UNIVERSITY OF OKLAHOMA

GRADUATE COLLEGE

Interaction Effects in Quantum Wires and One-Dimensional Incoherent Semimetals

A DISSERTATION

SUBMITTED TO THE GRADUATE FACULTY

in partial fulfillment of the requirements for the

Degree of

DOCTOR OF PHILOSOPHY

By

Geo Jose

Norman, Oklahoma

2022

Interaction Effects in Quantum Wires and One-Dimensional Incoherent Semimetals

A DISSERTATION APPROVED FOR THE

HOMER L. DODGE DEPARTMENT OF PHYSICS AND ASTRONOMY

BY THE COMMITTEE CONSISTING OF

Dr. Bruno Uchoa, Chair

Dr. Kieran Mullen

Dr. Michael Santos

Dr. Howard Baer

Dr. Tomasz Przebinda

Acknowledgments

I would like express my sincere gratitude to my Ph.D. supervisor Prof. Bruno Uchoa for his guidance. I am thankful to him for the several hours of discussions on various research topics. His broad expertise has helped me learn various topics during my Ph.D. and his passion to figure out things has always inspired me. I am grateful to him for his patience, constructive feedbacks, moral support, the opportunities he provided me, and for his care and concern at all times.

I would also especially like to thank Prof. Kieran Mullen for his amazing lectures and insightful discussions that have inspired me and generations of other graduate students. As a physicist and as a person, I have learned quite a lot from him and I will forever be indebted. My special thanks also to Prof. Howard Baer whose lectures on several advanced topics were inspirational to me. His lucid lectures and jokes are some of my fondest memories of graduate school. My sincere thanks also to Prof. Michael Santos and Prof. Tomasz Przebinda for serving on my advisory committee.

I would also like to thank all my friends, especially Ritwika Chakraborty, Sang Wook Kim, Alex Kerr, Hua Wang, Shadman Salam, Daniel Wilbern, Gaurav Nirala, Xin Guo, Vishnu Iyer, Namitha Ann James and Sharon. S. Philp for all the fun times inside and outside of academia. I thank my family for their constant love, care, and encouragement. I am grateful to them for always supporting my studies and efforts.

Abstract

In this thesis, we address the effect of interactions in low dimensional systems. In the first part, using bosonization, we study a microscopic model of parallel quantum wires constructed from two dimensional Dirac fermions in the presence of periodic topological domain walls. The model accounts for the lateral spread of the wave-functions ℓ in the transverse direction to the wires. The gapless modes confined to each domain wall are shown to form Luttinger liquids, which realize a well known smectic non-Fermi liquid fixed point when inter-wire Coulomb interactions are taken into account. Perturbative studies on phenomenological models have shown that the smectic fixed point is unstable towards a variety of phases such as superconductivity, stripe, smectic and Fermi liquid phases. Here, we show that the considered microscopic model leads to a phase diagram with only smectic metal and Fermi liquid phases. The smectic metal phase is stable in the ideal quantum wire limit $\ell \to 0$. For finite ℓ, we find a critical Coulomb coupling α_c separating the strong coupling smectic metal from a weak coupling Fermi liquid phase. We conjecture that the absence of superconductivity should be a generic feature of similar microscopic models. We also discuss the physical realization of this model with moiré heterostructures. In particular, our model may be of relevance to recent experiments on twisted bilayer tWTe$_2$.

In the second part we study a two band dispersive Sachdev-Ye-Kitaev model in 1+1 dimension. We suggest a model that describes a semimetal with quadratic dispersion at half-filling. We compute the Green's function at the saddle point using a combination of analytical and numerical methods. Employing a scaling symmetry of the Schwinger-Dyson equations that becomes transparent in the strongly dispersive limit, we show that the exact solution of the problem yields a distinct type of non-Fermi liquid with sub-linear $\rho \propto T^{2/5}$ temperature dependence of the resistivity. A scaling analysis indicates that this state corresponds to the fixed point of the dispersive SYK model for a quadratic band touching semimetal.

Contents

List of Figures

List of Publications

1. G. Jose and B. Uchoa, *Stability of smectic phases in parallel quantum wires*, arXiv: 2202.11744 (2022).

2. G. Jose, K. Seo and B. Uchoa, *Non-Fermi liquid behavior in the Sachdev-Ye-Kitaev model for a one dimensional incoherent semimetal*, Physical Review Research **4**, 013145 (2022).

3. A. Kerr, G. Jose, C. Riggert, and K. Mullen, *Automatic learning of topological phase boundaries*, Phys. Rev. E **103**, 023310 (2021).

4. S. W. Kim, G. Jose and B. Uchoa, *Hydrodynamic transport and violation of the viscosity-to-entropy ratio bound in nodal-line semimetals*, Phys. Rev. Research **3**, 033003 (2021).

5. G. Jose and B. Uchoa, *Quantum critical scaling of gapped phases in nodal-line semimetals*, Phys. Rev. B **101**, 115123 (2020).

6. G. Jose, R. Malla, V. Srinivasan, A. Sharma and S. Gangadharaiah, *Phase diagram for the Harper model of the honeycomb lattice*, J. Phys.:Condens. Matter **30**, 385603 (2018).

Chapter 1

Introduction

Several of the important advances in condensed matter physics in the last fifty years have been achieved in the context of low dimensional systems. The integer and fractional quantum Hall effects in two dimensional systems, subsequent prediction and discovery of topological materials, the advent of graphene based systems are prominent examples, to name a few. The simultaneous, rapid advancement in novel experimental techniques with the theoretical progress have made materials that host these systems very promising for technological and industrial applications. For example, topological materials are potentially useful for the design of more energy efficient microelectronic components and better storage devices. There have also been proposals of the possibility of topological quantum computers using anyons, which are particles with fractional statistics as qubits. Quantum wires can be used to make electron waveguides and high speed lasers. One dimensional electron systems are also naturally realized in carbon nanotubes which have found applications that range from transistors to biomedical devices.

Electron-electron interactions often play a fundamental role in these systems. The effect of interactions is often the key factor that decides the fate of these systems. For example, in the case of the quantum Hall effect, electrons in the presence of a magnetic field get arranged into Landau levels. Landau levels are dispersionless flat bands. Since the kinetic energy of electrons in flat Landau levels are quenched, interaction between electrons within Landau levels decides the many body state of the system. Providing a theoretical framework for strongly interacting systems can be challenging. In the case of the quantum Hall effect, Laughlin's ingenious ground state wave function led to the solution of the problem. In one dimensional systems, one can employ a procedure called

bosonization where the fermionic variables of the interacting electron problem can be traded for bosonic fields, after which the interacting fermionic problem becomes similar to a non-interacting boson problem, which can then be solved. Quite generally, if the interaction is perturbative, one can employ the framework of the renormalization group to assess the interacting system.

In this thesis, we explore the effects of electron-electron interactions in two low dimensional systems: a two dimensional array of parallel quantum wires and an incoherent semimetal in one dimension. One dimensional electron systems are special. In two or more spatial dimensions Fermi liquid theory provides a good description of the generic metallic state [1–5]. In these systems there is a one to one correspondence between the low energy modes in the non-interacting and interacting theory: the latter are dressed versions of the former with modified masses and other properties. In one dimension however, the low energy modes of the interacting theory are drastically different from the non-interacting theory. These are density waves which are described by Luttinger liquid theory [1, 15, 16]. These systems have power law correlations and several transport properties that have unusual power law dependence on temperature, where the powers depend on the interaction parameters. There have been many attempts to generalize such non-Fermi liquids to higher dimensions for various reasons [27–29, 38–40].

Quite recently experiments on moiré heterostructures in twisted bilayer systems have suggested that the effective description of such systems could be that of periodic structures formed out of effective one dimensional electron channels [41, 55]. Phenomenological calculations have shown that in coupled wire constructions, a generic phase diagram can be drawn that consists of a variety of non-Fermi liquid phases such as charge density waves, superconductivity and a smectic metal phase [38–40]. We undertake a microscopic calculation taking in to account realistic interactions in the model to see what part of the generic phase diagram survives [57]. We show that superconductivity is generically expected to be absent in such systems. In the absence of backscattering we predict a phase diagram that consists of a Fermi liquid phase and a smectic metal phase separated by a quantum phase transition and then consider the role of backscattering effects. We expect our results to be relevant to experiments done on twisted bilayer systems that form moiré patterns comprising of periodic lattice of one dimensional channels, in particular to the recent experiment on twisted bilayer tWTe$_2$ [41].

In the second part of the thesis, we study the properties of an incoherent semimetal. Incoherent

systems refer to those systems that lack a description in terms of quasiparticles. These systems resemble those near quantum critical points with power law correlation functions. Recently, there has been a huge interest in the study of a class of models called Sachdev-Ye-Kitaev models[85, 86]. These models describe quantum dots that lack a quasiparticle description. They are exactly solvable in the limit of large number of flavors of fermions in each dot. Higher dimensional versions [104–106, 111–113] of these comprising of a lattice of quantum dots which would form a Fermi liquid in the absence of interactions, have been shown to lead to a linear in temperature resistivity when each lattice point consists of an SYK dot. The generic situation in these systems is that as a function of temperature, the model allows for two phases: high temperature phase consisting of an incoherent metal with linear in temperature resitivity and a low temperature Fermi liquid phase [106, 111]. Linear in temperature resistivity is also known to be characteristic of the strange metal phase of high temperature superconductors [94, 95, 108–110]. It has also been shown that the correlators in the SYK model match precisely with those of the two-dimensional anti–de Sitter (AdS_2) horizons of extremal charged black holes [85]. We introduce and study a certain lattice model which involves a one dimensional quadratically dispersing semimetal in the presence of local SYK interactions [119]. This model lacks a Fermi surface to begin with. We show that as a function of temperature, the model allows for two phases: a high temperature incoherent semi-metallic phase with a linear in temperature resistivity and a low temperature phase which is a distinct type of incoherent semimetal with a sub-linear power law dependence of resistivity on temperature.

1.1   Outline

This thesis is organized into three main chapters. Chapter two is devoted to the study of interactions in coupled quantum wire systems. As an introduction to the system we begin by reviewing the theory of one dimensional electron systems. We introduce the low energy description of electron gases in one dimension and introduce the description in terms of collective density modes. This is followed by an introduction to the procedure of bosonization which makes the problem exactly solvable. Equipped with this background, we move on to a literature review of coupled one dimensional systems. We review the various possible phases that can arise in these systems based on phenomenological studies. The next section reviews the recent experimental advances in twisted moiré heterostructures. We

describe two recent experiments that have given evidence that these systems are amenable to a description in terms of a lattice of effective one dimensional electron channels. These arise from the underlying moiré patterns. With this background we introduce an effective microscopic model that realizes a system of coupled quantum wires. The model comprises of a single sheet of graphene in the presence of a periodic mass term. It is well known in this context that zero energy modes live on the interfaces where the mass term changes sign. In the present model, the mass term is zero along the interfaces across which it changes sign. These interfaces form an array of parallel wires. We analytically compute the wave-functions of the modes that live on these interfaces and show that they correspond to left and right moving modes on each wire. We then incorporate microscopic Coulomb interactions into this model and use bosonization to compute the effective Luttinger parameters. Incorporating inter-wire Coulomb interactions we arrive at the smectic metal action, which is a distinct non-Fermi liquid state of matter. We then consider various perturbations to this action and compute the phase diagram and compare it with previous phenomenological studies. This part is based on [57].

Chapter three is an introduction to the literature on SYK models. We begin by a review of the original SYK quantum dot model and introduce the replica trick used to analyze the model. We review the derivation of the Schwinger-Dyson equations and elucidate the emergent conformal/reparametrization symmetry of these equations. The next section reviews an experimental proposal to realize this model using an irregular graphene flake. We then give an overview of the various lattice extensions of the SYK model in literature and the generic phase diagram of these models as function of temperature. This sets the stage for the semi-metallic model studied in chapter four. In that chapter we introduce a semi-metallic version of the SYK model. We then derive the Schwinger-Dyson equations in this model and show that they possess a certain scaling symmetry while conformal symmetry is absent. We use the scaling symmetry to deduce the temperature dependence of the Green's function and the self-energy. We then numerically compute the scaling function and write down the Green's function and self-energies. We show that the Green's function has two distinct forms in two different temperature regimes. We then compute the dc conductivity in the two regimes and show that the two different temperature regimes allow for two distinct type of incoherent semi-metallic states. This part has been published in Physical Review Research [119].

Chapter five describes the conclusions. This chapter summarizes the various results of this thesis

and provides an outlook on possible future directions.

Chapter 2

Interaction effects in quantum wires

One dimensional electron systems occur in many experimental situations. Common experimental systems where they occur are quantum wires [7, 8], carbon nanotubes[9–11], edge states of quantum Hall systems [12–14]. They also occur in organic compounds, Bechgaard salts, some dichalcogenide materials and complex oxides[16]. Some oxides can also be described as a set of weakly coupled ladders[15]. The low energy physics of these systems is described in the terms of density waves under the frame work of Luttinger liquid theory. The correlation functions of these systems reveal that these systems generally live at a quantum critical point[15, 16]. Since such systems do not fall under the paradigm of conventional Fermi liquids, they are an example of non-Fermi liquid behavior. Arrays of parallel LL's have been studied extensively in the past thirty years with motivations such as the possibility of constructing non Fermi liquids in dimension greater than one and understanding the unusual normal state in cuprate superconductors [25, 29–35]. Perturbations to the decoupled parallel LL arrays were generically shown to result in a higher dimensional Fermi liquid or an ordered state [36, 37]. It was then pointed out that one needs to include other marginal operators such as inter-wire density-density and current-current interactions in the most general fixed point action, which then describes a generalized smectic state [38]. The perturbative stability of the smectic fixed is now understood and leads to a rich, if generic, phase diagram, where the following phases can arise: *i)* smectic superconductor, *ii)* insulating stripe crystal, *iii)* Fermi liquid and *iv)* smectic metal state [38–40]. However these calculations were done from a phenomenological point of view.

Quite recently there have been several important advances in twisted moiré systems in which one dimensional physics seem to play an important role. It was shown that twisted bilayer of

graphene on HBN could be described as an effective triangular array of one dimensional channels in the presence of a gate voltage[63, 79]. Recent experiments have suggested that marginally twisted bilayer graphene undergoes a lattice reconstruction to form a triangular array of one dimensional channels[55]. Phenomenological theories applied to such a model have revealed a rich phase diagram with several strongly correlated phases[56]. Even more recently, experiments on twisted bilayer tWTe$_2$ have revealed that this system realizes parallel arrays of one dimensional wires where the distance between the wires is tunable by the twist angle[41]. In the light of these events we study an effective microscopic model that realizes a two dimensional array parallel one dimensional channels and compute the phase diagram taking into account microscopic Coulomb interactions in the system. We find that superconductivity is generically absent in this model and there is a quantum phase transition that separates a smectic metal phase from a two dimensional Fermi liquid phase. This chapter begins with an introduction to one dimensional systems and the method of Bosonization[15, 16, 18, 19]. This is followed by a literature review of the phenomenological calculations and the generic phase diagram expected in these systems. We also review the recent experimental advances as a motivation to the effective microscopic model. This is followed by a discussion of an effective microscopic model of parallel quantum wires constructed out of monolayer graphene in the presence of a periodic mass term. This part is based on [57].

2.1 Quantum wires.

The continuum Hamiltonian of a spin-less one dimensional electron gas is given by the Hamiltonian

$$\mathcal{H}_0 = \int dx \, \psi^\dagger(x) \left(-\frac{\hbar^2}{2m} \frac{\partial^2}{\partial x^2} - \mu \right) \psi(x). \tag{2.1}$$

The spectrum of this Hamiltonian is shown in Fig 2.1, where $\mu = E_F$.

To construct a low energy theory we focus on the low energy excitations. We have two Fermi points at $\pm K_F$. The single particle energies of the states close to the Fermi points are

$$\varepsilon(k) \simeq \frac{K_F^2}{2m} + v_F \left(|k| - K_F \right) + .. \tag{2.2}$$

If we restrict ourselves to a momentum cutoff Λ from the Fermi points, the Fourier expansion of
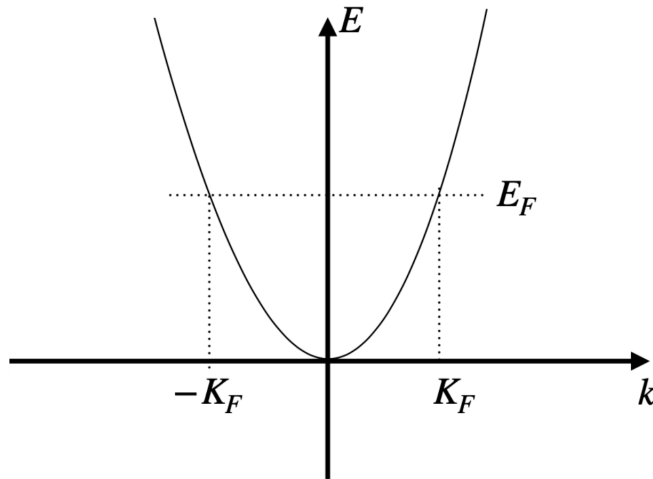
Figure 2.1: The dispersion of the model (2.1).

the field operator may be written as

$$\psi(x) \simeq \int_{-\Lambda}^{\Lambda} \frac{dk}{2\pi} e^{i(k+K_F)x}\psi\left(k+K_F\right) + \int_{-\Lambda}^{\Lambda} \frac{dk}{2\pi} e^{i(k-K_F)x}\psi\left(k-K_F\right). \tag{2.3}$$

Defining the left and right moving modes $\psi_{+,-}(x)$, we have $\psi(x) \simeq e^{iK_F x}\psi_+(x) + e^{-iK_F x}\psi_-(x)$. The Fourier transforms of left and right moving modes are given by

$$\psi_{+/-}(k) = \psi\left(k \pm K_F\right). \tag{2.4}$$

The Hamiltonian (2.1) then becomes,

$$\mathcal{H}_0 = \sum_{\alpha=+,-} \int_{-\Lambda}^{\Lambda} \frac{dk}{2\pi} \epsilon_\alpha v_F k \psi_\alpha^\dagger(k)\psi_\alpha(k) \tag{2.5}$$

where $\epsilon_\pm = \pm 1$. We can also rewrite a generic interaction of the form

$$\mathcal{H}_{int} = \int dx V(x - x')\rho(x)\rho(x') \tag{2.6}$$

where $\rho(x) = \psi^\dagger(x)\psi(x)$ denotes the particle density at position x,in terms of left and right movers.
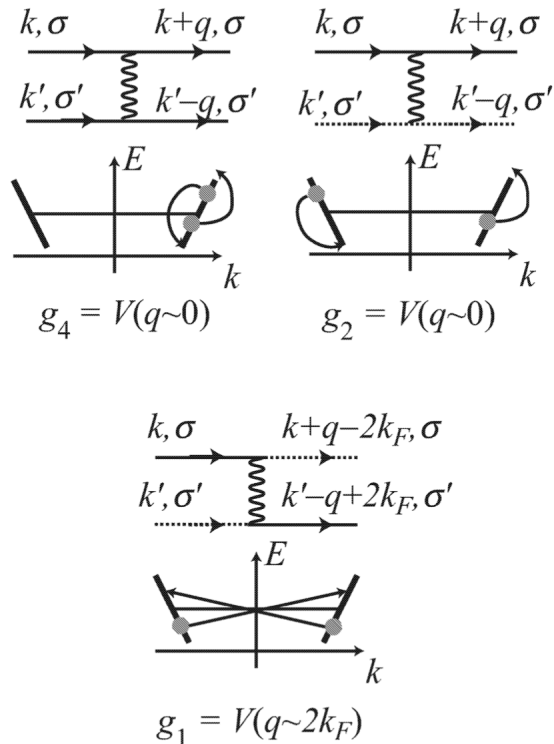
Figure 2.2: Various interaction processes in Luttinger liquids. The nomenclature g_i is conventional. When spin is included each process gets two contributions, one where the spin indices are conserved and one where the spin indices get interchanged.[15]

The density operator then becomes

$$\rho(x) = \rho_+(x) + \rho_-(x) + e^{2ik_F x}\psi_-^\dagger(x)\psi_+(x) + e^{-2ik_F x}\psi_+^\dagger(x)\psi_-(x), \tag{2.7}$$

where $\rho_\pm(x) = \psi_\pm^\dagger(x)\psi_\pm(x)$ are the right/left moving densities. The first two terms above correspond to the $q \sim 0$ part of the density and the last two terms correspond to the $q \sim 2K_F$ part. Using the expression for the density, one can classify the interaction processes based on whether they involve fermions from the same side of the Fermi surface or different sides as shown in the Fig. 2.2.

This classification gives the interactions to be of the types g_1, g_2 and g_4 where $g_{2,4} \simeq V(q \sim 0)$ correspond to foward scattering terms and $g_1 \simeq V(q \sim 2K_F)$ to a backscattering term. In the absence of backscattering, $g_1 = 0$ and we only have a model with g_2 and g_4. For the spin-less case, the distinction $\left(g_i^\parallel, g_i^\perp\right)$ is superficial and we just have g_i. The spinful case is treated below. Thus

we can write

$$\mathcal{H}_{int} = \int dx g_4 \rho_+(x)\rho_+(x) + \int dx g_4 \rho_-(x)\rho_-(x) + 2\int dx g_2 \rho_+(x)\rho_-(x). \qquad (2.8)$$

To solve this model, we use the method of bosonization. Bosonization involves rewriting the fermionic variables in terms of Bosonic fields and appropriate 'Klein factors' to maintain the commutation relations. Lets say we remove an electron from the filled part of the right moving branch at momentum k and place it at momentum $k + q$. This is a particle-hole excitation. Its energy is

$$v_F\left(k + q - K_F\right) - v_F\left(k - K_F\right) = v_F q \qquad (2.9)$$

and momentum

$$k + q - k = q \qquad (2.10)$$

So, particle-hole excitations have well defined momenta and energy. They can be used to construct a basis. The Fourier transform of the density operator, $\rho(x)$

$$\rho(q) = \sum_k \psi^\dagger(k+q)\psi(k) \qquad (2.11)$$

is a superposition of particle-hole excitations. Moreover, these are products of fermionic operators and are therefore bosonic in nature. In order to avoid infinities when the cutoff is taken to infinity, is it useful to work with operators that are normal ordered with respect to the ground state. The normal ordered densities of left and right movers are defined as

$$: \rho_{q,r}^\dagger : \quad = \quad \sum_k c_{k+q,r}^\dagger c_{k,r}, \quad q \neq 0 \qquad (2.12)$$

$$= \quad \sum_k c_{k,r}^\dagger c_{k,r} - \langle 0 | c_{k,r}^\dagger c_{k,r} | 0 \rangle, \quad q = 0 \qquad (2.13)$$

These *normal ordered* density operators satisfy the commutation relations:

$$[\rho_r^\dagger(p), \rho_{r'}(p')] = -\delta_{r,r'}\delta_{p,p'}\frac{rpL}{2\pi} \qquad (2.14)$$

$$[\rho_r^\dagger(p), \psi_r(x)] = -e^{ipx}\psi_r(x) \qquad (2.15)$$

where L is the length of the wire, and periodic boundary conditions have been used. In order to define a new bosonic basis, we need to express the original Fermionic operators in terms of new bosonic variables. It can be verified that if we take

$$\psi_r(x) = U_r e^{\sum_p e^{ipx} \rho_r^\dagger(-p) \frac{2\pi r}{pL}}, \tag{2.16}$$

the commutation relations can be satisfied. U_r is called a Klein factor. It commutes with the bosonic operators and $U_r^\dagger$ adds a fermion species of type r. A rigorous derivation of this mapping is presented in several sources, for example in Appendix B.1 of Ref. [15]. It is more convenient to work with two different bosonic operators $\phi_\pm$, under which the bosonization maps are

$$\psi_\pm(x) = \frac{U_\pm}{\sqrt{2\pi\alpha}} e^{\pm i k_F x} e^{\pm i 2\sqrt{\pi}\phi_\pm(x)}. \tag{2.17}$$

where α is a convergence factor which should be set to zero at the end of calculations. Using this map, the non interacting Hamiltonian becomes

$$\mathcal{H}_0 = v_F \int dx \left[(\partial_x \phi_+)^2 + (\partial_x \phi_-)^2 \right]. \tag{2.18}$$

The usefulness of this formalism becomes evident when we rewrite the interaction part in terms of the bosonic variables: they become quadratic in the bosonic fields. The normal ordered densities ar

$$: \rho_+(x) :=: \psi_+^\dagger(x)\psi_+(x) :=: \frac{1}{\sqrt{\pi}} \frac{\partial \phi_+(x)}{\partial x} : . \tag{2.19}$$

Similarly one can get

$$: \rho_-(x) :=: \psi_-^\dagger(x)\psi_-(x) :=: \frac{1}{\sqrt{\pi}} \frac{\partial \phi_-(x)}{\partial x} : \tag{2.20}$$

Using these, the interaction Hamiltonian (2.8) above becomes,

$$\mathcal{H}_{int} = \int dx g_4 \frac{1}{\pi} \left(\frac{\partial \phi_+(x)}{\partial x} \right)^2 + \int dx g_4 \frac{1}{\pi} \left(\frac{\partial \phi_-(x)}{\partial x} \right)^2 + 2 \int dx g_2 \frac{1}{\pi} \frac{\partial \phi_+(x)}{\partial x} \frac{\partial \phi_-(x)}{\partial x}. \tag{2.21}$$

Using a change of variables, $\phi_r(x) = \frac{1}{2}[\phi(x) + r\theta(x)]$, we get $\mathcal{H} = \mathcal{H}_0 + \mathcal{H}_{int}$

$$\mathcal{H} = \frac{u}{2} \int dx \left\{ \frac{1}{K}(\partial_x \theta)^2 + K(\partial_x \phi)^2 \right\} \qquad (2.22)$$

$$
\begin{aligned}
\frac{u}{K} &= v_F \left[1 + \left(\frac{g_4 - g_2}{\pi v_F} \right) \right] \\
uK &= v_F \left[1 + \left(\frac{g_4 + g_2}{\pi v_F} \right) \right]
\end{aligned}
\qquad (2.23)
$$

Thus, upon Bosonization, the interacting fermionic theory becomes a non interacting bosonic theory. u, K are called Luttinger parameters. This Hamiltonian defines the Luttinger liquid. Integrating out either the θ or ϕ field we can arrive at an effective action for one type of field. This is done in Appendix A and gives,

$$\mathcal{S} = \frac{K}{2} \int_\tau \int_y \left[\frac{1}{u}(\partial_\tau \phi(\tau, y))^2 + u(\partial_y \phi)^2 \right] \qquad (2.24)$$

upon integrating out the θ field.

If back scattering is present, we need to add the interaction term g_1 to the Hamiltonian. This is given by the Hamiltonian,

$$
\begin{aligned}
\mathcal{H}_{back} &= g_1 \int dx \psi_+^\dagger(x)\psi_-^\dagger(x)\psi_+(x)\psi_-(x) \qquad (2.25) \\
&= -g_1 \int dx \rho_+(x)\rho_-(x).
\end{aligned}
$$

Since this takes the same form as the interaction g_2, we can simply account for backscattering by making the substitution $g_2 \to g_2 - \frac{g_1}{2}$ in the Luttinger parameters (2.23)[15]. The analysis of the spinful case proceeds along the same lines. Now each process takes two values $\left(g_i^\parallel, g_i^\perp\right)$ depending on whether the spins σ and σ' on each fermion is equal $\left(g_i^\parallel\right)$ or opposite $\left(g_i^\perp\right)$. In this case we will need to introduce the boson representation separately for each spin $(\phi_\uparrow, \theta_\uparrow)$ and $(\phi_\uparrow, \theta_\uparrow)$.

The kinetic part of the Hamiltonian simply becomes a sum $\mathcal{H}_0 = \mathcal{H}_0^\uparrow + \mathcal{H}_0^\downarrow$. Now we need to take into account all the processes in Fig. 1.2. g_4 processes now contribute the following term to

the interaction Hamiltonian:

$$\mathcal{H}_{g_4} = \sum_{r=\pm,\sigma} g_4^{\parallel} \int dx \rho_{r,\sigma}(x) \rho_{r,\sigma}(x) + g_4^{\perp} \int dx \rho_{r,\sigma}(x) \rho_{r,-\sigma}(x) \tag{2.26}$$

Similarly, the g_2 processes contribute

$$\mathcal{H}_{g_2} = \sum_{r=\pm,\sigma} g_2^{\parallel} \int dx \rho_{r,\sigma}(x) \rho_{-r,\sigma}(x) + g_2^{\perp} \int dx \rho_{r,\sigma}(x) \rho_{-r,-\sigma}(x) \tag{2.27}$$

In the following, we shall take $\left(g_{2,4}^{\parallel} = g_{2,4}^{\perp} \right)$ since that is the case in the problem we shall be interested in. As in the spin-less case, we need to make some field transformations to arrive at the quadratic boson Hamiltonian. We define

$$\phi_r^{\sigma}(x) = \frac{1}{2} \left[\phi^{\sigma}(x) + r\theta^{\sigma}(x) \right]. \tag{2.28}$$

Further defining density and spin variables:

$$\Theta^{\rho} = \frac{\theta^{\uparrow}(x) + \theta^{\downarrow}(x)}{\sqrt{2}}, \qquad \Theta^{\sigma} = \frac{\theta^{\uparrow}(x) - \theta^{\downarrow}(x)}{\sqrt{2}}, \tag{2.29}$$

and similarly

$$\Phi^{\rho} = \frac{\phi^{\uparrow}(x) + \phi^{\downarrow}(x)}{\sqrt{2}}, \qquad \Phi^{\sigma} = \frac{\phi^{\uparrow}(x) - \phi^{\downarrow}(x)}{\sqrt{2}}, \tag{2.30}$$

we get,

$$\mathcal{H}_0 = \frac{v_F}{2} \int dy \left[(\partial_y \Theta^{\rho})^2 + (\partial_y \Phi^{\rho})^2 \right] + \frac{v_F}{2} \int dy \left[(\partial_y \Theta^{\sigma})^2 + (\partial_y \Phi^{\sigma})^2 \right]. \tag{2.31}$$

for the free part and

$$\mathcal{H}_{int} = \frac{1}{2} \left\{ \int dx \frac{2g_4}{\pi} \left[\left(\frac{\partial \Theta^{\rho}}{\partial x} \right)^2 + \left(\frac{\partial \Phi^{\rho}}{\partial x} \right)^2 \right] + \int dx \frac{2g_2}{\pi} \left[\left(\frac{\partial \Phi^{\rho}}{\partial x} \right)^2 - \left(\frac{\partial \Theta^{\rho}}{\partial x} \right)^2 \right] \right\} \tag{2.32}$$

13

for the interacting one. Thus the full Hamiltonian, $\mathcal{H} = \mathcal{H}_0 + \mathcal{H}_{int}$ is thus given by

$$
\begin{aligned}
\mathcal{H} &= \mathcal{H}^\rho + \mathcal{H}^\sigma \\
\mathcal{H}^\rho &= \frac{1}{2} \int dy \left\{ (\partial_y \Theta^\rho)^2 \frac{u^\rho}{K^\rho} + (\partial_y \Phi^\rho)^2 u^\rho K^\rho \right\} \\
H^\sigma &= \frac{1}{2} \int dy \left\{ (\partial_y \Theta^\sigma)^2 \frac{u^\sigma}{K^\sigma} + (\partial_y \Phi^\sigma)^2 u^\sigma K^\sigma \right\},
\end{aligned}
$$

with the Luttinger parameters in the charge and spin sectors

$$
\frac{u^\rho}{K^\rho} = v_F \left[1 + \frac{2g_4}{\pi v_F} - \frac{2g_2}{\pi v_F} \right] \tag{2.33}
$$

$$
u^\rho K^\rho = v_F \left[1 + \frac{2g_4}{\pi v_F} + \frac{2g_2}{\pi v_F} \right], \tag{2.34}
$$

and

$$
u^\sigma = v_F, \qquad K^\sigma = 1. \tag{2.35}
$$

In this process, we have reformulated an interacting fermionic theory given by (2.5),(2.8) into a non-interacting bosonic theory. The interactions parameters are now parametrized by the Luttinger parameters. The free bosonic theory makes it easier to calculate various quantities of interest. The separation of the Hamiltonian into separate charge and spin sectors is referred to as spin-charge separation. Including g_1 interactions, we have an extra term

$$
\begin{aligned}
\mathcal{H}_{g_1} &= -g_1^{\parallel} \int dx \psi_{-,\sigma}^\dagger(x)\psi_{-,\sigma}(x)\psi_{+,\sigma}^\dagger(x)\psi_{+,\sigma}(x) + g_1^{\perp} \int dx \psi_{-,\sigma}^\dagger(x)\psi_{+,\sigma}(x)\psi_{+,-\sigma}^\dagger(x)\psi_{-,-\sigma}(x) \\
&= -g_1^{\parallel} \int dx \rho_{-,\sigma}(x)\rho_{+,\sigma}(x) + g_1^{\perp} \int dx \psi_{-,\sigma}^\dagger(x)\psi_{+,\sigma}(x)\psi_{+,-\sigma}^\dagger(x)\psi_{-,-\sigma}(x) \tag{2.36}
\end{aligned}
$$

Upon bosonization, these become,

$$
\begin{aligned}
\mathcal{H}_{g_1} &= -g_1^{\parallel} \int dx \rho_{-,\sigma}(x)\rho_{+,\sigma}(x) + \frac{g_1^{\perp}}{(2\pi\alpha)^2} \cos\left(2\sqrt{2\pi}\Phi^\sigma\right) \\
&= \frac{-g_1^{\parallel}}{4\pi} \int dx \left\{ (\partial_y \Phi^\rho)^2 + (\partial_y \Phi^\sigma)^2 - (\partial_y \Theta^\rho) - (\partial_y \Theta^\sigma)^2 \right\} + \frac{g_1^{\perp}}{(2\pi\alpha)^2} \cos\left(2\sqrt{2\pi}\Phi^\sigma\right)
\end{aligned}
$$

This implies that the Luttinger parameters get modified in the following manner

$$\frac{u^\rho}{K^\rho} = v_F \left[1 + \frac{2g_4}{\pi v_F} - \frac{2g_2}{\pi v_F} + \frac{g_1^{\parallel}}{2\pi v_F} \right] \tag{2.37}$$

$$u^\rho K^\rho = v_F \left[1 + \frac{2g_4}{\pi v_F} + \frac{2g_2}{\pi v_F} - \frac{g_1^{\parallel}}{2\pi v_F} \right] \tag{2.38}$$

and

$$\frac{u^\sigma}{K^\sigma} = v_F \left[1 + \frac{g_1^{\parallel}}{2\pi v_F} \right] \tag{2.39}$$

$$u^\sigma K^\sigma = v_F \left[1 - \frac{g_1^{\parallel}}{2\pi v_F} \right]. \tag{2.40}$$

Similarly, one could also have an umklapp term exactly at half filling[15]. This term takes the form $\mathcal{H}_u = \frac{g_u}{(2\pi\alpha)^2} \cos\left(2\sqrt{2\pi}\Phi^\rho\right)$. Thus we see that in the absence of backscattering and umklapp terms, the interacting fermionic Hamiltonian gets mapped to a spin-charge separated bosonic model, known as the Tomonaga-Luttinger model. $u^{\rho,\sigma}$ correspond to effective velocities, while $K^{\rho,\sigma}$ are called stiffness parameters. These parametrize the effect of interactions. The stiffness parameter decides the power law decay of most correlation functions.

2.2 Arrays of parallel quantum wires.

As discussed in the previous section, one dimensional electron systems can be described as Luttinger liquids. Arrays of weakly coupled Luttinger liquids have been well studied by several authors [20–24, 26–28, 96, 97]. It was however shown that such systems always order at low temperatures or cross over to a higher dimensional Fermi liquid state. However the investigations following Anderson's suggestion[25] that electron transverse hopping may be incoherent, allowing for a non-Fermi liquid in dimensions greater than one showed that the inclusion of strong forward scattering interactions between the chains lead to a stable non Fermi liquid phase in two dimensions called the sliding Luttinger liquid or the smectic metal phase [38–40]. Considering a parallel array of wires, each labeled by an integer a and taking into account inter-stripe density-density and current-current

interactions, leads to an imaginary time Lagrangian density of the form [38]

$$\mathcal{L}_{smectic} = \frac{1}{2} \sum_{a,a',\mu} j_\mu^a \widetilde{W_\mu}(a - a') j_\mu^{a'}, \tag{2.41}$$

where $j_{0,1} = \rho_+ \pm \rho_-$ are the density and current operators. The phenomenological parameters $\widetilde{W_\mu}$ should come from the microscopic interactions present in a given model as we shall see later. Incorporating this into the Luttinger liquid action, the fixed point action has the generic form

$$\mathcal{S} = \frac{1}{2} \sum_{\mathbf{k}} \left\{ W_0(\mathbf{k})\omega^2 + W_1(\mathbf{k})k^2 \right\} \phi(\mathbf{k})^2 \tag{2.42}$$

where $\mathbf{k} = (\omega, k, k_\perp)$. Equivalently, integrating out $\phi(\mathbf{k})$ instead of $\theta(\mathbf{k})$, we get

$$\mathcal{S} = \frac{1}{2} \sum_{\mathbf{k}} \left\{ \frac{\omega^2}{W_0(\mathbf{k})} + \frac{k^2}{W_1(\mathbf{k})} \right\} \theta(\mathbf{k})^2 \tag{2.43}$$

The action (2.42) preserves the smectic symmetry $\phi_a(x) \to \phi_a(x) + \alpha_a$ (where α_a is constant on each stripe) of the decoupled Luttinger liquids. For this action, the charge-density-wave order parameters of the individual wires do not lock with each other, and the charge density profiles on each wire can slide relative to each other without an energy cost. In other words, there is no rigidity to shear deformations of the charge configuration on nearby stripes. This is the smectic metal phase. Various instabilities can occur at this fixed point action.

In a classical setting, smectic phases are examples of liquid crystal phases in liquids formed by rod shaped molecules[17]. In the liquid phase, the axes of these molecules are randomly oriented and their centers of mass are randomly distributed. When these liquids are cooled, they undergo phases transitions to states of lower symmetry. Liquid crystals in classical systems are phases that are intermediate between a liquid and a solid, and spontaneously break the rotation and/or translation symmetries of free space. Upon cooling an isotropic liquid, the first liquid crystal phase that can occur is the nematic phase, in which the axes of these molecules are oriented in a given direction. However their centers of masses are still randomly distributed. Thus the nematic phase breaks rotational isotropy, but not translational invariance of free space. On further reduction of temperature, molecules segregate into planes leading to the smectic phase. There is liquid-

like motion in each layer, but no correlation between molecules in different layers. Electronic liquid crystal phases are similarly quantum mechanical systems with intermediate symmetries. The smectic phase breaks translational symmetry in only one direction. Along the other direction, it has the character of an electron liquid.

The most important perturbations to the smectic phase are singlet pair tunneling (Josephson), coupling between CDW order parameters and single particle hopping. These are given by

$$\mathcal{H}_{sc} = \sum_{a,a'} g_{sc}^{ij} \psi_{Ra}^{\dagger} \psi_{La}^{\dagger} \psi_{Ra'} \psi_{La'} + c.c. \tag{2.44}$$

$$\mathcal{H}_{cdw} = \sum_{a,a'} g_{cdw}^{ij} \psi_{Ra}^{\dagger} \psi_{La} \psi_{La'}^{\dagger} \psi_{Ra'} + c.c. \tag{2.45}$$

$$\mathcal{H}_{sp} = \sum_{a,a'} g_{sp}^{ij} \psi_{Ra}^{\dagger} \psi_{Ra'} + \psi_{La}^{\dagger} \psi_{La'} + c.c. \tag{2.46}$$

where *c.c.* stands for complex conjugate.

Upon restricting to nearest neighbor coupling and Bosonizing using (2.17), these become,

$$\mathcal{H}_{sc} = g_{sc} \sum_{a} \cos \left[\sqrt{4\pi} \left(\theta_a - \theta_{a+1} \right) \right] \tag{2.47}$$

$$\mathcal{H}_{cdw} = g_{sc} \sum_{a} \cos \left[\sqrt{4\pi} \left(\phi_a - \phi_{a+1} \right) \right] \tag{2.48}$$

$$\mathcal{H}_{sp} = g_{sp} \sum_{a} \cos \left[\sqrt{\pi} \left(\theta_a - \theta_{a+1} \right) \right] \cos \left[\sqrt{\pi} \left(\phi_a - \phi_{a+1} \right) \right] \tag{2.49}$$

These perturbations cause the smectic metal fixed point (2.42) to be unstable. Their relevance can be ascertained using a perturbative renormalization group calculation. This calculation is sketched in Appendix B. These perturbations become relevant when their RG scaling dimensions $\eta > 0$. The scaling dimensions for perturbation $X = sc, cdw, sp$ are given by $\eta_X = 2 - \Delta_X$, where

$$\triangle_{sc} = 2 \int_{-\pi}^{\pi} \frac{dk_{\perp}}{2\pi} \left[\kappa \left(k_{\perp} \right) \right] \left(1 - \cos k_{\perp} \right)$$

$$\triangle_{cdw} = 2 \int_{-\pi}^{\pi} \frac{dk_{\perp}}{2\pi} \left[\kappa \left(k_{\perp} \right) \right]^{-1} \left(1 - \cos k_{\perp} \right)$$

$$\triangle_{sp} = \frac{\triangle_{sc}}{4} + \frac{\triangle_{cdw}}{4}$$

with $\kappa = \sqrt{W_0(k_{\perp})W_1(k_{\perp})}$. In order to compute the scaling dimensions, the phenomenological

parameter κ is expanded in a Fourier cosine series and the first two terms are retained. This gives $\kappa = \kappa_0 + \kappa_1 \cos k_\perp + ...$ The case of a spinful model can be treated in a similar manner. Including spin, the scaling dimensions of the perturbations get trivial modifications [38, 40] as discussed in Appendix B, namely $\triangle_{sc}^{\text{spin}} = 1 + \frac{1}{2}\triangle_{sc}$, $\Delta_{cdw}^{\text{spin}} = 1 + \frac{1}{2}\triangle_{cdw}$, and $\triangle_{sp}^{\text{spin}} = \frac{1}{2} + \frac{1}{2}\triangle_{sp}$. A phase diagram that shows various regions where the above perturbations are stable can now be drawn as a function of $\kappa_{0,1}$. This is shown in Figs. 2.3 and 2.4. The perturbation (2.44) that leads to superconductivity can be understood as the hopping of a pair of electrons from one chain to another. Using a mean field decomposition, of the perturbation, one can interpret θ as the superconducting phase field[15]. (2.44) however still preserves the smectic symmetry making this phase a smectic superconductor. (2.45) involves backscattering operators on neighboring wires. Backscattering on individual wires can lead to charge density wave instabilities and therefore wave order parameters on neighboring wires. Therefore, (2.45) can be interpreted as a coupling between charge density wave order parameters on neighboring wires. When this operator is relevant the system is considered to be a stripe crystal. When single particle hopping between wires is the most dominant perturbation, the coupled wire picture is lost, and the system undergoes a dimensional crossover to a conventional Fermi liquid phase in two dimensions, which can itself exhibit a BCS instability. When all these perturbations are irrelevant, the smectic metal action is stable and the system is said to be in a smectic metal phase.
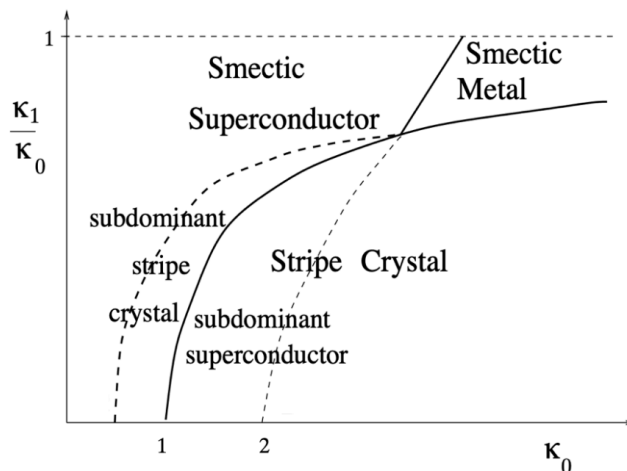
Figure 2.3: Phase diagram of an array of parallel coupled Luttinger liquids taken from [38]. Here a spin gapped case is considered, where spin degrees of freedom are effectively frozen which is expected to be the case in one-dimensional correlated electron fluids in the stripe phases of high-temperature superconductors coupled to an active environment.
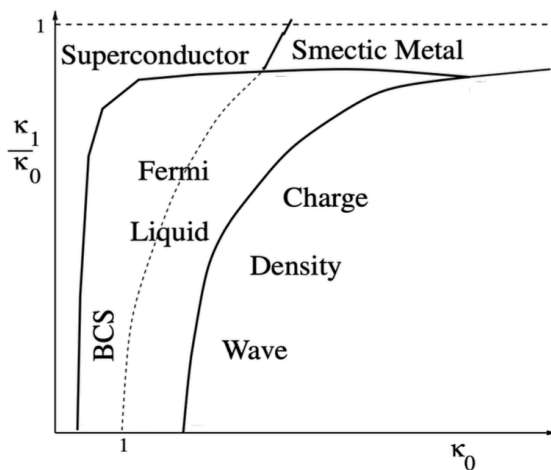
Figure 2.4: Phase diagram of an array of parallel coupled Luttinger liquids for the spinful case taken from [38].

2.3   Quantum wires in twisted moiré heterostructures.

Moiré patterns appear when two or more periodic lattices are overlaid slightly askew, leading to a new larger periodic pattern. Moire patterns have a spatial structure on a larger scale than either of the two lattices. Experimentally, the Moire patterns can be realized by stacking 2D materials together. For example, Fig. 2.5 shows a moire pattern resulting from two graphene sheets twisted
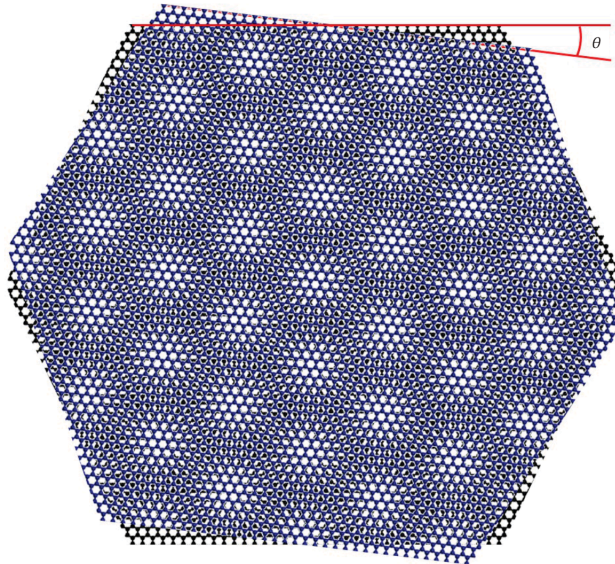
Figure 2.5: Moire pattern from two graphene layers twisted relative to one another by an angle θ [46].

relative to one another.

Such moiré heterostructures offer a formidable platform for building arrays of identical and perfectly spaced quantum wires. In general, application of a voltage difference between two layers in a van der Waals heterostructure (achievable by separately controlling the gates at each layer) permits theoretically integrating out the degrees of freedom in one of the layers. This results in an effective description for the other layer, that is affected by local potentials that modulate with the period of the moiré pattern [64]. In the case of moiré heterostructures with Dirac fermions in each monolayer, as in marginally twisted graphene bilayers, those local potentials create periodic scalar, vector and mass terms [79, 81–83]. A periodic mass term can confine Dirac fermions, with the lines where it changes sign forming quasi-1D modes that are topological. The periodic vector potential can be gauged away [63], and the scalar potential controlled with gating effects. Below, we briefly describe how 1D channels could emerge microscopically in systems where individual layers are honeycomb lattices [63, 79].

The Hamiltonian of a two layer system can be written as a sum of the Hamiltonians of individual layers and an interlayer coupling term,

$$\mathcal{H} = \sum_{l=1,2} \mathcal{H}^{(l)} + \mathcal{H}^{(12)} \tag{2.50}$$

where $l = 1, 2$ labels the two layers. The long wavelength Dirac Hamiltonian of the individual honeycomb layers is given by

$$\mathcal{H}^{(l)} = \int d^2r \sum_{\nu=\pm} \Psi_\nu^{\dagger(l)}(\mathbf{r}) \left[-iv\vec{\sigma}_\nu . \nabla + V_l \sigma_0 + m_l \sigma_3 \right] \Psi_\nu^{(l)}(\mathbf{r}) \tag{2.51}$$

where for each layer l, $\Psi = (\psi_a, \psi_b)$ are the two component spinors labelling sublattices, ν correspond to the two different valleys, $\vec{\sigma}_\nu = (\sigma_x, \nu\sigma_y)$, v is the Fermi velocity, V_l labels the scalar potential and m_l labels the mass on layer l. We shall consider the case where $m_1 = V_1 = 0$, $m_2 = m$ and $V_2 = V$. The interlayer Hamiltonian is given by

$$\mathcal{H}^{(12)} = \int d^2r \sum_{\alpha,\beta=a,b} \bar{\psi}_\alpha^{\dagger(1)}(\mathbf{r}) t_\perp(\mathbf{r}) \bar{\psi}_\beta^{(2)}(\mathbf{r}) + h.c. \tag{2.52}$$

where $t_\perp(\mathbf{r}) \approx t_\perp$ in the interlayer hopping amplitude and the fields $\bar{\psi}_\alpha^{(l)}(\mathbf{r}) = \sum_\nu u_{\alpha,\nu}^{(l)}(\mathbf{r}) \psi_{\alpha,\nu}(\mathbf{r})$ are related to the continuum fields $\psi_{\alpha,\nu}^{(l)}(\mathbf{r})$ by the Bloch wave function in layer l, [63–66]

$$u_{\alpha,\nu}^{(l)}(\mathbf{r}) = \frac{1}{\sqrt{3}} \sum_{m=1}^{3} e^{i\mathbf{K}_{\nu,m}^{(l)} \cdot (\mathbf{r} - \mathbf{r}_{0,\alpha}^{(l)})}. \tag{2.53}$$

Here, as shown in Fig. 2.6, $\mathbf{K}_{\nu,\delta}^{(l)}$ labels the reciprocal lattice vectors of the Brillouin zone corners that correspond to the three equivalent $\mathbf{K}$ points ($m = 1, 2, 3$) in a given valley ν in layer l, and $\mathbf{r}_{0,\alpha}^{(l)}$ labels the position of a given carbon atom on sublattice $\alpha = a, b$ on layer l. We shall allow for twisted configurations which will reflect in the reciprocal lattice vectors and the positions of carbon atoms. Using (2.53), we can rewrite (2.52) as

$$\mathcal{H}^{(12)} \equiv \int d^2r \sum_{\nu=\pm} \Psi_\nu^{\dagger(1)}(\mathbf{r}) \left[\hat{t}_\nu(\mathbf{r}) \right] \Psi_\nu^{(2)}(\mathbf{r}) + h.c., \tag{2.54}$$

where

$$\hat{t}_\nu^{\alpha,\beta}(\mathbf{r}) = \frac{t_\perp}{3} \sum_{m,m'} e^{i\mathbf{K}_{\nu,m}^{(2)}(\mathbf{r} - \mathbf{r}_{0\beta}^{(2)})} e^{-i\mathbf{K}_{\nu,m'}^{(1)}(\mathbf{r} - \mathbf{r}_{0\alpha}^{(1)})} \tag{2.55}$$

is the hopping matrix elements between the twisted layers [64]. Here $\mathbf{K}_{\nu,m}^{(1,2)}$ correspond to the $\mathbf{K}$ points one the two different layers, where one is rotated relative the other as shown in Fig. 2.6.

In the path integral approach, one can integrate out the fields corresponding to layer 2 to obtain
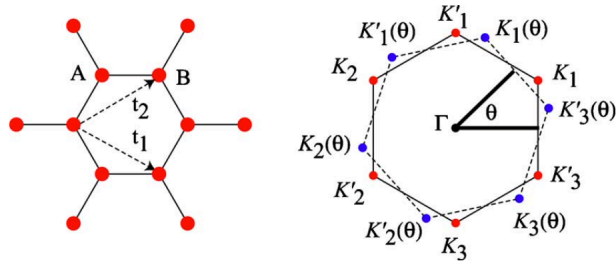
Figure 2.6: Left: Graphene lattice showing A and B sites in the primitive cell and primitive translations t_1 and t_2. Right: Brillouin zones for the two layers: the Brillouin zone corners labeled $\mathbf{K}_{1,2,3}$ correspond to the equivalent $\mathbf{K}$ points and $\mathbf{K}'_{1,2,3}(\theta)$ are the corresponding $\mathbf{K}$ points in the rotated layer [65].

an effective Hamiltonian for layer 1. Symbolically, the effective action is given by

$$
\begin{aligned}
\int D[\Psi_1]e^{S_{\mathrm{eff}}[\Psi_1]} &= \int D[\Psi_1]\left(\int D[\Psi_2]e^{S_1[\Psi_1,\Psi_2]}\right) \\
&= \int D[\Psi_1]e^{S_1[\Psi_1]}\left(\int D[\Psi_2]e^{S_2[\Psi_2]+S_{1-2}[\Psi_1,\Psi_2]}\right) \\
&= \int D[\Psi_1]e^{S_1[\Psi_1]}\left\langle e^{S_{1-2}[\Psi_1,\Psi_2]}\right\rangle_2,
\end{aligned}
$$

where $S_i[\Psi_i]$ is the action corresponding to Hamiltonian H_i and $S_{1-2}[\Psi_1,\Psi_2]$ correspond to the contribution to the action from the interlayer Hamiltonian (2.54). Using the cumulant expansion,

$$
\left\langle e^{\Omega}\right\rangle = e^{\langle\Omega\rangle+\frac{1}{2}\left(\langle\Omega^2\rangle-\langle\Omega\rangle^2\right)}+\ldots. \tag{2.56}
$$

Therefore,

$$
S_{\mathrm{eff}} = S_1 + \langle S_{1-2}\rangle_2 + \frac{1}{2}\left(\langle S_{1-2}^2\rangle_2 - \langle S_{1-2}\rangle_2^2\right)+\ldots, \tag{2.57}
$$

which is perturbative in $t_\perp$. The first correction $\langle S_{1-2}\rangle = 0$ and the second correction [79] computed in the limit $V \gg m$ gives

$$
\frac{1}{2}\left(\langle S_{1-2}^2\rangle_2 - \langle S_{1-2}\rangle_2^2\right) = \int_{\tau,\mathbf{r}}\sum_{\alpha=\pm}\Psi_\nu^{\dagger(l)}(\mathbf{r})\left[\hat{t}_\nu(\mathbf{r})\hat{M}\hat{t}_\nu^\dagger(\mathbf{r})\right]\Psi_\nu^{(l)}(\mathbf{r}),
$$

where

$$
\hat{M} = \frac{1}{m-V}\begin{pmatrix} \eta & 0 \\ 0 & 1 \end{pmatrix}, \tag{2.58}
$$

with $\eta = (V - m)/(V + m)$. For very small twist angles and in the first star approximation where backscattering process are restricted to the first Brillouin zone of the extended unit cell, the spatial modulation of the terms in the correction to the layer 1 Hamiltonian can be approximated to a sum over the three reciprocal lattice vectors of the moiré unit cell,

$$\hat{W}_\nu(\mathbf{r}) \equiv \hat{t}_\nu(\mathbf{r})\hat{M}\hat{t}_\nu^\dagger(\mathbf{r}) = \mu(\mathbf{r})\sigma_0 + \nu\mathbf{A}(\mathbf{r}) \cdot \vec{\sigma}_\nu + M(\mathbf{r})\sigma_3 \tag{2.59}$$

where μ, $\mathbf{A}$ and M are the local scalar, vector, and mass term potentials on layer 1 induced by layer 2, which spatially modulate with the moiré pattern. Thus the effective Hamiltonian for layer 1 can be written as

$$\mathcal{H}_1 = \int d^2 r \sum_{\nu=\pm} \Psi_\nu^{\dagger(1)}(\mathbf{r}) \left[-iv\vec{\sigma}_\nu \cdot \nabla + \hat{W}_\nu(\mathbf{r}) \right] \Psi_\nu^{(1)}(\mathbf{r}). \tag{2.60}$$

For more details, see [63, 64, 79].

As we saw above, application of a bias voltage between small angle twisted bilayer Dirac systems systems can lead to mass terms that vary with the periodicity of the moiré pattern. The interfaces that separate regions of positive and negative mass has $M(\mathbf{r}) = 0$ and in two dimensions correspond to domain walls, which are one dimensional objects. Outside the domain walls, the spectrum is fully gapped and are described by topological charges, N_3. For a generic Dirac Hamiltonian in a single valley, $H = \mathbf{g}(\mathbf{k}) \cdot \sigma$, where $\mathbf{g}(\mathbf{k}) = (k_x, k_y, M)$ and σ denoting the usual Pauli matrices,

$$\begin{aligned} N_3 &= \frac{1}{4\pi} \int dk_x dk_y \hat{g} \cdot (\partial_{k_x}\hat{g} \times \partial_{k_x}\hat{g}) \\ &= \frac{M}{2\,|M|} \end{aligned} \tag{2.61}$$

where $\hat{g} = \mathbf{g}/|\mathbf{g}|$. Though the spectrum of quasiparticles is fully gapped outside the domain wall, it can be gapless inside it, and due to the gap outside, all the low-temperature physics is determined by the gapless excitations living inside the topological object, that is the domain wall. The topological index theorem dictates that the number of gapless modes that live on the domain wall (n) is given by the difference in the topological index N_3 on either side of the domain wall,

$$n = \left| N_3(M^+) - N_3(M^-) \right|. \tag{2.62}$$
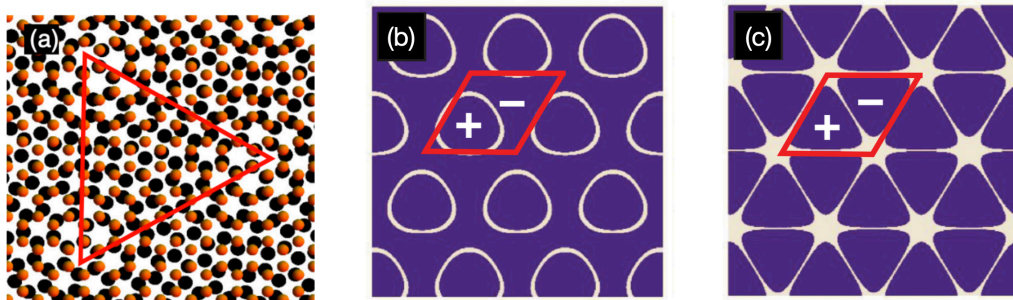
Figure 2.7: (a) moiré pattern of graphene on top of boron nitride. (b) Periodic mass term potentials induced on graphene by a gapped honeycomb substrate, such as BN or SiC. Solid rings are the regions where the mass potential crosses zero and changes sign. $+(-)$ indicates regions where the mass term is positive (negative). This corresponds to $\eta = -0.5$ in (2.58) . (c) $\eta = 1$, corresponding to the case of marginally twisted bilayer graphene [63, 79].

This implies $n = 1$ mode per valley. Taking into account both the valleys in graphene, this gives 2 modes per domain wall. If spin degree of freedom is also included a further degeneracy of 2 should also be included. Unless time several symmetry is broken, for example by a magnetic field, there will be equal number of left and right moving modes. We shall explicitly see this in section 2. 4. 1.

When layer 1 is graphene and layer 2 is gapped, as for instance in hexagonal boron nitride (h-BN) [79] or gapped graphene on silicon carbide [80], the numerically obtained $M(\mathbf{r})$ is shown in Fig. 2.7 (b) for $\eta = -0.5$. The interfaces where the mass term changes sign forms a lattice of disconnected quantum rings. As we cross these rings, the sign of the mass term changes from being positive inside the ring to negative in the regions between the rings. The rings therefore form domain walls. In this system, it has been proposed that interaction effects may lead to spontaneous formation of chiral loop currents in the bulk and a macroscopic spin-valley order may appear [79].

In recent times, in the context of moiré systems, twisted bilayer graphene at magic angles (for example, $\theta \sim 1.1°$) has been an area of active research. At these angles, the electronic bands become almost flat, thereby increasing electron-electron interaction effects leading to unconventional insulating and superconducting states[44, 45, 47–49]. At very low twist angles (marginal twist), $\theta \ll 1°$, the moiré pattern of bilayer graphene consists of triangular regions of AB (where A-type atoms of layer 1 overlap with B type atoms of layer 2) and BA stacking regions, separated by domain walls [50–52].

For biased twisted bilayer graphene at marginal angles, $m = 0$, $\eta = 1$, numerical calculations
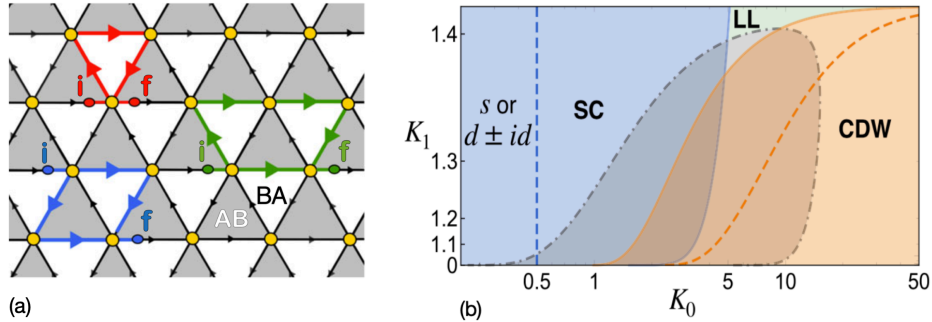
Figure 2.8: (a) Marginally twisted bilayer graphene depicted as a superlattice made of a triangular network of AB/BA domain walls, (b) Phase diagram obtained from a from a coupled Luttinger liquid description, where $K_{0,1}$ are phenomenological interaction parameters analogous to Eq. (2.42) [55, 56].

show that the mass term of the effective Hamiltonian changes sign along a triangular network of connected 1D channels [63], which is shown in Fig. 2.7 (c). The mass term has opposite signs in neighboring domains, which form an interconnected array of channels that percollate over the whole system, creating a metallic state. This pattern has been recently observed both in spectroscopy [50] and in magneto transport experiments [55] (for a discussion of the experimental moiré pattern, see [50] and the references therein). The latter report exceptionally strong Aharonov–Bohm oscillations arising from electron interference along the triangular loops formed by the domain walls. These results show that marginally twisted bilayer graphene is markedly distinct from bilayer graphene at larger twist angles.

Evidence for a triangular network of one dimensional arrays also paves way for a Luttinger liquid based analysis of marginally twisted bilayer graphene. In this context, very recently a detailed study of the electronic phases that could arise from triangular arrays of coupled quantum wires was done [56]. The analysis is phenomenological along the lines of section 2.2 and begins by considering marginally twisted bilayer graphene as a lattice of Luttinger liquids arranged in a triangular geometry. This is shown in Fig. 2.8 (a). As in section 2.2, after bosonizing the Luttinger liquid array and arriving at the smectic metal action, various perturbations such as interwire hopping, pair hopping between wires etc. are considered perturbatively. A renormalization-group calculation assessing the relevance of various processes showed that several strongly correlated phases can be occur in such a system including: superconductivity, charge density waves, a two-dimensional Fermi liquid, and a smectic metal phase. This model is expected to provide an effective description of marginally
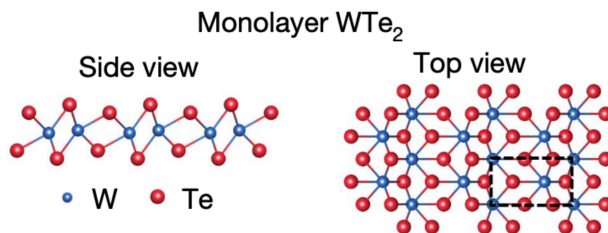
Figure 2.9: Lattice structure of WTe$_2$. [41].
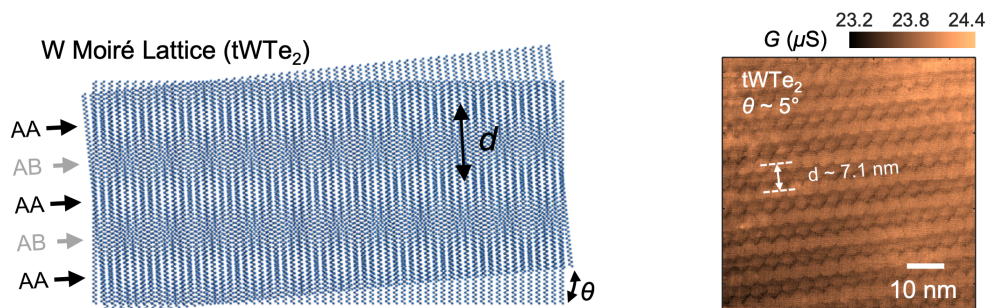
Figure 2.10: On the left is the moiré pattern formed by the W atoms, Te atoms are not shown and on the right is a conductive AFM image of the full moiré pattern. One dimensional channels can be clearly seen [41].

twisted bilayer graphene. The model and phase diagram obtained in [56] is shown in Fig. 2.8.

Another moiré system of recent experimental interest, which also partly motivates our work in the next section is that of twisted bilayer WTe$_2$ [41]. Monolayer WTe$_2$ shown in Fig. 2.9, is a three atomic layer thick system. The side view, shows a chain W atoms in between chains of Te atoms. From a top view, the Te atoms form a hexagonal pattern, with W atoms occupying positions slightly shifted from the center of the hexagon. The monolayer is thus highly anisotropic. High resolution STEM images show that, viewed from the top, the anisotropy in the monolayer leads to the lattice to resemble a collection of one dimensional stripes which are in fact zig-zag chains along the W atom chains[43]. Small angle twisted bilayer WTe$_2$ is six atomic layers thick and has a complicated structure. The experimental visualization of the full moiré pattern using conductive atomic force microscopy is shown in Fig. 2.10; moiré pattern resembling stripes can be easily seen. The distance between these stripes can be tuned by the twist angle and the distance between neighboring stripes is given as $d = a/2 \sin \frac{\theta}{2}$, where a is the length of the monolayers unit cell. For a twist angle $\theta \sim 5^\circ$, $d \sim 7.2$nm. Examined separately, at small twist angles, the Te atoms form a moiré pattern
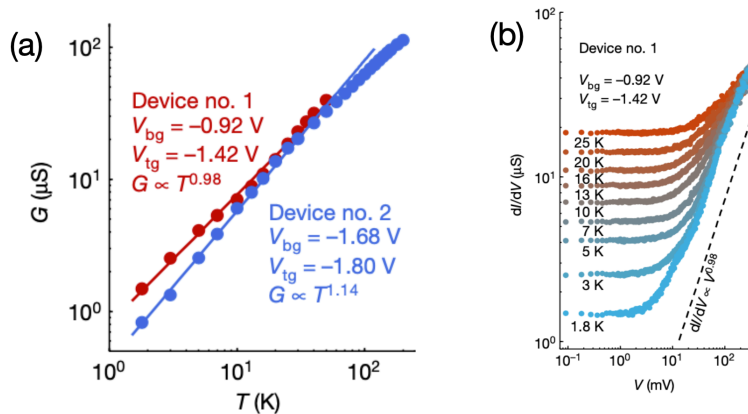
Figure 2.11: (a) Across wire conductance G as a function of temperature T plotted in log-log scale (b) Across-wire differential conductance dI/dV as a function of d.c. bias V for various temperatures. [41].

that resembles a triangular lattice whereas the W atoms form a moiré pattern of parallel stripes, as shown in Fig. 2.10. One can roughly imagine the moiré pattern as twisting two overlapping lattices of parallel zig-zag W atom chains leading to a moiré pattern of stripes perpendicular to the monolayer W atom chains.

In the experiment, the gates at each layer are controlled in such a way as to create a voltage difference between the layers. In the spirit of the effective description outlined before, integration of the degrees of freedom in one of the layers leads to effective local scalar potentials that modulate with the moire pattern and make the resulting electronic bands flat along the directions perpendicular to the stripes. Even though WTe$_2$ monolayer is a topological insulator [69–74], the metallic contacts are far away from the edges, whereas gating effects ensure that the system behaves as a metal, rather than an insulator in bulk.

Experimental transport results show that in the hole doped regime, there is a huge anisotropy in the transport measurements along perpendicular directions in the sample. Transport measurements along and across the wires indicate that individual stripes obey power law behaviors that resemble Luttinger liquids, whereas across wire measurements also indicate power law behaviors that are Luttinger liquid like with different power laws. These strongly indicate the possibility of the smectic metal phase being realized in this system. Fig. 2.11(a) shows across wire conductance G as a function of temperature T plotted in log-log scale and (b) shows across-wire differential conductance dI/dV as a function of d.c. bias V for various temperatures. These results show that $G \propto T^\alpha$ and

$dI/dV \propto V^{\alpha}$, where the exponent is the same for both measurements. This is strongly indicative of Luttinger liquid behavior across the wires[42]. Along the wires too, similar power law behavior with a different exponent α was obtained, although they are less robust due to contact effects that play an important role in the along-wire transport whereas across-wire transport is dominated by tWTe$_2$ bulk.

2.4 Effective microscopic model

Partly motivated by the experiment on twisted bilayer tWte$_2$[41], we study an effective microscopic model of parallel Luttinger liquids, where the wave-functions on individual wires and the interaction parameters within and between wires can be computed from the model. We draw a phase diagram for this system and analyze what part of the generic phenomenological phase diagram in Figs. 2.3 and 2.4 survives.

We construct a model for an array of parallel quantum wires using 2D Dirac fermions in the presence of a periodically modulated mass term. This potential confines the low energy quasiparticles to propagate along one dimensional channels, as depicted in Fig. 2.12. Incorporating intra-wire Coulomb interactions, these modes are shown to be tunable LL's, akin to the domain wall modes found in gated bilayer graphene [58, 59], in mono and bilayer graphene under irradiation [60], and also in other contexts [61–63]. When inter-wire Coulomb interactions are taken into account, the model realizes a smectic metal state, whose Luttinger parameters can be obtained in terms of effective microscopic quantities.

Even though the proposed model is topological, we suggest that it offers insight on the stability of the smectic phase for parallel quantum wires with non-topological origin, as in tWTe$_2$, and arrays of generic quantum wires with exponentially localized wavefunctions. This model naturally incorporates the lateral spread of the wave-functions ℓ in the perpendicular direction to the quantum wires. Employing well established abelian bosonization methods to account for the possible instabilities to the smectic fixed point, we show that only two phases remain in this model: a smectic metal state and a 2D Fermi liquid state. We point out that, while the absence of the insulating smectic (stripe) phase is due to the lack of backscattering in the model, superconductivity is shown to be always an irrelevant (or marginal) perturbation at the smectic fixed point.
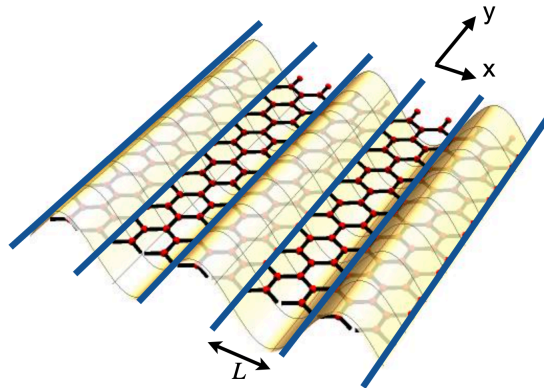
Figure 2.12: Cartoon representation of a periodic mass term (yellow wave form) on the honeycomb lattice. One dimensional modes at interfaces where the mass term changes sign are shown as thick blue lines. The transverse distance between these modes is L. The modes that live on the interface have a transverse width that dies off as $e^{-x^2/(2\ell^2)}$, with ℓ the lateral spread of the wavefunction (see text).

In the phase diagram, we find that the smectic metal and the Fermi liquid phases are separated by a quantum critical point set by a critical Coulomb coupling α_c, whose value is determined by the lateral spread ℓ and other microscopic parameters. For finite ℓ, the Fermi liquid phase is the leading instability in weak coupling $(\alpha < \alpha_c)$, while the smectic metal is dominant in the strong coupling regime $(\alpha > \alpha_c)$. The critical coupling vanishes in the ideal quantum wire limit $(\ell \to 0)$, where the smectic phase is always dominant. We finally discuss the role of weak backscattering effects in similar models.

2.4.1 Model

We consider a generic continuum model of 2D Dirac fermions with two valley flavors, as in the honeycomb lattice. Generalizations to other physical lattices with Dirac quasiparticles and an arbitrary number of valleys are straightforward. In real space, the free Hamiltonian is $\mathcal{H}_0 = \int d^2r \, \Psi_\sigma^\dagger(\mathbf{r}) \hat{\mathcal{H}}_0(\mathbf{r}) \Psi_\sigma(\mathbf{r})$, where

$$\hat{\mathcal{H}}_0(\mathbf{r}) = \begin{pmatrix} \hat{\mathcal{H}}_+ & 0 \\ 0 & \hat{\mathcal{H}}_- \end{pmatrix} \tag{2.63}$$

is a 4×4 matrix defined in the two valleys $\alpha = \pm$,

$$\mathcal{H}_\nu(\mathbf{r}) = -iv\sigma_x\partial_x - i\alpha v \sigma_y \partial_y + M(\mathbf{r})\sigma_z, \tag{2.64}$$

with σ_x and σ_y the off diagonal Pauli matrices in the pseudospin space. $\Psi_\sigma(\mathbf{r})$ is a four-component spinor with spin $\sigma = \uparrow, \downarrow$. The mass term profile is taken to be of the form

$$M(\mathbf{r}) = M_0 \sin\left(\frac{\pi x}{L}\right), \tag{2.65}$$

which breaks the continuous translational symmetry along the x direction. It is well known in the context of the index theorem that real space lines where the mass term changes sign are topological, hosting zero energy modes [67]. The mass term (2.65) is a periodic function that changes sign at the nodal lines where $M(\mathbf{r}) = 0$, forming an array of parallel quantum wires with spacing L shown in Fig. 2.10.

Before addressing the fate of the possible many-body phases in this system, we first compute the zero-modes that live on these nodal lines. To solve for the eigenvalues and eigenvectors of $\mathcal{H}_+(\mathbf{r})$, it is convenient to linearize Eq. (2.65) in the vicinity of a zero-mass line at $x = 0$ to get

$$M(\mathbf{r}) \approx M_0 \frac{\pi x}{L}. \tag{2.66}$$

The eigenvalue problem can be solved analytically by performing two sequential unitary transformations in the pseudospin [68]: a rotation by $-\pi/2$ around the z axis, that takes $\sigma_x \to \sigma_y$ and $\sigma_y \to -\sigma_x$, followed by a rotation by $\pi/2$ around the y axis, which takes $\sigma_x \to -\sigma_z$ and $\sigma_z \to \sigma_x$. In the transformed basis, the "+" block of the eigenvalue problem $\mathcal{H}(\mathbf{r})\Psi(\mathbf{r}) = E\Psi(\mathbf{r})$ can be written as

$$\omega \begin{pmatrix} \ell k_y & -\partial_\xi + \xi \\ \partial_\xi + \xi & -\ell k_y \end{pmatrix} \Phi_+(\xi) = E_+ \Phi_+(\xi), \tag{2.67}$$

where we have introduced variables $\ell = \sqrt{vL/(M_0\pi)}$, $\omega = v/\ell$ and $\xi = x/\ell$. Eq. (2.67) implicitly assumes the ansatz

$$\Psi_+(\mathbf{r}) = \frac{e^{ik_y y}}{\sqrt{L_y}} \begin{pmatrix} \Phi_+(\xi) \\ 0 \end{pmatrix} \tag{2.68}$$

due to translational symmetry in the y direction, with k_y the corresponding momentum and L_y the length of the quantum wires.

In this form, Eq. (2.67) resembles the problem of Dirac fermions in the presence of a uniform

magnetic field [75], ℓ being the analogue of the magnetic length. Defining the ladder operator $\mathcal{O} = (\partial_\xi + \xi)/\sqrt{2}$ such that $[\mathcal{O}, \mathcal{O}^\dagger] = 1$ and the number operator $\hat{N} = \mathcal{O}^\dagger \mathcal{O}$, one can easily infer that the eigenvalues are given by

$$E_{+,N}^{(\pm)}(k_y) = \pm\omega\sqrt{\ell^2 k_y^2 + 2N}, \tag{2.69}$$

where $N = 1, 2, \ldots$ indexing the gapped quantum wire modes, with the corresponding eigenvectors

$$\Phi_+^{N,\pm}(\xi) = \begin{pmatrix} \psi_N(\xi) \\ \pm\psi_{N-1}(\xi) \end{pmatrix}. \tag{2.70}$$

In a more explicit form, $\psi_N(\xi) = 2^{-\frac{N}{2}}/(\pi^{\frac{1}{4}}\sqrt{N!})e^{-\xi^2/2}H_N(\xi)$, where $H_N(\xi)$ is the N-th Hermite polynomial. The length ℓ hence determines the lateral spread of the wave-functions confined to the quantum wires. The solution of the $\Psi_-(\mathbf{r})$ eigenmodes in the opposite valley is related by time-reversal operation,

$$\Psi_{-,N}^{(\pm)}(\mathbf{r}) = \frac{e^{-ik_y y}}{\sqrt{L_y}} \begin{pmatrix} \mathbf{0} \\ \Phi_-^{N,\pm}(\xi) \end{pmatrix}, \tag{2.71}$$

with $\Phi_-^{N,\pm}(\xi) = (\psi_N(\xi), \pm\psi_{N-1}(\xi))^T$. The "$\pm$" upper index accounts for the two particle-hole branches in each valley.

The $N = 0$ case corresponds to the gapless zero energy modes moving along the quantum wires. This case requires a more careful analysis to resolve the seeming ambiguity between particle and hole states in Eq. (2.69). In valley $\alpha = +$, the x dependent part of the wavefunction $\Psi_+(x) = (\Phi_+^0(\xi), \mathbf{0})^T$ gives the four-component eigenvector for a single right moving mode (per spin) with energy dispersion

$$E_+(k_y) = vk_y. \tag{2.72}$$

That can be seen by plugging in $\Phi_+^0(\xi)$ into (2.67) and explicitly solving the resulting differential equation. The zero energy mode $\Psi_-(x) = (\mathbf{0}, \Phi_-^0(\xi))^T$ in the opposite valley corresponds to a left moving mode with energy $E_-(k_y) = -vk_y$, as required by time reversal symmetry.

2.4.2 Tunable LL's

To derive an effective one dimensional model, we assume a suitable energy cut off $v\Lambda$ below the bulk mass M_0 and focus on the gapless modes propagating along the quantum wires. We closely follow the LL derivation in Ref. [58, 60]. In the infrared, we restrict our interest to the gapless modes with $N = 0$, with k_y the small momentum in the vicinity of the two valleys, αK. The field operator becomes

$$\hat{\chi}_\sigma(\mathbf{r}) = \frac{1}{\sqrt{L_y}} \sum_{\alpha=\pm} e^{i\alpha K y} \Psi_\alpha(x) \hat{\zeta}_{\alpha,\sigma}(y) \tag{2.73}$$

where $\hat{\zeta}_{\alpha,\sigma}(y) = \sum_{k_y} e^{ik_y y} \hat{\zeta}_{\alpha,\sigma,k_y}$ is a slowly varying field operator for electrons in valley α moving along the wire. The non-interacting Hamiltonian is given by

$$\mathcal{H}_0 = v \sum_{k_y,\sigma,\alpha} \alpha k_y \hat{\zeta}_{\alpha,\sigma}^\dagger(k_y) \hat{\zeta}_{\alpha,\sigma}(k_y). \tag{2.74}$$

The effective Coulomb interaction projected onto the one dimensional modes can be obtained by substituting (2.73) into the Coulomb interaction term $\mathcal{H}_{I,\text{intra}} = \frac{1}{2} \sum_{\sigma,\sigma'} \int_{\mathbf{r},\mathbf{r}'} \hat{\rho}(\mathbf{r}) V(\mathbf{r} - \mathbf{r}') \hat{\rho}(\mathbf{r}')$, defined in terms of density operators $\hat{\rho}(\mathbf{r}) = \sum_\sigma \hat{\chi}_\sigma^\dagger(\mathbf{r}) \hat{\chi}_\sigma(\mathbf{r})$. Here, $V(\mathbf{r}) = e^2 e^{-r/\lambda}/r$ is a screened Coulomb interaction, with screening length λ set by metallic contacts with the wires.

We note that the orthogonality of the spinors $\Psi_+(x)$ and $\Psi_-(x)$ suppresses backscattering in this model, unlike in conventional LLs. Since $\hat{\zeta}_{\alpha,\sigma}(y)$ are slow varying fields, the effective intra-wire interaction can be approximated by

$$\mathcal{H}_{I,\text{intra}} \approx \int_y \sum_{\alpha\beta} g_{\alpha\beta} \hat{\zeta}_{\alpha,\sigma}^\dagger(y) \hat{\zeta}_{\beta,\sigma'}^\dagger(y) \hat{\zeta}_{\beta,\sigma'}(y) \hat{\zeta}_{\alpha,\sigma}(y), \tag{2.75}$$

with

$$g_{\alpha\beta} = \frac{1}{2} \int_{x,x'} \int_{\bar{y}} V(x - x', \bar{y}) |\psi_0(x)|^2 |\psi_0(x')|^2, \tag{2.76}$$

where $\bar{y} = y - y'$. Using the standard g-ology notation in the LL literature, the denote $g_{+-} = g_{-+} = g_2$ and $g_{--} = g_{++} = g_4$, which turn out to be the same, $g_2 = g_4$. This is not a coincidence, but a manifestation of the chiral symmetry of the problem in the forward scattering terms. The equality between g_2 and g_4 also implies in the absence of current-current interaction terms.

The interaction term can be written explicitly in terms of density operators,

$$\mathcal{H}_{I,\text{intra}} = \int dy g_4 \left[\rho_+(y) + \rho_-(y)\right]^2 = \frac{2g_4}{\pi} \int dx \left(\partial_x \Phi_\rho\right)^2, \tag{2.77}$$

where

$$g_4 \left(\frac{e^2}{\epsilon_0}, \ell\right) = \frac{1}{2} \int_{x,x'} \int_{\bar{y}} V(x - x', \bar{y}) \left|\psi_0(x)\right|^2 \left|\psi_0(x')\right|^2$$

and $V(\mathbf{r}) = (e^2/\epsilon_0)e^{-r/\lambda}/r$ the screened Coulomb interaction, with Φ_ρ defined as below. In order to bosonize the fermionic Hamiltonian, we follow the abelian bosonization convention in [16, 38]. The fermionic fields for left and right moving modes

$$\hat{\zeta}_{\alpha,\sigma}(y) \sim e^{i\alpha\sqrt{\pi}[\phi_\sigma(y) - \alpha\theta_\sigma(y)]} \tag{2.78}$$

are cast in terms of the two bosonic fields $\phi_\sigma(y)$ and $\theta_\sigma(y)$. The Hamiltonian $\mathcal{H}_{\text{intra}} = \mathcal{H}_0 + \mathcal{H}_{I,\text{intra}}$ written in terms of charge (ρ) and spin (σ) variables exhibit spin-charge separation,

$$\mathcal{H}_{\rho,\sigma} = \frac{1}{2} \int dy \left[(\partial_y \Theta_{\rho,\sigma})^2 \frac{u_{\rho,\sigma}}{K_{\rho,\sigma}} + (\partial_y \Phi_{\rho,\sigma})^2 u_{\rho,\sigma} K_{\rho,\sigma}\right], \tag{2.79}$$

where $\Theta_{\rho,\sigma}(y) = [\theta^\uparrow(y) \pm \theta^\downarrow(y)]/\sqrt{2}$ and $\Phi_{\rho,\sigma}(y) = [\phi^\uparrow(y) \pm \phi^\downarrow(y)]/\sqrt{2}$. The Luttinger parameters are given by $u_{\rho,\sigma} = v$, $K_\sigma = 1$ and $K_\rho = [1 + 2sg_4/(\pi v)]^{\frac{1}{2}}$. In the above, $s = 2$. In the case of spin-less fermions, the spin part of $\mathcal{H}_{\text{intra}}$ is absent and $s = 1$. The LL stiffness in the charge sector K_ρ can be controlled by tuning the lateral spread of the wave-functions ℓ through the coupling g_4. The one dimensional modes that live on the nodal lines thus form a lattice of decoupled LLs.

2.4.3 Smectic metal

It was pointed out in Ref. [38–40] that the inclusion of inter-wire density-density and current-current interactions can still be treated exactly in the bosonization formalism, leading to what is called a generalized smectic metal.

The density-density interaction between wires follows from $\mathcal{H}_{\text{intra}}^I$ after incorporating the wire index a for the superlattice into the wave-functions and $\hat{\xi}_{\alpha,\sigma}^a(y)$ operators, and hence into the

definition of the field operators,

$$\hat{\chi}_{\sigma,a}(\mathbf{r}) = \sum_{\alpha=\pm} e^{i\alpha K y} \Psi_{\alpha,\sigma}(x_a) \hat{\zeta}^a_{\alpha,\sigma}(y), \tag{2.80}$$

with $x_a \equiv x - X_a$ the relative coordinate to wire a. In line with [38–40], we only consider the coupling of charge densities between wires and not the exchange coupling, which is small when $\ell/L \ll 1$, with L the inter-wire distance. Thus,

$$\mathcal{H}_{\text{inter}} = \frac{1}{2} \sum_{a \neq a'} \int_{\mathbf{r},\mathbf{r}'} V(\mathbf{r} - \mathbf{r}') \rho_a(\mathbf{r}) \rho_{a'}(\mathbf{r}'). \tag{2.81}$$

From the bosonization identities, we can write this as an effective one dimensional density density interaction,

$$\mathcal{H}_{\text{inter}} = \frac{2}{\pi} \int_y \sum_{a \neq a'} U_{a,a'} \left[\partial_y \Phi_{\rho,a}(y) \right] \left[\partial_y \Phi_{\rho,a'}(y) \right], \tag{2.82}$$

where

$$U_{a,a'} = \frac{1}{2} \int_{x,x',\bar{y}} V(x - x', \bar{y}) \left| \psi_0(x_a) \right|^2 \left| \psi_0(x'_{a'}) \right|^2. \tag{2.83}$$

Thus only the charge sector is modified by the inter-wire interaction. Eq. (2.79) and (2.82) define the Hamiltonian of the smectic metal and are invariant under $\Phi_{\rho,a}(y) \to \Phi_{\rho,a}(y) + c_{\rho,a}$, $\Theta_{\rho,a}(y) \to \Theta_{\rho,a}(y) + d_{\rho,a}$, where $c_{\rho,a}, d_{\rho,a}$ are independent constants on each LL. This property defines *the sliding* symmetry in arrays of LLs [39].

For the charge variables, before introducing inter-wire interactions, as shown above,

$$\mathcal{H}^{\rho} = \frac{1}{2} \int dy \left\{ \left(\partial_y \Theta^a_\rho \right)^2 \frac{u^\rho}{K^\rho} + \left(\partial_y \Phi^a_\rho \right)^2 u^\rho K^\rho \right\} \tag{2.84}$$

where

$$\frac{u^\rho}{K^\rho} = v \tag{2.85}$$

$$u^\rho K^\rho = v \left[1 + \frac{2 s g_4}{\pi \gamma} \right]. \tag{2.86}$$

The spin part is unaffected. The inter-wire interaction contributes an extra term to the charge part

as shown in (2.82),

$$
\begin{aligned}
\mathcal{H}^\rho_{int} &= \frac{1}{\pi} \int_y \sum_{a,a'} U_0(a-a') \left[\partial_y \Phi^a_\rho(y)\right] \left[\partial_y \Phi^{a'}_\rho(y)\right] &\text{(2.87)} \\
&= \frac{2}{\pi} \int_y \sum_a \{ g_4 \left[\partial_y \Phi^a_\rho(y)\right] \left[\partial_y \Phi^a_\rho(y)\right] &\text{(2.88)} \\
&\quad + V_1 \left[\partial_y \Phi^a_\rho(y)\right] \left[\partial_y \Phi^{a+1}_\rho(y)\right] + V_1 \left[\partial_y \Phi^a_\rho(y)\right] \left[\partial_y \Phi^{a-1}_\rho(y)\right] \} &\text{(2.89)}
\end{aligned}
$$

where we have restricted $\sum_{a,a'}$ to sum over nearest neighbors. The casting the LL Hamiltonian together with the bosonized interaction term among different wires, we have

$$
\begin{aligned}
\mathcal{H}^\rho &= \int_{k,k_\perp} \frac{1}{2} \left[v k^2 \Theta_\rho(\mathbf{k})\Theta_\rho(-\mathbf{k}) + \left[v + \frac{2}{\pi} s g_4 + \frac{s}{\pi} 4 V_1 \cos k_\perp L \right] k^2 \Phi_\rho(\mathbf{k})\Phi_\rho(-\mathbf{k}) \right] \\
&\equiv \int_{k,k_\perp} \frac{1}{2} \left[\frac{u^\rho}{K^\rho} k^2 \Theta_\rho(\mathbf{k})\Theta_\rho(-\mathbf{k}) + u^\rho K^\rho k^2 \Phi_\rho(\mathbf{k})\Phi_\rho(-\mathbf{k}) \right] &\text{(2.90)}
\end{aligned}
$$

where

$$
\begin{aligned}
\frac{u^\rho(k_\perp)}{K^\rho(k_\perp)} &= v \\
u^\rho(k_\perp) K^\rho(k_\perp) &= v + \frac{1}{\pi} 2 s g_4 + \frac{1}{\pi} 4 s V_1 \cos k_\perp L &\text{(2.91)}
\end{aligned}
$$

and $V_1 \equiv U_{a'=a\pm1}$ is the nearest neighbor interwire repulsion as defined in Eq. (2.83). The action for the spin and charge degrees of freedom can be obtained by integrating out the $\Theta^{\rho,\sigma}$ fields. This yield

$$
\begin{aligned}
\mathcal{S}^\sigma &= \int_{k,k_\perp,\omega} \frac{K^\sigma}{2} \left(\frac{\omega^2}{u_\sigma} + u^\sigma k^2 \right) |\Phi_\sigma(\mathbf{k})|^2 &\text{(2.92)} \\
\mathcal{S}^\rho &= \int_{k,k_\perp,\omega} \frac{K^\rho(k_\perp)}{2} \left(\frac{\omega^2}{u^\rho(k_\perp)} + u^\rho(k_\perp) k^2 \right) |\Phi_\rho(\mathbf{k})|^2 &\text{(2.93)}
\end{aligned}
$$

where $u^\sigma = v$, $K^\sigma = 1$, as before, and $\int_{k,k_\perp,\omega} \equiv L/(2\pi)^3 \int_{-\infty}^\infty d\omega dk \int_{-\pi/L}^{\pi/L} dk_\perp$. Luttinger parameters of the charge sector acquire momentum dependence from (2.82). Stability of the theory requires these parameters to be positive. We restrict the sum in (2.82) to nearest neighbor interactions as in [38]. In the above expressions, we defined $\mathbf{k} = (\omega, k, k_\perp)$, $s = 2$. In the spin-less case, $s = 1$ and the spin part of the action S^σ is absent. In comparison with the notation in [38],

$\left(\frac{u^{\rho}(k_{\perp})}{K^{\rho}(k_{\perp})}\right)^{-1} = W_0(k_{\perp})$ and $u^{\rho}(k_{\perp})K^{\rho}(k_{\perp}) = W_1(k_{\perp})$. The parameter that decides the phase diagram $\kappa = \sqrt{W_0(k_{\perp})W_1(k_{\perp})}$.

2.4.4 Phase diagram

The stability of the smectic metal state to various instabilities has to be assessed via a renormalization group (RG) analysis of the relevant perturbations. Vast literature exist on the RG analysis of the smectic fixed point [38–40]. Therefore we do not repeat the analysis here, but adapt their RG equations to our model. The potentially relevant interactions in this case are nearest neighbor single electron tunneling ($\mathcal{H}_t$), nearest neighbor singlet pair (Josephson) tunneling ($\mathcal{H}_{sc}$), and the coupling between the charge density wave (CDW) order parameters. As mentioned before, due to the absence of backscattering, the interaction between CDW order parameters are absent in our model. The former two are given by

$$\mathcal{H}_t = \mathcal{T} \sum_{a,\alpha,\sigma} \int dx \, \hat{\zeta}^{\dagger a}_{\alpha,\sigma} \hat{\zeta}^{a+1}_{\alpha,\sigma} + h.c. \tag{2.94}$$

$$\mathcal{H}_{sc} = \mathcal{J} \sum_{a,\alpha,\alpha'} \int dx \, \hat{\zeta}^{\dagger a}_{\alpha,\uparrow} \hat{\zeta}^{\dagger a}_{-\alpha,\downarrow} \hat{\zeta}^{a+1}_{\alpha',\downarrow} \hat{\zeta}^{a+1}_{-\alpha',\uparrow} + h.c. \,, \tag{2.95}$$

where $\mathcal{T}$ and $\mathcal{J}$ are the single particle and Josephson tunneling amplitudes, respectively.

These perturbations become relevant when their scaling dimensions, $\eta_X = 2 - \triangle_X > 0$ for $X = t, sc$. These scaling dimensions obtained from a one loop RG analysis in the spin-less case are,

$$\triangle_{sc} = \int_{-\pi}^{\pi} \frac{dk_{\perp}}{2\pi} \left[2\kappa(k_{\perp})\right] (1 - \cos k_{\perp}) \tag{2.96}$$

$$\triangle_t = \frac{1}{4} \int_{-\pi}^{\pi} \frac{dk_{\perp}}{2\pi} 2 \left[\kappa(k_{\perp}) + \kappa^{-1}(k_{\perp})\right] (1 - \cos k_{\perp}), \tag{2.97}$$

where in the present model

$$\kappa(k_{\perp}) = \sqrt{\left(1 + \frac{2sg_4}{\pi v} + \frac{4sV_1}{\pi v} \cos k_{\perp}\right)}. \tag{2.98}$$

In the spinful case, $\triangle^{\text{spin}}_{sc} = 1 + \frac{1}{2}\triangle_{sc}$ and $\triangle^{\text{spin}}_t = \frac{1}{2} + \frac{1}{2}\triangle_t$. Notice that, for the spin-less case here there is an extra factor of 2, compared to [38]. This is because we consider a spin-less case as
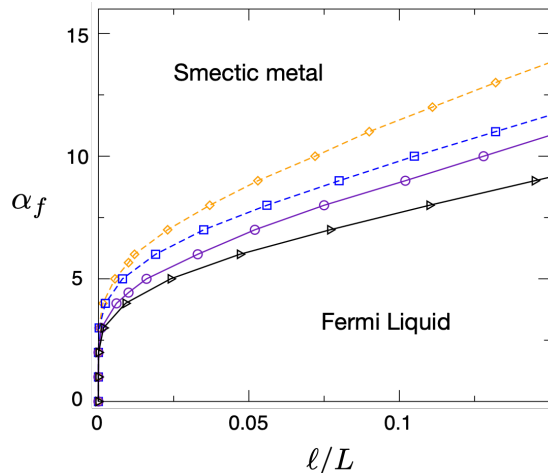
Figure 2.13: Fine structure constant $\alpha_f = e^2/(\epsilon v)$ vs lateral spread of the wave-functions in the quantum wires, ℓ, normalized by the inter-wire separation L. Curves show the boundary between the Fermi liquid and smectic metal phases. Black triangles and purple circles: spin-less particles for $\lambda/L = 0.5$ and 1, respectively. Blue square and orange diamonds: spinful case for $\lambda/L = 0.5$ and 1, respectively.

opposed to the spin gapped case considered in high-T_c like scenarios.

We plot in Fig. 2.13 the regions where these perturbations are relevant as a function of fine structure constant, $\alpha_f = e^2/(\epsilon v)$ and the dimensionless lateral spread of the wavefunction in the wires, ℓ/L. We restrict the analysis to the regime $\ell/L \ll 1$, where the smectic action is stable. There is no part of the phase diagram where superconductivity is relevant. It has been phenomenologically proposed that superconductivity may result in *active* environments, such as in high-T_c scenarios [76]. In the present model, the minimum value of $\triangle_{sc}$ is 2, making it marginal at best. A similar conclusion is applicable to non-topological quantum wires with repulsive interactions whenever $g_4 \gg V_1$.

The curves in the plot describe the critical coupling α_c separating the regions where the smectic metal and the Fermi liquid phases emerge. As previously announced, the 2D Fermi liquid phase is the dominant instability in the weak coupling regime, when $\alpha_f < \alpha_c$, whereas the smectic metal phase is the most relevant perturbation in strong coupling, $\alpha_f > \alpha_c$. The quantum critical phase transition collapses in the $\ell \to 0$ limit, where α_c scales to zero. That limit corresponds to the physical situation where the amplitude of the mass term in (2.65) $M_0 \gg vL$. The solid lines describe the spin-less case, when the screening length $\lambda/L = 0.5$ (black triangles) and 1 (purple circles). The other two dashed curves correspond to the spinful case for $\lambda/L = 0.5$ (blue squares) and 1 (orange diamonds). The modifications that can happen to our predictions in a model where backscattering

is non-zero, is discussed next.

2.4.5 Backscattering effects

Orthogonality between left and right modes eliminates backscattering in the present model. It is worth remarking that in a more general model, where there is backscattering, the phase diagram will comprise of regions where CDW coupling is the most relevant one. In lattice models with Dirac fermions, a finite but very small amount of backscattering is expected [58]. Backscattering is also expected in tWTe$_2$ bilayers and in layered van der Waals material NbSi$_{0.45}$Te$_2$ [77], where a non-symmorphic symmetry protects directional massless Dirac fermions that form equally spaced 1D channels in the bulk of the material, akin to stripes.

If present, intra-wire backscattering is known to renormalize the Luttinger parameters and introduce an irrelevant perturbation (for repulsive interactions) in the spin channel [15, 16]. Backscattering between quantum wires, however, can be relevant and may open a CDW gap at zero temperature. For completeness, we briefly look at the role of intrawire backscattering in this subsection. In the spinless case, it is well known that backscattering of the form $H_{back} = g_1 \int dx \zeta_+^\dagger(x) \zeta_-^\dagger(x) \zeta_+(x) \zeta_-(x)$ can be rewritten as forward scattering term, thereby amounting only to a redefinition of the Luttinger parameters [15],

$$\frac{u}{K} = v_F \left[1 - \frac{g_1}{2\pi v_F} \right], \qquad uK = v_F \left[1 + \left(\frac{2g_4 + g_1/2}{\pi v_F} \right) \right] \qquad (2.99)$$

In the spinful case however, the backscattering term takes the form [15]

$$H_{g_1} = -g_1^\parallel \int dx \zeta_{-,\sigma}^\dagger(x) \zeta_{-,\sigma}(x) \zeta_{+,\sigma}^\dagger(x) \zeta_{+,\sigma}(x) + g_1^\perp \int dx \zeta_{-,\sigma}^\dagger(x) \zeta_{+,\sigma}(x) \zeta_{+,-\sigma}^\dagger(x) \zeta_{-,-\sigma}(x) \quad (2.100)$$

Upon bosonization of this interaction, $g_1^\perp$ leads to a cosine interaction of the form

$$H_{g_1^\perp} = \frac{g_1^\perp}{(2\pi\alpha)^2} \cos\left(2\sqrt{2\pi} \Phi^\sigma \right)$$

whereas, $g_1^\parallel$ gets absorbed into the Luttinger parameters, giving

$$\frac{u^\rho}{K^\rho} = v_F \left[1 + \frac{g_1^\parallel}{2\pi v_F} \right], \qquad u^\rho K^\rho = v_F \left[1 + \frac{4g_4}{\pi v_F} - \frac{g_1^\parallel}{2\pi v_F} \right] \qquad (2.101)$$

for the charge sector and

$$\frac{u^\sigma}{K^\sigma} = v_F \left[1 + \frac{g_1^\parallel}{2\pi v_F} \right], \qquad u^\sigma K^\sigma = v_F \left[1 - \frac{g_1^\parallel}{2\pi v_F} \right] \tag{2.102}$$

for the spin one.

The RG scaling dimension of the interaction $H_{g_1^\perp}$ is $\triangle_{g_1^\perp} > 2$ generally for repulsive interactions and therefore these processes are irrelevant [16]. Therefore the spin sector remains gapless, and there is no ordering. Umklapp interactions, on the other hand, are relevant for repulsive interactions and can open a CDW gap [16]. These have a non-zero amplitude only precisely at half filling and can be ignored in experimental settings where the chemical potential can be tuned at will.

The interwire coupling between wires that leads to a CDW state has the form

$$\mathcal{H}_{cdw} = g_{cdw} \sum_{a,\alpha,\sigma,\sigma'} \int dx \hat{\zeta}^{\dagger a}_{\alpha,\sigma} \hat{\zeta}^{a}_{-\alpha,\sigma} \hat{\zeta}^{\dagger a+1}_{-\alpha,\sigma'} \hat{\zeta}^{a+1}_{\alpha,\sigma'}.$$

From the lowest order RG analysis, this operator becomes relevant when $\eta_{cdw} = 2 - \triangle_{cdw} > 0$. For the spinless case, this is given by

$$\triangle_{cdw} = \int_{-\pi}^{\pi} \frac{dk_\perp}{2\pi} \left[2\kappa (k_\perp)^{-1} \right] (1 - \cos k_\perp) \tag{2.103}$$

where $\kappa (k_\perp)$ is defined in the main text. For the spinful case, $\triangle_{cdw}^{\mathrm{spin}} = 1 + \frac{1}{2}\triangle_{cdw}$. The plot in Fig. 2.14 shows the regions in the phase diagram where the operators corresponding to CDW, SC and Fermi liquid phases become relevant, as a function of the fine structure constant α_f and the ratio ℓ/L. In the model considered in the in the previous section, $g_{cdw} = 0$ due to orthogonality between left and right modes. In lattice models that can be approximated by the continuum model discussed in the in the previous section, g_{cdw} can be non-zero, although still small. We see that compared to the case described earlier, the smectic metal phase now gives way for a more relevant CDW state at zero temperature.

As pointed out before, in models where the backscattering term g_{cdw} is parametrically small compared to forward scattering terms g_2 and g_4 to begin with, the CDW gap is only observable at very small temperature [58]. In the RG spirit, temperature plays a role of an infrared cut-off , where the RG flow stops. Since g_{cdw} is a marginal operator at the tree level ($g_2 = g_4 = 0$), it grows
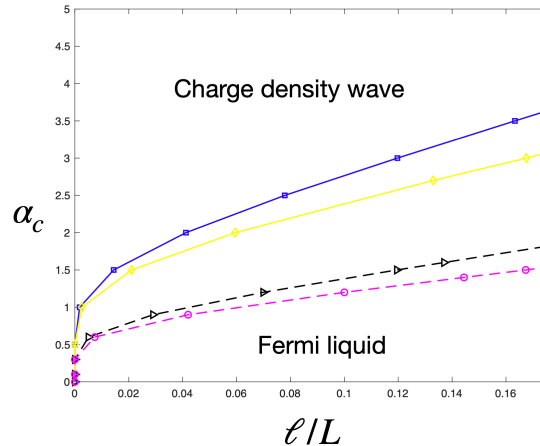
Figure 2.14: Zero temperature phase diagram in the presence of interwire backscattering. Black triangles and magenta circles: spinless particles for $\lambda/L = 0.5$ and 1, respectively. Blue square and yellow diamonds: spinful case for $\lambda/L = 0.5$ and 1, respectively.

under the RG only logarithmically under rescaling of the momenta and fields,

$$g_{cdw}(T) = g_{cdw}(\Lambda_T) + \eta_{cdw} \ln\left(\frac{\Lambda_T}{T}\right), \qquad (2.104)$$

where Λ_T is some ultraviolet temperature cut-off, with $g_{cdw}(\Lambda_T) \ll g_2, g_4$. Hence, g_{cdw} becomes dominant over forward scattering processes near zero temperature, somewhere in the limit where temperature $T/\Lambda_T \to 0$.

Hence, in models that have parametrically weak backscattering to begin with, the CDW gap is experimentally observable only at very low temperature [58]. Those models admit an experimentally accessible temperature $k_B T_* \ll g_2, g_4$ above which the CDW order is subdominant, avoring either a smectic metal or Fermi liquid phases, even when backscattering is the most relevant perturbation. This seems to be the case in tWTe$_2$, where a smectic metal phase was observed down to 1.8K [41]. We predict that placing tWTe$_2$ on a dielectric substrate at fixed $T > T_*$ could destabilize the smectic metal towards a Fermi liquid phase.

The properties of those two phases, smectic metal and Fermi liquid, are rather well known. While the Fermi liquid state is the most general many particle state in two or three dimensions, the smectic metal state is a rather peculiar state of matter. In a smectic metal, there is large longitudinal conductivity in each quantum wire, but transport is incoherent in the transverse direction due to the irrelevance of inter-wire hopping. In the absence of disorder, resistivity along the wires $\rho_{yy} = 0$.

Small amounts of disorder, which are present in realistic samples, can introduce backscattering and lead to a temperature dependence $\rho_{yy} \sim T^{\alpha_\parallel}$, where $\alpha_\parallel = \left[\int_{-\pi}^{\pi} \frac{dk_\perp}{2\pi} \kappa \left(k_\perp\right)^{-1} \right] - 2$ [38, 40, 78]. On the other hand, in the transverse direction, conductivity is still given by a power law, $\sigma_{xx} \sim T^{\alpha_\perp}$, where the exponent $\alpha_\perp$ depends on the details of single particle hopping and Josephson couplings [40].

2.4.6 Conclusion

We considered an effective microscopic model for an array of parallel quantum wires in 2D that accounts for the lateral spread of the wave-functions ℓ in the transverse direction to the wires. The model lacks backscattering, and does not lead to a stripe phase. Using standard abelian bosonization and RG methods, we calculated the Luttinger parameters of the sliding LL phase in terms of microscopic parameters and analyzed what known instabilities of the smectic fixed point (previously found phenomenologically) actually survive. We showed that the smectic metal phase is stable in the ideal quantum wire limit, and survives at finite ℓ beyond a critical Coulomb coupling α_c that grows monotonically with ℓ. In weak coupling ($\alpha < \alpha_c$), this model describes a 2D Fermi liquid, with the wave-functions in the quantum wires percolating over the whole system. We find that superconductivity is absent, a feature that is expected to be generic of similar models. We also discussed the effects of possible weak backscattering.

Chapter 3

The SYK model and extensions

The Sachdev-Ye-Kitaev (SYK) model of fermions with random interactions between them has received wide attention recently. SYK_q models describe strongly interacting fermions with infinite range, $q-$body, random all-to-all interactions. The $0 + 1$ dimensional SYK_q dot model [85, 86] exhibits an approximate conformal symmetry in the infrared, is exactly solvable in the limit of a large number of fermion flavors. The SYK model is also known to be maximally chaotic. Chaos is characterized by the Lyapunov exponent, which can be computed using the out of time ordered four point correlation function [92, 93]. An upper bound has been conjectured for the Lyapunov exponent, and the SYK model saturates this bound[89]. The model has also been shown to be dual to gravitational theories in $1 + 1$ dimensions. [87–89]. The Lyapunov exponent of a black hole in Einstein gravity also saturates the chaos bound[87, 88]. Useful connections to the black hole information problem have also been established [90].

In these models, approximate conformal symmetry in the strong coupling/low frequency regime leads to power law behavior of correlation functions. In the SYK_4 model, the zero temperature two-point correlation function decays as $G(\omega) \sim 1/\sqrt{\omega}$, with ω the frequency. Finite temperature Green's functions can be then obtained by appealing to conformal symmetry [85]. In dispersive versions of the SYK model, they result in the linear temperature dependence of the dc resistivity, $\rho \propto T$, a characteristic feature of strange metal phases. It was originally conjectured that the linear scaling of the scattering rate in the strange metal phase was due to hyper-scaling in the proximity of a quantum critical point buried inside the superconducting phase. Recent momentum resolved electron energy spectroscopy experiments in the cuprates revealed the emergence of a mysterious

momentum independent energy scale nearly one order of magnitude larger than the temperature range of the quantum critical fan [98, 99], at odds with conventional quantum critical theories. One may speculate [100–104] that the origin of the strange metal phase could be related to aspects of the physics of incoherent metals.

Various lattice generalizations [104–106, 111–113] of the dot model comprising of connected SYK dots have been recently proposed in the regime where the SYK coupling is the dominant energy scale of the problem. The general idea behind many of those extensions is to build on the solution of the dot model including lattice effects perturbatively. Weakly dispersive versions of the SYK model were used to describe incoherent or 'Planckian' metals which lack well defined quasiparticles [103, 114, 115]. These incoherent metals typically have a crossover between the incoherent high temperature regime and a low temperature Fermi liquid behavior [106, 111]. The crossover energy scale between the two regimes is set by t^2/J, with t proportional to the band width and $J \gg t$ the SYK coupling. In the low temperature regime, the coherence of the quasiparticles is restored by the presence of a large Fermi surface. Semimetals, on the other hand, abridge a large class of gapless multi-band systems that lack a Fermi surface. One could then ask what is the nature of the normal state in a disordered semimetal with random local couplings. We address this question in the next chapter.

This chapter provides an introduction to the properties of SYK models. We begin with an introduction to the $0 + 1$ dimensional SYK$_4$ dot model and discuss its basic properties. We then review the literature on lattice extensions of this model and discuss their transport properties. We also review the recent experimental proposal for realizing this model on a graphene flake.

3.1 Introduction

The $0 + 1$ dimensional SYK$_4$ dot model describes N fermions in a quantum dot [85, 106]. Since there is no spatial structure, the Hamiltonian of this model consist only of an interaction term, describing interactions between the fermions in the quantum dot. The interaction is special: the amplitude for each process is a random complex number. Fig. 3.1 schematically shows the model.
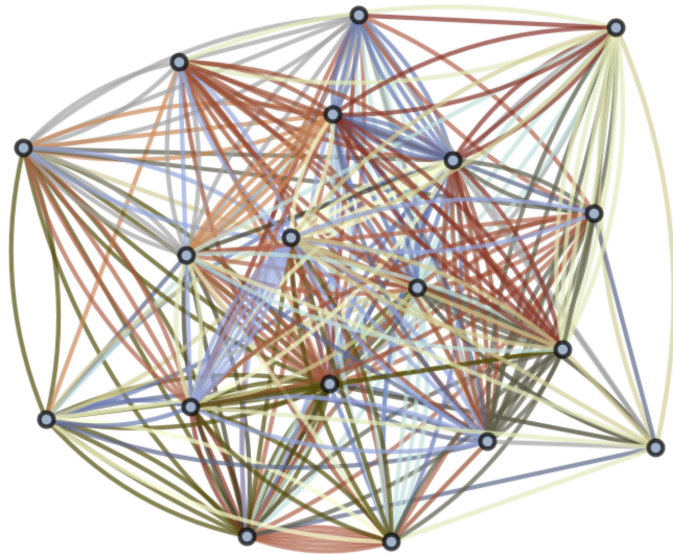
Figure 3.1: The SYK dot model. Each dot corresponds to a fermion flavor. The lines indicate the random interactions.[91]

The Hamiltonian for this model is given by

$$\mathcal{H} = \frac{1}{(2N)^{\frac{3}{2}}} \sum_{ijkl=1}^{N} J_{ijkl} c_i^\dagger c_j^\dagger c_k c_l - \mu \sum_i c_i^\dagger c_i \tag{3.1}$$

where $c_j^\dagger$ creates a fermion of flavor j. J_{ijkl} are complex, independent Gaussian random couplings with zero mean and variance $|J_{ijkl}|^2 = J^2$. The basic object of the theory that helps compute physical observables is the the 2-point correlation function or the Green's function. Since the Hamiltonian has disorder in it, we need to average over the disorder, while calculating physical observables. This is accomplished using the replica trick. The disorder averaging process is reviewed in Appendix C. In the path integral approach, the Green's function is defined as,

$$G(\tau_1 - \tau_2) = -\frac{1}{N} \sum_i \left\langle T_\tau \left(c_i(\tau_1) c_i^\dagger(\tau_2) \right) \right\rangle \tag{3.2}$$

where $\langle ... \rangle$ denotes the thermal average. T_τ refers to time ordering and τ is the imaginary time variable that runs from 0 to β,where $\beta = 1/T$,T is the temperature. This problem is exactly solvable in the limit of a large number of fermions N. As shown in Appendix C, upon disorder averaging, the problem of computing the Green's function reduces to that of solving the following

set of coupled Schwinger-Dyson equations for the Green's function and self energy,

$$G\left(i\omega_n\right) = \frac{1}{i\omega_n + \mu - \Sigma(i\omega_n)} \tag{3.3}$$

$$\Sigma(\tau) = -J^2 G^2(\tau)G(-\tau) \tag{3.4}$$

$G(i\omega_n)$ is the Fourier transformed version of $G(\tau)$. These equations can also be arrived at using a diagrammatic expansion. In this approach, only a class of diagrams called melon diagrams contribute to the Green's function upon disorder averaging. See for example, [121]. In the strong coupling, infra-red limit $T \ll J$, where we can ignore $i\omega_n$ in comparison to the self energy $\Sigma(i\omega_n)$,these equations have an underlying arbitrary time reparametrization/ conformal symmetry.

3.1.1 Conformal symmetry

Equations (3.3),(3.4) can be rewritten using Fourier tranforms in the following manner:

$$\int d\tau_2 G(\tau_1, \tau_2)\Sigma(\tau_2, \tau_3) = -\delta(\tau_1 - \tau_3)$$

$$\Sigma(\tau_1, \tau_2) = -J^2 G(\tau_1, \tau_2)G(\tau_2, \tau_1) \tag{3.5}$$

where we have rewritten (3.3) in $\tau-$domain. In this form, it can be seen that these equations are invariant under a time reparametrization $\tau \to \sigma$, under which

$$\tau = f(\sigma)$$

$$G(\tau_1, \tau_2) = \left[f'(\sigma_1)f'(\sigma_2)\right]^{-1/4} G(\sigma_1, \sigma_2)$$

$$\Sigma(\tau_1, \tau_2) = \left[f'(\sigma_1)f'(\sigma_2)\right]^{-3/4} \Sigma(\sigma_1, \sigma_2) \tag{3.6}$$

where prime denotes derivative. This means that if we know the solutions to (3.5), $G(\tau_1, \tau_2)$ and $\Sigma(\tau_1, \tau_2)$ in the variable τ, we can compute the solutions to the reparametrized equations in the variable σ suing the map (3.6). As we shall see below, this allows one to deduce the finite temperature solutions if the zero temperature solutions are known. This is because in the path integral formalism, zero temperature and finite temperature are related by the domain over which the imaginary time variable τ is defined. For finite temperature, $\tau \epsilon(0, \beta)$ whereas for zero temperature, $\tau \epsilon(-\infty, \infty)$.

If we choose the map $f(\sigma)$ such that this mapping is achieved, we can compute finite temperature Green's function and Self energy from the corresponding zero temperature versions. We can map $\tau \, \epsilon \, (-\infty, \infty)$ at $T = 0$ to $\tau \, \epsilon \, (0, \beta)$ at non zero T using the map

$$\tau \to \frac{\beta}{\pi} \tan \frac{\pi\tau}{\beta}. \tag{3.7}$$

where $\beta = 1/T$ as defined before.

3.1.2   Green's function

We shall focus on the particle-hole symmetric case, $\mu = 0$. At zero temperature, these equations can be solved by a power law ansatz. To see this, we start from a retarded version of these equations $G\left(i\omega_n \to \omega + i0^+\right)$, and try a power law ansatz: $G(\omega) = Ce^{-i\frac{\pi}{4}}\omega^{-\frac{1}{2}}$, where the constant C is undetermined. An inverse Fourier transform then yields

$$G(\tau) = -\frac{C}{\sqrt{2\pi}} \frac{\text{sign}(\tau)}{|\tau|^{1/2}}. \tag{3.8}$$

Plugging this in to (3.4) gives

$$\Sigma(\tau) = -\frac{J^2 C^3}{(2\pi)^{3/2}} \frac{\text{sign}(\tau)}{|\tau|^{3/2}}. \tag{3.9}$$

Fourier transformation of $\Sigma(\tau)$, plugged in to (3.3) gives the undetermined constant $C = \frac{\pi^{1/4}}{J^{1/2}}$. Using the map (3.7), $f'(\tau) = \sec^2 \frac{\pi\tau}{\beta}$, we get from (3.8)

$$G(\tau) = -\frac{C}{\sqrt{2}} \left(\frac{T}{\sin \pi T\tau}\right)^{1/2}, \quad 0 < \tau < \beta. \tag{3.10}$$

Taking a Fourier transform gives

$$G(i\omega_n) = -\frac{(1+i)^2}{2\sqrt{2}JT\pi^{1/2}} \frac{\Gamma\left(\frac{3}{4} + n\right)}{\Gamma\left(\frac{5}{4} + n\right)} \tag{3.11}$$

Thus we see that the finite temperature Greens function splits as a $\frac{1}{\sqrt{T}}$ temperature dependence, multiplied to a scaling function which is independent of temperature. As we shall see in a later section, this temperature dependence ultimately leads to a linear in temperature dc resistivity.

3.2   SYK model from a graphene flake.
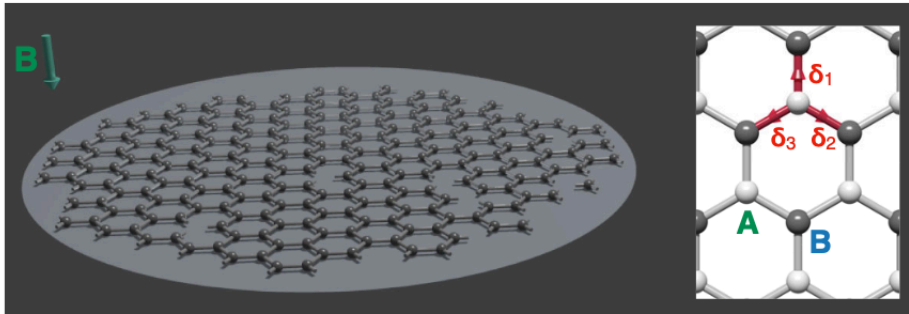
Figure 3.2: Schematic diagram of the proposed model. The inset shows graphene lattice with sublattices and nearest neighbors marked. [122]

A simple experimental realization of the SYK dot was proposed in [122]. The proposal involves a mesoscopic graphene flake with irregular boundaries subject to a strong perpendicular magnetic field. For non-interacting electrons, the magnetic field simply reorganizes the electrons into Landau levels. The essence of the proposal is that, when electrons occupy the lowest Landau level and the flake is sufficiently irregular, the Coulomb interactions projected onto to the lowest Landau level, behaves essentially like the SYK interaction. A schematic diagram of the proposal is shown in Fig. 3.2.

The Aharanov-Casher construction ensures that in the absence of interactions, the lowest Landau level remains perfectly sharp even in the presence of strong disorder if chiral symmetry of graphene is respected [123]. Since the proposed model preserves chiral symmetry of graphene [122], electrons in the lowest Landau level remain nearly perfectly degenerate and the wave functions acquire random spatial structure due to the irregular confining geometry imposed by the shape of the flake. The effective Hamiltonian for electrons in the Lowest Landau level takes the form (3.1), with

$$J_{ijkl} = \frac{1}{2} \sum_{\mathbf{r}_1, \mathbf{r}_2} \left[\Phi_i(\mathbf{r}_1)\Phi_j(\mathbf{r}_2) \right]^* V(\mathbf{r}_1 - \mathbf{r}_2) \left[\Phi_k(\mathbf{r}_1)\Phi_l(\mathbf{r}_2) \right], \qquad (3.12)$$

where $\Phi_i(\mathbf{r}_1)$ are the wave-functions in the lowest Landau level $V(\mathbf{r}_1 - \mathbf{r}_2)$ is the Coulomb interacting between electrons. $i, j, k, l = 1, \ldots, N$ where N is the number of states in the lowest Landau level. Numerically evaluated $J'_{ijkl}s$ are shown in Fig. 3.3, which show their Gaussian random nature.
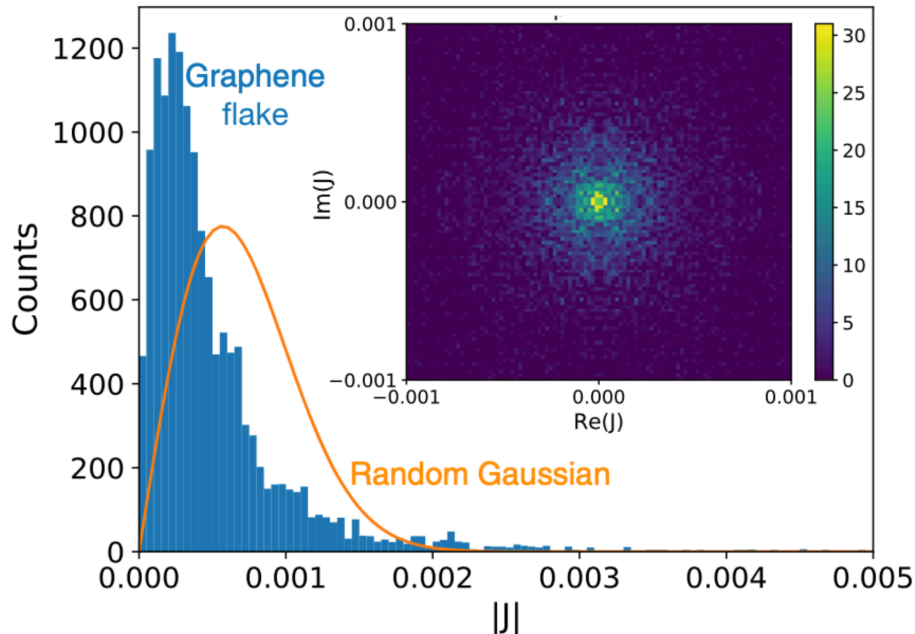
Figure 3.3: Histogram of $|J_{ijkl}|$. Inset shows the histogram of real and imaginary components of J_{ijkl}. [122]

3.3 Lattice models

Several higher dimensional extensions of the SYK dot model have appeared in the literature in the recent years [104–106, 111–113]. The primary motivation behind these models is the construction of higher dimensional Non-Fermi liquid states of matter. These models generically exhibit a crossover from a Fermi liquid phase to a non-Fermi liquid state as a function of temperature. In the limit of strong SYK coupling, incoherent metal states with linear in temperature dc resistivity [106, 111], marginal Fermi liquid states [104, 111] and other types of non Fermi liquids have been constructed [112]. Magnetotransport in these systems have also been explored [104]. As a motivation for the next chapter, in this section we review the simplest extension in the form of a hyper-cubic lattice in d-dimensions [111], where each lattice point consists of an SYK dot. Flavor preserving hopping is allowed between dots as shown in Fig. 3.4.

The Hamiltonian describing this model is given by [111]

$$\mathcal{H} = \sum_{\mathbf{r},\mathbf{r}',i} \left(-t_{\mathbf{r},\mathbf{r}'} - \mu \delta_{\mathbf{r},\mathbf{r}'} \right) c^\dagger_{\mathbf{r},i} c_{\mathbf{r}',i} + \frac{1}{(2N)^{\frac{3}{2}}} \sum_{ijkl=1}^{N} J_{ijkl} c^\dagger_{\mathbf{r}i} c^\dagger_{\mathbf{r}j} c_{\mathbf{r}k} c_{\mathbf{r}l} \tag{3.13}$$
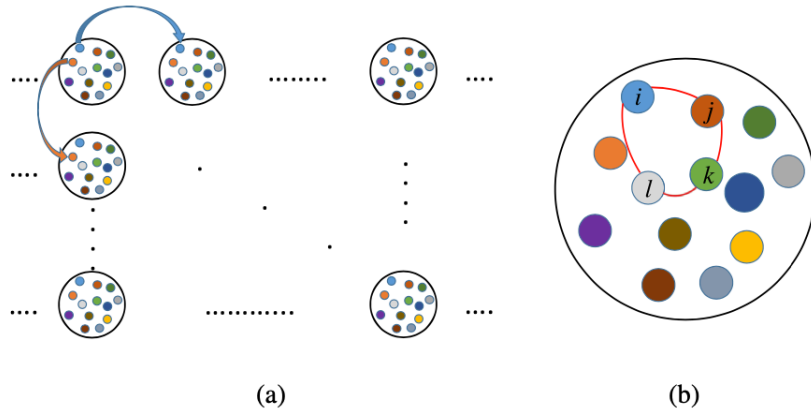
Figure 3.4: (a) A two-dimensional lattice of SYK dots. Flavor preserving hopping is shown using arrows. (b) The SYK dot that occupies each lattice point in (a). [111]

where J_{ijkl} are the usual SYK couplings, μ is the chemical potential and t refers to the hopping amplitude between sites $\mathbf{r}, \mathbf{r}'$. The full interacting problem is difficult to solve. The Green's function can be computed using the replica trick as in section 3.1. This leads to the usual set of Schwinger-Dyson equations, now also dependent on position. These are

$$
\begin{aligned}
G(i\omega, \mathbf{k}) &= \frac{1}{i\omega - \varepsilon_{\mathbf{k}} - \Sigma(i\omega, \mathbf{k})} \\
\Sigma(\tau, \mathbf{r}) &= -J^2 G(\tau, \mathbf{r})^2 G(-\tau, -\mathbf{r}).
\end{aligned}
$$

The solution to the above set of equations are qualitatively different in different temperature regimes. In the strong coupling limit, where the SYK coupling is dominant, we can perturbatively expand the Green's function around the SYK dot Green's function, including the effects of hopping perturbatively. In this regime, if we begin with an ansatz for the self energy, $\Sigma(i\omega, \mathbf{k}) = \Sigma_{syk}(i\omega, \mathbf{k}) + \Sigma^{(1)}(i\omega, \mathbf{k})$, where $\Sigma_{syk}(i\omega, \mathbf{k})$ is the SYK self energy and $\Sigma^{(1)}(i\omega, \mathbf{k})$ is the correction due to hopping, we can express the Green's function as

$$
\begin{aligned}
G(i\omega, \mathbf{k}) &= \frac{1}{i\omega - \varepsilon_{\mathbf{k}} - \Sigma(i\omega, \mathbf{k})} \\
&\approx -\frac{1}{\Sigma_{syk}(i\omega)} + \frac{\varepsilon_{\mathbf{k}}}{\Sigma_{syk}(i\omega, \mathbf{k})^2} + .. \\
&\equiv G_{syk}(i\omega) + G^{(1)}(i\omega, \mathbf{k}).
\end{aligned}
\tag{3.14}
$$

Using the SYK Green's function from section 3.1, we see that the leading temperature depen-

dence of $G(i\omega_n, \mathbf{k}) \sim \frac{1}{\sqrt{T}}$. Since this Green's function has no pole structure, there are no quasi-particles. This Green's function thus describes an incoherent metal state. Considering dispersion as a small in comparison to the self energy, $\varepsilon_\mathbf{k} \ll \Sigma_{syk}(i\omega)$, implies a temperature regime $T \gg \frac{t^2}{J}$ since the SYK self energy goes like $\sqrt{JT}$. This behavior crosses over to a Fermi liquid like Green's function at low temperature or frequency. Starting from a Fermi liquid like ansatz for the Green's function, a self consistent calculation [111] for the Green's function for $T \ll \frac{t^2}{J}$ shows that the Green's function behaves like that of a renormalized Fermi liquid. Thus the lattice SYK model has a crossover temperature, $T_c = \frac{t^2}{J}$ above which the model behaves as an incoherent metal and below which the model behaves as a Fermi liquid. We can also understand this from a scaling point of view [106, 111]. When the hopping parameter $t = 0$, we have a set of decoupled SYK dots. Considering hopping as a perturbation, we can look at the renormalization group scaling dimensions of the hopping parameter. Under a scaling $\tau \to \tau' = \tau/s$, $t \to t' = s^{1/2}t$, implying that hopping is a relevant perturbation and will grow under renormalization. If we run the scaling until $s_T = J/T$,the renormalized hopping at this scale would be $t_T = t\,(J/T)^{1/2}$. With decreasing temperature, the regime of weak hopping applies only until $t \sim J$. This corresponds to temperature $T^* = t^2/J$. For temperatures above T^*, the description of weakly coupled SYK dots apply and we have an incoherent system, whereas for temperatures below this scale one could expect the coupling between dots to lead to a Fermi liquid like behavior.

The incoherent metal phase is particularly interesting because the dc resistivity in this phase is linearly proportional to temperature, a property that is characteristic of the strange metal phase of high-T_c superconductors[111]. The dc conductivity is given by

$$\sigma_{\mathrm{dc}} = \lim_{\omega \to 0} \frac{\mathrm{Im}\mathcal{K}(i\omega_n \to \omega + i0^+)}{\omega}, \tag{3.15}$$

where $\mathcal{K}^{\mathrm{ret}}(\omega)$ is the retarded current-current correlation function, $\mathcal{K}$ is given by the series of diagrams in Fig. 4.5. The current operator is $\mathbf{J} = e\sum_{\mathbf{k}i} v_\mathbf{k} c_{\mathbf{k}i}^\dagger c_{\mathbf{k}i}$ where $v_\mathbf{k} = \nabla_\mathbf{k}\varepsilon_\mathbf{k}$. The leading contribution comes from the first diagram giving,

$$\sigma_{dc} = Ne^2\beta \int \mathrm{d}\omega \int \mathrm{d}^2 k v_\mathbf{k}^2 \mathcal{A}\,(\mathbf{k},\omega)^2\,\frac{1}{4\cosh^2\left(\frac{\beta\omega}{2}\right)} \tag{3.16}$$

where $\mathcal{A}\left(\mathbf{k}, \omega\right) = -2\mathrm{Im}G\left(\mathbf{k}, i\omega_n \to \omega + i0^+\right).$ Using the leading contribution to the Green's functions from (3.14), we get

$$\sigma_{dc} = Ne^2 \beta \int d\omega \int d^2 k v_{\mathbf{k}}^2 \left(\frac{1}{\sqrt{JT}}\right)^2 \frac{1}{4\cosh^2\left(\frac{\beta\omega}{2}\right)} \propto \frac{1}{T}. \qquad (3.17)$$

Therefore we see that an otherwise metallic lattice model with a Fermi surface behaves qualitatively differently as a function of temperature in the presence of SYK interactions. There is a low temperature Fermi liquid phase which crosses over to a high temperature incoherent metal with a linear in temperature resistivity. This motivates the question of what happens if we have a semi-metallic model in the non interacting limit coupled to SYK interactions. The next chapter investigates this question using a simple one dimensional model.

Chapter 4

Incoherent Semimetals

4.1 Introduction

Motivated by the SYK models discussed in the previous chapter, we ask what is the nature of the normal state in a disordered semimetal with random local couplings. To this end, we study a 1D ladder model with local random couplings at every unit cell, as shown in Fig. 1. The hopping amplitudes between lattice sites is finely tuned such that this system describes a half-filled semimetal with quadratic dispersion and local SYK couplings. The weakly dispersive limit $t^2/J \ll T \ll J$ has approximate conformal invariance and recovers the usual SYK transport behavior, as expected. In the strongly dispersive regime, $T \ll t^2/J$, the scaling symmetry of the problem becomes transparent, albeit the absence of conformal symmetry. In this limit, the incoherent regime extends down to zero frequency and temperature, unlike in the more conventional metallic case. We show that the resistivity of this model has a sub-linear scaling with temperature,

$$\rho \propto T^{2/5}, \tag{4.1}$$

whereas the Lorentz ratio $L = \kappa/(\sigma T) \approx 3.2$ is fairly close to the value expected for a Fermi liquid, $L = \pi^2/3$. We find through a scaling argument that when the system starts from the SYK fixed point at high temperature, it flows towards a distinct non-Fermi liquid (NFL) fixed point at zero temperature. At intermediate energy scales, away from the low temperature fixed point, the system crosses over from a "Planckian" semimetal to an incoherent NFL with sub-linear temperature scaling
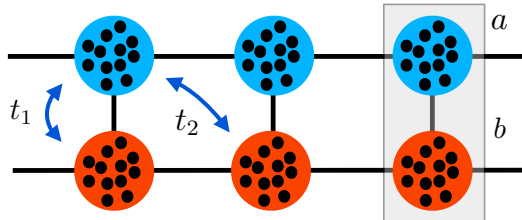
Figure 4.1: Dispersive SYK ladder model: The unit cell contains two sites, one for each chain (color). Each color site hosts N complex fermions, which interact locally through random couplings. We assume that hopping is only allowed between different color sites, with t_1 the NN hopping and t_2 the NNN one. The two-band quadratic dispersion in Eq. (4.3) can be obtained by tuning $t_1 = -2t_2 = t$, with $m = 2/(ta^2)$ the effective mass of the fermions, where a is the lattice constant.

of the resistivity.

This paper is organized in the following way: in section II we introduce the lattice model of a 1D ladder of SYK quantum dots that behaves as a 1D semimetal with quadratic dispersion. In section III we address the Green's function of this system at zero and finite temperature. In the strongly dispersive regime $(T \ll t^2/J)$, where conformal symmetry is not present, we numerically extract the finite temperature scaling functions of the Green's function and of the self-energy. In section IV, we discuss a scaling analysis of the problem and the crossover between the high temperature incoherent Planckian regime and the low temperature NFL one. In section V we address the temperature scaling of the dc resistivity of the model. Finally, in section VI we present our conclusions.

4.2 Model

We consider $N-$flavors of complex fermions hopping on an 1D lattice. Each lattice site hosts an SYK dot with random, site dependent interactions $J^x_{ijk\ell}$ between them. The indexes $i, j, k, \ell = 1, .., N$ label the $N-$flavors/colors per site. We start from a 1D ladder shown in Fig. 1, with two sites per unit cell, shown in blue and red. Allowing hopping processes between blue and red sites only, the Hamiltonian of the kinetic term can be written as

$$\hat{\mathcal{H}}_0 = \int_k \sum_\nu f(k) \psi^\dagger_{k,i,\nu} (\sigma_x)_{\nu,\nu'} \psi_{k,i,\nu'}, \tag{4.2}$$

where

$$f(k) = t_1 + 2t_2 \cos(ka), \tag{4.3}$$
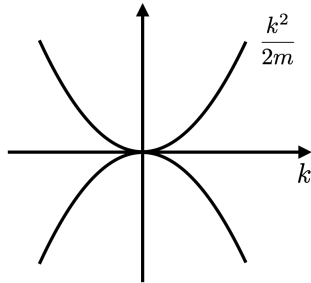
Figure 4.2: Finely tuned energy dispersion for the ladder model illustrated in Fig. 1. The half-filled band describes a 1D semimetal with parabolic band touching at $k = 0$.

with t_1 and t_2 the hopping between nearest neighbors (NN) and second nearest neighbors (NNN) respectively among different color sites, and $\int_k \equiv a(2\pi)^{-1} \int_{-\Lambda}^{\Lambda} \mathrm{d}k$ with $\Lambda = \pi/a$ the ultraviolet cutoff. $\psi_{i,\nu}$ is a two-component spinor in the site basis of the unit cell $\nu = a, b$ and σ_x is the real off-diagonal Pauli matrix in that basis. Fine tuning the hopping constants to $t_1 = -2t_2 = t$, then

$$\mathcal{H}_0 = \int_k \sum_{i\nu} \frac{k^2}{2m} \psi^{\dagger}_{k,i,\nu} \, (\sigma_x)_{\nu\nu'} \, \psi_{k,i,\nu'}, \tag{4.4}$$

in the continuum limit ($k \ll 1/a$), with $m^{-1} = ta^2/2$. The dispersion of this model has two quadratic bands touching at a single point $k = 0$, as shown in Fig. 2. At half filling, the band lacks a Fermi momentum and behaves as a 1D semimetal. In the following, we assume the band to be half filled and set $a \to 1$.

These fermions interact via a local, instantaneous two body SYK interaction,

$$\mathcal{H}_{\mathrm{SYK}} = \frac{1}{(N)^{\frac{3}{2}}} \sum_{\nu\nu',ijk\ell} \int_x J^x_{ijk\ell} \psi^{\dagger}_{x,i,\nu} \psi^{\dagger}_{x,j,\nu'} \psi_{x,k,\nu'} \psi_{x,\ell,\nu} \tag{4.5}$$

with random, color site independent matrix elements $J^x_{ijk\ell}$ that are properly antisymmetrized with $J^x_{ijk\ell} = -J^x_{jik\ell} = -J^x_{ij\ell k}$. As in the other SYK models, we take these to be complex Gaussian distributed coupling with a zero mean value $\langle\langle J^x_{ijk\ell} \rangle\rangle = 0$ and variance $\langle\langle |J^x_{ijk\ell}|^2 \rangle\rangle = J^2/16$.

The standard method to study the current problem is the imaginary time path integral formalism, where the partition function is given by $\mathcal{Z} = \int \left[\mathcal{D}\bar\psi \mathcal{D}\psi \right] \mathrm{e}^{-\mathcal{S}}$, where $\mathcal{S} = \mathcal{S}_0 + \mathcal{S}_{\mathrm{SYK}}$, with

$$\mathcal{S}_0 = \int_{\tau,x} \sum_{\ell,\nu} \bar\psi_{\ell,\nu}(\tau, x) \left[\partial_\tau - (\sigma_x)_{\nu\nu'} \frac{\partial_x^2}{2m} \right] \psi_{\ell,\nu'}(\tau, x). \tag{4.6}$$

We define $\int_\tau \equiv \int_0^\beta d\tau$, with $\beta = 1/T$, and $\mathcal{S}_{\text{SYK}}$ the corresponding two body action of (4.5) with with same time Grassmann fields $\bar{\psi}(\tau, x)$ and $\psi(\tau, x)$. In order to deal with the disorder, we use the replica trick and average over disorder realizations. This procedure amounts to an annealed approximation[107]. Using

$$\langle\langle e^{-\sum_{ijk\ell} J_{ijk\ell} A_{ijk\ell}}\rangle\rangle = e^{2J^2 \sum_{ijk\ell} \bar{A}_{ijk\ell} A_{ijk\ell}} \tag{4.7}$$

and defining the Green's function

$$\hat{G}_{\nu\nu'}(\tau, x) = -\frac{1}{N} \sum_{\ell=1}^N \langle T[\psi_{\nu,\ell}(0,0)\, \bar{\psi}_{\nu',\ell}(x,\tau)]\rangle, \tag{4.8}$$

the integration over the fermionic fields results in the saddle point action,

$$\mathcal{S}_{\text{eff}} = -\log\det\left[\delta\left(\tau - \tau'\right)\delta\left(x - x'\right)\left(\partial_\tau + \sigma_x\left(i\partial_x\right)^2\right) + \hat{\Sigma}\left(x - x', \tau - \tau'\right)\right]$$
$$-\frac{J^2}{8}\int_{\tau,\tau'} \text{tr}\hat{G}^2\left(0, \tau - \tau'\right)\text{tr}\hat{G}^2\left(0, \tau' - \tau\right) - \int_{x,x'}\int_{\tau,\tau'}\text{tr}\left[\hat{\Sigma}\left(x - x', \tau - \tau'\right)\hat{G}\left(x' - x, \tau' - \tau\right)\right], \tag{4.9}$$

where $\hat{\Sigma}(x - x', \tau - \tau')$ is the self-energy. The action can be minimized exactly in $\hat{G}$ and $\hat{\Sigma}$ in the large-N limit. Following the minimization, the solutions form a set of Schwinger-Dyson equations

$$\hat{G}^{-1}(i\omega_n, k) = i\omega_n - \frac{k^2}{2m}\sigma_x - \hat{\Sigma}(i\omega_n, k), \tag{4.10}$$

and

$$\hat{\Sigma}(\tau, x) = -\frac{J^2}{2}\delta(x)\hat{G}(-\tau, 0)\,\text{tr}\left[\hat{G}(\tau, 0)\,\hat{G}(\tau, 0)\right], \tag{4.11}$$

The self-energy $\hat{\Sigma}(i\omega_n, k) \equiv \hat{\Sigma}(i\omega_n)$ is therefore momentum independent, reflecting the x−dependence of the couplings $J_{ijk\ell}^x$. The disorder averaged SYK term is uncorrelated and purely local. We denote the Fourier transform of the momentum independent self-energy as $\hat{\Sigma}(\tau)$. We also denote

$$\hat{\mathcal{G}}(\tau) \equiv \hat{G}(\tau, 0) = \int_k \hat{G}(\tau, k) \tag{4.12}$$
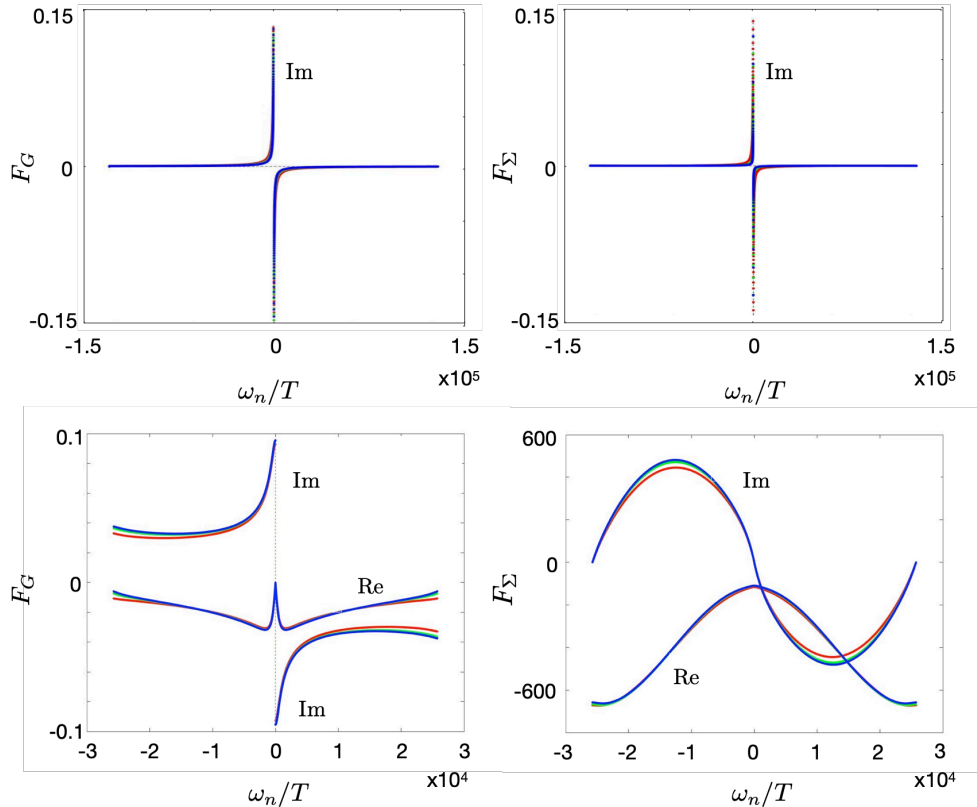
Figure 4.3: Scaling functions for the Green's function (F_G) and the self-energy (F_Σ) versus Matsubara frequency ω_n normalized by temperature T. Top row: numerical solution of Eq. (4.14) and (4.16) for F_G and F_Σ in the SYK limit for various temperatures, namely $T = 10, 20$ and 30 (green line, blue and red, respectively). $\beta = T^{-1}$ and $J = 100$ are set in units of $2m$ with $a \to 1$ ($\Lambda = \pi$). In this case, the Green's function and self energy are purely imaginary and admit an analytical solution [see Eq. (4.17)]. Bottom row: numerical solution of Eqs. (14) and (25), in the strongly dispersive regime. The real and imaginary parts of the scaling functions were computed at various temperatures, namely $\beta = 1/T = 256, 64$ and 4 (green line, blue and red, respectively). All curves nearly coincide at low frequencies, where the scaling functions are expected to be temperature independent.

for the momentum integrated Green's function.

4.3 Green's Function

If one takes the ansatz for the Green's function, $\hat{G}(\tau) = \mathcal{G}(\tau)\sigma_x$, the self energy then has to be of the form $\hat{\Sigma}(\tau) = \Sigma(\tau)\sigma_x$. As in usual SYK models, we make the usual infrared assumption to

ignore $i\omega_n$. The Schwinger Dyson equations (4.10) and (4.11) can be written as

$$
\begin{aligned}
\mathcal{G}(i\omega_n) &= -\int_k \frac{1}{\frac{k^2}{2m} + \Sigma(i\omega_n)} \\
&= -\frac{\sqrt{2m}}{\pi\sqrt{\Sigma(i\omega)}} \tan^{-1}\left(\frac{\Lambda}{\sqrt{2m}\sqrt{\Sigma(i\omega)}}\right),
\end{aligned}
\tag{4.13}
$$

and

$$
\Sigma(\tau) = -J^2 \mathcal{G}^2(\tau)\mathcal{G}(-\tau),
\tag{4.14}
$$

There are two limits of particular interest. As it will be clear in the next section, one is the intermediate frequency limit $t^2/J \ll \omega \ll J$, where the magnitude of the argument of the $\tan^{-1}(y)$ function,

$$
y \equiv \frac{\Lambda}{\sqrt{2m}\sqrt{\Sigma(i\omega)}}
\tag{4.15}
$$

is small. This regime corresponds to the weakly dispersive limit, which recovers the physics of the $0 + 1$ dimensional SYK dot. The other is the strongly dispersive regime, $\omega \ll t^2/J$, where the magnitude of $y \gg 1$. We show that this limit is exactly solvable and leads to a different NFL regime.

4.3.1 Weakly dispersive limit

In this weakly dispersive limit, the SYK physics dominates and typically one obtains a fully incoherent system with a linear in T dc resistivity. In that regime, Eq. (4.13) becomes

$$
\mathcal{G}(i\omega_n) \approx -\frac{1}{\pi}\frac{\Lambda}{\Sigma(i\omega_n)}.
\tag{4.16}
$$

The Schwinger-Dyson Eq. (4.14) and (4.16) have the same form as in the SYK dot model [85]. They have conformal/reparametrization invariance, indicating a power law solution at $T = 0$.

At zero temperature, Eq. (4.14) and (4.16) can be solved by the ansatz $\mathcal{G}(i\omega) = c_1 e^{-i\frac{\pi}{4}}(i\omega)^{-\frac{1}{2}}$ for the time ordered Green's function [85]. Using this result in Eq. (4.14) and taking a Fourier transform one finds

$$
\Sigma(i\omega) = -\frac{J^2 c_1^3}{\pi} e^{i\frac{\pi}{4}}\sqrt{i\omega},
\tag{4.17}
$$

where the constant $c_1 = \Lambda^{\frac{1}{4}}/\sqrt{J}$. The zero temperature dispersive Green's function is

$$\hat{G}(i\omega, k) = \left(\frac{-1}{\Sigma\left(i\omega\right)} + \frac{k^2/2m}{\Sigma\left(i\omega\right)^2} + \dots \right) \sigma_x \tag{4.18}$$

This solution introduces a perturbative correction to the SYK Green's function, in the same spirit as in the metallic case [111].

To get the finite temperature solutions, one can then use the conformal map, $\tau \to f\left(\tau\right) = \tan \frac{\pi\tau}{\beta}$. Applying this to the Fourier transform of $\mathcal{G}\left(i\omega\right)$ gives

$$\mathcal{G}\left(\tau\right) = \text{sgn}(\tau)\, c_1 \sqrt{\frac{1/\beta}{2\sin \pi\tau/\beta}}. \tag{4.19}$$

The finite temperature self-energy $\Sigma\left(i\omega_n\right)$ can then be obtained from a Fourier transform of (4.14),

$$\Sigma\left(i\omega_n\right) = iJ^2 c_1^3 \frac{(2\pi)^{3/2} \sqrt{2}\Gamma\left(\frac{3}{4} + \frac{\omega_n\beta}{2\pi}\right)\Gamma\left(-\frac{1}{2}\right)}{\sqrt{\beta}\pi\Gamma\left(\frac{1}{4} + \frac{\omega_n\beta}{2\pi}\right)}, \tag{4.20}$$

with ω_n a Matsubara frequency. The dispersive Green's function at finite temperature follows from Eq. (4.16) and (4.20),

$$\hat{G}(i\omega_n, k) = \left(\frac{-1}{\Sigma\left(i\omega_n\right)} + \frac{k^2/2m}{\Sigma^2\left(i\omega_n\right)} + \dots \right) \sigma_x \tag{4.21}$$

It is well known that the Greens function and self energies in this regime have some convenient scaling properties. Eqs. (4.14) and (4.16) admit solutions of the form:

$$\mathcal{G}(i\omega_n) = (JT)^{-\frac{1}{2}}\Lambda^{-\frac{3}{4}}F_G\left(\frac{\omega_n}{T}\right) \tag{4.22}$$

$$\Sigma(i\omega_n) = (JT)^{\frac{1}{2}}\Lambda^{\frac{3}{4}}F_\Sigma\left(\frac{\omega_n}{T}\right) \tag{4.23}$$

where $F_{G,\Sigma}$ are scaling functions which are independent of all parameters. The scaling functions are plotted in the top row panels of Fig. 3. They were obtained by numerically solving Eq. (4.14) and (4.16) for various temperatures and then stripping away the power law dependence in T and J from the above equations. The results show good agreement with the scaling arguments.

4.3.2 Strongly dispersive regime

Next we consider the strongly dispersive regime. As we will show below, this inequality corresponds to the regime where

$$\omega \ll \frac{t^2}{J}, \tag{4.24}$$

and leads a different kind of NFL behavior compared to weakly dispersive SYK models.

In the strongly dispersive regime, the Schwinger-Dyson equation (4.13) reads

$$\mathcal{G}(i\omega) = -\frac{1}{2}\frac{\sqrt{2m}}{\sqrt{\Sigma(i\omega)}}. \tag{4.25}$$

Eq. (4.14) and (4.25) admit a power law solution at $T = 0$, given by the ansatz

$$\mathcal{G}(\tau) = C\frac{1}{|\tau|^{2\Delta}}, \tag{4.26}$$

where $2\Delta = 3/5$, as found in a related model [112], with

$$C = \left[\frac{\Gamma(\frac{1}{5})^{-1}\Gamma(\frac{2}{5})^{-2}}{20\sin^2\left(\frac{3\pi}{10}\right)\sin\left(\frac{9\pi}{10}\right)}\right]^{\frac{1}{5}} \approx 0.40. \tag{4.27}$$

That solution corresponds to a self-energy

$$\Sigma(i\omega) = C'J^{\frac{4}{5}}m^{\frac{3}{5}}|\omega|^{6\Delta-1} \gg |\omega|, \tag{4.28}$$

from equation (4.14). Explicit verification of this solution follows by Fourier transforming (25),

$$\mathcal{G}(i\omega) = 2C\sin\pi\Delta\,\Gamma(1-2\Delta)J^{-\frac{2}{5}}m^{\frac{1}{5}}|\omega|^{2\Delta-1}, \tag{4.29}$$

and calculating $\Sigma(i\omega)$ from (4.14). The zero-temperature Green's function is hence

$$\hat{G}(i\omega, k) = \frac{-\sigma_x}{\frac{k^2}{2m} + C'J^{\frac{4}{5}}m^{\frac{3}{5}}|\omega|^{4/5}}, \tag{4.30}$$

where

$$C' = -2C^3\sin\left(\frac{9\pi}{10}\right)\Gamma\left(-\frac{4}{5}\right) \approx 0.22. \tag{4.31}$$

The Green's function above describes a distinct type of incoherent semimetal, and is valid all the way down to zero frequency. It contrasts with the result in the coherent $J \to 0$ limit of the ladder problem model $(J/|\omega| \ll 1)$, where the Green's function has a pole with well defined quasiparticles. One needs to analytically continue the above solution and impose physical restrictions to obtain the exact Green's function.

Note that the linear in T resistivity in SYK models stems from $\Delta = \frac{1}{4}$. In strongly dispersive semimetals, with the magnitude of $y \gg 1$, finite temperature solutions cannot be obtained using a conformal map on the $T = 0$ solution because (4.14) and (4.25) do not have the requisite conformal/reparametrization symmetry. Finite temperature solutions to these equations then have to be obtained numerically. However, we still have a scaling symmetry which dictates a certain scaling form for the solutions.

Rewriting (4.25) in $\tau-$space,

$$\int_{\tau_1, \tau_2} \mathcal{G}(\tau)\mathcal{G}(\tau - \tau_2)\Sigma(\tau - \tau_1) = \frac{m}{2}\delta(\tau). \tag{4.32}$$

It is easy to see that these equations are invariant under

$$\tau \to b\tau, \quad \mathcal{G} \to b^{-\frac{3}{5}}\mathcal{G}, \quad \Sigma \to b^{-\frac{9}{5}}\Sigma. \tag{4.33}$$

Under this scaling, $T \to T/b$ leaving $T\tau$ invariant. With this information, one can see that (4.14) and (4.25) admit a solution of the form

$$\mathcal{G}(\tau) = m^{\frac{1}{5}}J^{-\frac{2}{5}}T^{\frac{3}{5}}\tilde{\mathcal{G}}(T\tau) \tag{4.34}$$

and

$$\Sigma(\tau) = m^{\frac{3}{5}}J^{\frac{4}{5}}T^{\frac{9}{5}}\tilde{\Sigma}(T\tau). \tag{4.35}$$

Equivalently in Fourier space, we find

$$\mathcal{G}(i\omega_n) = m^{\frac{1}{5}}(JT)^{-\frac{2}{5}}F_G\left(\frac{\omega_n}{T}\right) \tag{4.36}$$

$$\Sigma(i\omega_n) = m^{\frac{3}{5}}(JT)^{\frac{4}{5}}F_\Sigma\left(\frac{\omega_n}{T}\right) \tag{4.37}$$

where $F_{G,\Sigma}$ are scaling functions that are independent of temperature T and the coupling J, with ω_n a Matsubara frequency. The dispersive finite temperature Green's function of the problem in this regime is

$$\hat{G}^{-1}(i\omega_n, k) = - \left(\frac{k^2}{2m} + m^{\frac{3}{5}}(JT)^{\frac{4}{5}} F_\Sigma(\omega_n/T) \right) \sigma_x. \tag{4.38}$$

As shown in the next section, this will suffice to determine the temperature dependence of various transport coefficients. Strictly speaking, the scaling symmetry is only present in the infrared limit of the theory. This means that the exact numerical solutions may violate these scaling forms at very high frequencies. The real and imaginary parts of the numerically obtained scaling functions F_G and F_Σ are plotted in the bottom row of Fig. 3. The plots show good agreement with Eq. (4.37) even outside the infrared limit.

4.4 Scaling analysis

After averaging over the disorder, which is spatially uncorrelated, the SYK term in the action has eight fermionic fields, which we symbolically write as

$$\mathcal{S}_{\text{SYK}} = J^2 \int_{\tau_1, \tau_2, x} [\bar{\psi}(\tau_1, x)\psi(\tau_1, x)]^2 [\bar{\psi}(\tau_2, x)\psi(\tau_2, x)]^2. \tag{4.39}$$

Rescaling time as $\tau' = \tau/s$ and imposing the SYK coupling J to be marginal, then the fields rescale as $\psi' = \psi/s^{\frac{1}{4}}$. As pointed out before [106, 111], analyzing the problem in the vicinity of the fixed point of the $0+1$ dimensional SYK model $(t = 0)$, the kinetic term is a relevant perturbation and the hopping parameter grows as $t' = t\sqrt{s}$. If one starts from temperature T in the weakly dispersive regime $t \ll J$, the hopping will grow until $t'(s_*) \sim J$ for a rescaling parameter no larger than $s_* = J/T$. Hence, the scaling stops at $T = t^2/J$. The validity of the incoherent "Planckian" regime requires that

$$T \gg T_* = t^2/J, \tag{4.40}$$

as in the case of incoherent metals with a finite Fermi surface [111].

If one continues to lower the temperature further below T_*, we claim that the system crosses over to a different type of incoherent NFL regime with sub-linear temperature scaling of the resistivity,
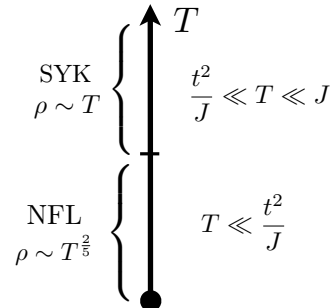
Figure 4.4: Different temperature regimes in the scaling. At temperature $T > T_* = t^2/J$, the system is close to the $0+1$ dimensional SYK fixed point and shows Planckian behavior, with linear dependence of the resistivity in temperature. Below $T_* = t^2/J$ the system crosses over towards a distinct type of incoherent NFL, with $\rho \sim T^{\frac{2}{5}}$.

as illustrated in Fig. 4. From the perspective of the Schwinger-Dyson equations (4.13) and (4.14), the parameter that controls the crossover between the weakly and the strongly dispersive regimes is

$$y(T) \sim \sqrt{\left|\frac{t}{\Sigma(T)}\right|}. \tag{4.41}$$

In the strongly dispersive regime $y(T) \gg 1$, setting $m \sim t^{-1}$, one can write the solution of the finite temperature self-energy (4.37) as

$$|\Sigma(T)| \propto t^{-\frac{3}{5}}(JT)^{\frac{4}{5}} \ll t. \tag{4.42}$$

This inequality leads to $T \ll T_* = t^2/J$. In the same way, in the weakly dispersive regime ($y(T) \ll 1$),

$$|\Sigma(T)| \propto \sqrt{JT} \gg t, \tag{4.43}$$

as seen from Eq. (4.20), implying that $T \gg T_*$.

We note that in the case of metals, the $T < T^*$ regime was found to realize a Fermi liquid. In the case of a 1D half-filled semimetal with parabolic touching, we showed that the low temperature regime does not lead to a semimetal, but to another type of incoherent NFL, whose transport properties will be addressed in the next section.

4.5 Transport

In this section, we look at the electric and thermal conductivities using the above finite temperature solutions. These can be computed using the Kubo formula. The charge current operator for this model is

$$\hat{j}_e = \frac{e}{2m} \int_k \sum_i k \psi_{ki}^\dagger \sigma_x \psi_{ki}. \tag{4.44}$$

The zero frequency conductivity is given by

$$\sigma_{\text{dc}} = \lim_{\omega \to 0} \frac{\text{Im} \mathcal{K}^{\text{ret}}(\omega)}{\omega}, \tag{4.45}$$

where $\mathcal{K}^{\text{ret}}(\omega)$ is the retarded current-current correlation function, $\mathcal{K}(\tau) = \langle T[\hat{j}_e(0,x)\hat{j}_e(\tau,x)]\rangle$, given by the series of diagrams in Fig. 5. Each diagram displayed in that figure is of order N. For instance, in diagram (b) each SYK vertex contributes a factor of $N^{-\frac{3}{2}}$, while the three independent flavor sums contribute N^4, making it a total of order N. Diagrams in (b) and (c) vanish because the current vertex is an odd function of momenta. This can be readily seen by noticing that because of the disorder averaging, the summation over momenta through each current vertex can be performed independently, resulting in a zero contribution of those diagrams [116]. The remaining diagram is shown in Fig. 5a. It can be written in terms of the Green's functions derived before as

$$\mathcal{K}(i\omega_n) = \frac{Ne^2}{(2m)^2} T \text{ tr} \sum_{\nu_n} \int_k k^2 \hat{G}(i\nu_n, k) \hat{G}(i\nu_n + i\omega_n, k). \tag{4.46}$$

The transport properties of the weakly dispersive regime recovers the expected behavior of incoherent metals found in Ref. [104, 111], $\sigma_{\text{dc}} \propto 1/T$, and we will focus instead in the strongly dispersive case.

It is usually challenging to sum over Matsubara frequencies in the absence of poles in the Green's functions. One can circumvent that difficulty by using the spectral representation of the Green's function

$$\hat{G}(i\omega_n, k) = \int_{\omega'} \frac{\hat{\mathcal{A}}(k, \omega')}{i\omega_n - \omega'}, \tag{4.47}$$

with

$$\hat{\mathcal{A}}(k, \omega) = \frac{1}{\pi} \sigma_x \text{Im} \frac{1}{\frac{k^2}{2m} + \Sigma(\omega + i0_+)} \tag{4.48}$$
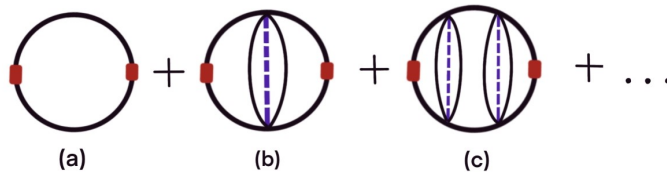
Figure 4.5: Diagrams that contribute to the current-current correlation function to leading order in N (see text). Red rectangles represent the current vertex. Black lines represent the fermion Green's function and dotted blue line represents disorder average. Since the current vertex is an odd function of momenta, diagrams (b) and (c) and so on vanish, leaving (a) as the sole contribution in the large-N limit.

the spectral function. One arrives at

$$\sigma_{dc} = \frac{Ne^2\sqrt{2m}}{\pi^2 T} \int_\omega \frac{\left[\text{Im}\Sigma(\frac{\omega}{T})\right]^2}{\cosh^2(\frac{\omega}{2T})} \int_k \frac{k^2}{\left|\frac{k^2}{2m} + \Sigma\left(\frac{\omega}{2T}\right)\right|^4}. \tag{4.49}$$

Equivalently, casting Eq. (4.49) in terms of the scaling functions (4.37), the dc conductivity is

$$\sigma_{\text{dc}}(T) = \frac{Ne^2}{\sqrt{2m}(JT)^{\frac{2}{5}}} I_1, \tag{4.50}$$

where

$$I_1 = \frac{1}{\pi^2} \int_0^\infty dz \frac{[\text{Im}F_\Sigma(z)]^2}{\cosh^2(\frac{z}{2})} \int_0^\infty dy \frac{y^2}{|y^2 + F_\Sigma(z)|^4} \tag{4.51}$$

is a dimensionless integral, and $F_\Sigma(z)$ the analytically continued scaling function of the self energy.

A signature property of Fermi liquids is captured by the Lorentz ratio, $L = \kappa/(\sigma T)$, which is the ratio of thermal (κ) and electric (σ) conductivities. In the particle-hole symmetric model, the thermoelectric contribution to the thermal conductivity, which is proportional to T/σ, vanishes by symmetry and can be ignored in the computation of κ [104, 114]. The energy current, whose correlation function determines the remaining piece of the thermal conductivity, is given by

$$\hat{j}_E = \int_k \sum_i \frac{k}{2m} \psi_{k,i}^\dagger \sigma_x \partial_\tau \psi_{k,i}. \tag{4.52}$$

In the present particle-hole symmetric case, the thermal conductivity is then given by the same diagrams as in the case of σ. Following the same prescription as above,

$$\kappa = \lim_{\omega \to 0} \frac{\mathcal{K}_E^{\text{ret}}(\omega)}{\omega T}, \tag{4.53}$$

64

where $\mathcal{K}_E(\tau) = \langle T[\hat{j}_E(0, x)\hat{j}_E(\tau, x)]\rangle$ is a thermal current-current correlation function. This leads to

$$\kappa = \frac{Ne^2}{\sqrt{2m}J^{\frac{2}{5}}}T^{\frac{3}{5}}I_2, \tag{4.54}$$

where

$$I_2 = \frac{1}{\pi^2}\int_0^\infty \mathrm{d}z\, z^2 \frac{\mathrm{Im}\left[F_\Sigma(z)\right]^2}{\cosh^2(\frac{z}{2})}\int_0^\infty \mathrm{d}y\, \frac{y^2}{|y^2 + F_\Sigma(z)|^4}. \tag{4.55}$$

In order to calculate integrals I_1 and I_2, one needs to perform a numerical analytical continuation of the scaling functions obtained in section III. In the spirit of SYK models, we compute these integrals assuming the scaling form to be valid over the entire range of frequencies. Numerical analytical continuation is a challenging problem. The numerical integrals were done with the Pade approximation method in the TRIQS library [117, 118].

We numerically find that slight variations in the Matsubara scaling forms can significantly affect the integrals I_1 and I_2, but their ratio is insensitive to numerical issues with the analytical continuation process in the regime of interest. The Lorentz ratio is

$$L = \frac{\kappa}{T\sigma} = \frac{I_2}{I_1} \approx 3.2, \tag{4.56}$$

which is rather close to the Fermi liquid value of $L_{FL} = \pi^2/3$.

4.6 Discussion

In this work, we studied a simple semi-metallic version of a dispersive SYK model in one dimension. Contrary to most studies of dispersive models in the literature [104–106, 111, 112], we focus on the strongly dispersive limit, which corresponds to the stable fixed point of this problem from the scaling point of view. In this limit, we find that the Schwinger-Dyson equations do not admit an exact analytic finite temperature solution even in the infrared approximation, where it is assumed that $\Sigma(i\omega) \gg i\omega$. In particular, the model does not exhibit conformal symmetry, which makes it difficult to solve the Schwinger-Dyson equations analytically. We solve those equations *exactly* exploiting the scaling symmetry of the model, combined with numerical calculations. We find that the Greens function and self-energy scale with temperature with a power law of $T^{-\frac{2}{5}}$ and $T^{\frac{4}{5}}$ respectively.

Using this solution to study transport properties, we show that dc resistivity scales with a sublinear power law dependence on temperature, $\rho \sim T^{\frac{2}{5}}$. We compute the Lorentz ratio $L = \kappa/(\sigma T)$ with the analytically continued scaling functions and find that $L \approx 3.2$, rather close to that of Fermi liquids. The scaling analysis of this problem indicates that if one starts in the high temperature SYK fixed point of the problem, where $t^2/J \ll T \ll J$, the hopping parameter will grow as one scales the temperature down, while the SYK coupling is marginal. The scaling flows towards the strongly dispersive regime, where the Schwinger-Dyson equations indicate the presence of a distinct incoherent NFL regime at $T \ll t^2/J$. That contrasts with the behavior of incoherent metals, which have a finite Fermi surface. In the latter, the system flows towards a Fermi liquid at low temperature [111].

Those results should be compared with the several lattice models of SYK dots that have been studied recently [104, 111, 112]. Ref. [104, 111] studied a lattice of coupled dots in the limit where the SYK coupling J is the highest energy scale. In those cases, the physics of a single dot dominates, with the effects of hopping being perturbative. The $\Sigma \propto \sqrt{\omega}$ scaling of the self energy in this limit ultimately leads to a linear in T dc resistivity.

Among the dispersive SYK models, the one studied in Ref. [112] is the closest to ours. They examined a two-band model for arbitrary dimension and dispersion, with a color site dependent SYK interaction, which forces the saddle point solution of the Green's function to be diagonal but still color site dependent. Their solution for the self-energy is purely imaginary and color site independent, differently from our results. That leads to an approximate conformal symmetry in the problem in the NFL regime, in contrast with our work, where we find that conformal symmetry is absent. In this paper, we focused in the crossover between the regime dominated by the $0 + 1$ dimensional SYK fixed point and the low temperature NFL regime for a 1D semimetal with parabolic band touching, and addressed the transport properties of this novel state.

Chapter 5

Conclusions

In this thesis, we addressed the effect of interactions in coupled quantum wire systems and incoherent semimetals. We began by reviewing the basic framework used to analyze one dimensional quantum wire systems which involves reformulating the interacting fermion problem into a non-interacting bosonic theory, known as bosonization. In the absence of backscattering, the low energy properties of these systems are generically described by the Luttinger liquid theory. This theory takes the same significance as that of Fermi liquid theory in higher dimensions as a generic state of matter. We then reviewed the phenomenological theoretical works that have analyzed the problem of several coupled Luttinger liquids. It has been shown that when inter-wire current-current and density-density interactions are taken into account, the coupled Luttinger liquid system can be described as a generalized smectic non-Fermi liquid fixed point. Considering the possible perturbations to this fixed point, which can arise from electron hopping between the wires, a generic phase diagram was predicted in the literature. We revisited this problem, motivated by the recent developments in the theoretical and experimental understanding of twisted moiré heterostructures. Many moiré systems have been shown to well described by effective models of coupled quantum wires. In these systems, integrating out the degrees on freedom in one layer leads to an effective mass term that follows the same periodic pattern as the underlying moiré pattern. At the interfaces where the mass term changes sign, one dimensional modes appear leading to a coupled wire description of these systems.

We studied an effective microscopic model for a system of coupled parallel wires constructed from a honeycomb lattice coupled to a periodic mass term. We computed the wave-functions for the electron that live on the interface where the mass term changes sign, and showed that these modes

are Luttinger liquids, whose Luttinger parameters are tunable by the strength of the mass term and the distance between the interfaces. Furthermore, taking into account the Coulomb interaction between electrons on different wires, we showed that the system can be described as a smectic metal. Incorporating the perturbations arising from inter-wire hopping, we drew the phase diagram for this system as function of the effective fine structure constant and the ratio ℓ/L where ℓ is the lateral spread of the wave-functions that live on the wires and L is the distance between wires. We showed that contrary to the phenomenological models, superconductivity is generically absent in our phase diagram. In the ideal quantum wire limit, where the transverse width of the wave-functions approach zero, the smectic metal phase is stable. The phase diagram shows an interesting quantum phase transition between a two dimensional Fermi liquid phase and the smectic metal phase. A phase transition towards either a charge density wave or a Fermi liquid phase is expected at very low temperature in models with parametrically weak backscattering. Although our model is based on topological quantum wires, we expect our results to applicable to generic quantum wires, topological or not, with exponentially localized wavefunctions.

In the second part of the thesis, we studied the physics of SYK models in the context of a semi-metallic system. SYK models have attracted huge attention in the recent years due to a variety of reasons. The SYK dot model describes a quantum dot with a large number of fermions, with all to all random interactions. This model is an example of a strongly interacting quantum field theory which is exactly solvable in the limit of a large number of fermions. Furthermore, the model was shown to exhibit approximate conformal symmetry and is dual to gravitational theories in 1+1 dimensions. The model is also known to be maximally chaotic. On the condensed matter side, this model describes matter without quasiparticles. A recent experimental proposal has suggested that the SYK model could be realized in an irregular graphene flake in the presence of a strong magnetic field. Several lattice models constructed out of SYK dots were proposed in recent years, primarily with the aim of constructing incoherent non-Fermi liquid systems. For systems which have a Fermi surface in the non-interacting case, it was shown that SYK interactions lead to the system behaving as an incoherent metal at high temperatures and as a Fermi liquid at low temperatures, with a characteristic crossover temperature scale. Much excitement arose out of the linear in temperature dc resistivity in the incoherent metal phase, which is characteristic of the strange metal phase in high -T_c superconductors. After briefly reviewing these aspects, we addressed the physics of SYK

interaction in semi-metallic models, where the Fermi surface in the non interacting case is reduced to a Fermi point.

We constructed a simple one dimensional semi-metallic model with a quadratic dispersion. Incorporating local SYK interactions, we showed that the model realizes two phases as a function of temperature. In the low temperature limit, we found that the Schwinger-Dyson equations do not admit an exact analytic finite temperature solution. We solved those equations exactly exploiting the scaling symmetry of the model, combined with numerical calculations. We found that the Green's function and self-energy scale with temperature with a power law of $T^{-2/5}$ and $T^{4/5}$ respectively. We then study the transport properties and show that dc resistivity scales with a sublinear power law dependence on temperature, $\rho \sim T^{2/5}$. We computed the Lorentz ratio with the analytically continued scaling functions and find that $L \approx 3.2$, rather close to that of Fermi liquids. The scaling analysis of this problem indicates that if one starts in the high temperature SYK fixed point of the problem, which is given by $t^2/J \ll T \ll J$ where t is the hopping strength and J is the SYK interaction, the hopping parameter will grow, as one scales the temperature down. At the low temperature limit the Schwinger-Dyson equations indicate the presence of a distinct incoherent NFL regime when $T \ll t^2/J$. That contrasts with the behavior of incoherent metals, which have a finite Fermi surface, where the system flows towards a Fermi liquid at low temperature.

Our effective microscopic model of parallel quantum wires may be relevant to the recent experiments on twisted bilayer tWTe$_2$[41], which was effectively shown to be described as an array of parallel Luttinger liquids. Effective models that could describe moiré heterostructures with more complicated moiré patterns could prove useful in explaining the growing body of experimental works in these systems. More analysis into the properties of dispersive SYK models especially in understanding many body chaos remain open. More comprehensive studies on the implications of incoherence on higher dimensional Dirac and topological materials also remain to be explored.

Appendix A

Action for Luttinger liquids

This Appendix gives a brief derivation of the action for Luttinger liquids.

$$\mathcal{H} \equiv \frac{1}{2} \int dy \left[\frac{u}{K} \left(\partial_y \theta \right)^2 + uK \left(\partial_y \phi \right)^2 \right]. \tag{A.1}$$

The term $\Pi(y) = \partial_y \theta$ is canonically conjugate to the field $\phi(y)$. The action for this theory is:

$$-\mathcal{S} = \int_\tau \int_y \left(i\Pi(\tau, y) \partial_\tau \phi(\tau, y) - H\left[\phi(\tau, y), \Pi(\tau, y) \right] \right) \tag{A.2}$$

$$= \int_\tau \int_y \left(i\partial_y \theta(\tau, y) \partial_\tau \phi(\tau, y) - H\left[\phi(\tau, y), \Pi(\tau, y) \right] \right). \tag{A.3}$$

The Hamiltonian in momentum space is

$$\mathcal{H} = \left(\frac{1}{2\pi} \right) \int_k \left[\frac{u}{2K} k^2 \theta(\mathbf{k}) \theta(-\mathbf{k}) + \frac{uK}{2} k^2 \phi(\mathbf{k}) \phi(-\mathbf{k}) \right]. \tag{A.4}$$

In momentum space the action becomes

$$-\mathcal{S} = \left(\frac{1}{2\pi} \right)^2 \int_{k,\omega_n} \left(-ik\omega_n \theta(\mathbf{k}) \phi(-\mathbf{k}) - \left[\frac{u}{2K} k^2 \theta(\mathbf{k}) \theta(-\mathbf{k}) + \frac{uK}{2} k^2 \phi(\mathbf{k}) \phi(-\mathbf{k}) \right] \right)$$

$$= \left(\frac{1}{2\pi} \right)^2 \int_{k,\omega_n} \left(-ik\omega_n \theta(\mathbf{k}) \phi(-\mathbf{k}) - \frac{u}{2K} k^2 \theta(\mathbf{k}) \theta(-\mathbf{k}) - \frac{uK}{2} k^2 \phi(\mathbf{k}) \phi(-\mathbf{k}) \right), \tag{A.5}$$

where $\omega_n, k = \mathbf{k}$. Now we add and subtract $\frac{\omega_n^2}{\frac{u}{K}}\phi(\mathbf{k})\phi(-\mathbf{k}))$, from which one readily finds

$$
-\mathcal{S} = \left(\frac{1}{2\pi}\right)^2 \int_{k,\omega_n}
$$
$$
\left(-\frac{1}{2}\frac{\omega_n^2}{\frac{u}{K}}\phi(\mathbf{k})\phi(-\mathbf{k}) + \left\{\frac{1}{2}\frac{\omega_n^2}{\frac{u}{K}}\phi(\mathbf{k})\phi(-\mathbf{k}) - ik\omega_n\theta(\mathbf{k})\phi(-\mathbf{k}) - \frac{u}{2K}k^2\theta(\mathbf{k})\theta(-\mathbf{k})\right\} - \frac{uK}{2}k^2\phi(\mathbf{k})\phi(-\mathbf{k})\right).
$$

The curly brackets can be rewritten as

$$
\{-\} = -\frac{u}{2K}k^2\left[\theta(\mathbf{k}) + \frac{i\omega_n}{\frac{u}{K}k}\phi(\mathbf{k})\right]\left[\theta(-\mathbf{k}) + \frac{i\omega_n}{\frac{u}{K}k}\phi(-\mathbf{k})\right].
$$

Then if we change variables to $\theta(\mathbf{k}) + \frac{i\omega_n}{\frac{u}{K}k}\phi(\mathbf{k}) = \widetilde{\theta}(\mathbf{k})$,

$$
-\mathcal{S} = \left(\frac{1}{2\pi}\right)^2 \int_{k,\omega_n}\left(-\frac{1}{2}\frac{\omega_n^2}{\frac{u}{K}}\phi(\mathbf{k})\phi(-\mathbf{k}) + \left\{-\frac{u}{2K}k^2\widetilde{\theta}(\mathbf{k})\widetilde{\theta}(-\mathbf{k})\right\} - \frac{uK}{2}k^2\phi(\mathbf{k})\phi(-\mathbf{k})\right).
$$

Integrating out $\widetilde{\theta}(\mathbf{k})$ gives

$$
\mathcal{S} = \left(\frac{1}{2\pi}\right)^2 \int_{k,\omega_n}\left(\frac{1}{2}\frac{\omega_n^2}{\frac{u}{K}}\phi(\mathbf{k})\phi(-\mathbf{k}) + \frac{uK}{2}k^2\phi(\mathbf{k})\phi(-\mathbf{k})\right)
$$
$$
\mathcal{S} = \left(\frac{1}{2\pi}\right)^2 \int_{k,\omega_n}\frac{1}{2}\left(\frac{\omega_n^2}{\frac{u}{K}} + uKk^2\right)\phi(\mathbf{k})\phi(-\mathbf{k}). \tag{A.6}
$$

Instead, if we had integrated out ϕ, we would get

$$
\mathcal{S} = \frac{1}{2}\left(\frac{1}{2\pi}\right)^2 \int_{k,,\omega}\left(\frac{\omega_n^2}{uK} + \frac{u}{k}k^2\right)|\theta(\mathbf{k})|^2 \tag{A.7}
$$

In position-time space,

$$
\mathcal{S} = \frac{K}{2}\int_\tau\int_y\left[\frac{1}{u}\left(\partial_\tau\phi(\tau,y)\right)^2 + u\left(\partial_y\phi\right)^2\right]. \tag{A.8}
$$

Appendix B

Renormalization group analysis

This Appendix gives a derivation of how the RG scaling dimensions are obtained. We start from the smectic metal action given by,

$$\mathcal{S}\left(\theta\right) = \frac{1}{2} \int_{k,k_\perp,\omega} \left(\frac{\omega^2}{W_1(\mathbf{k})} + \frac{k^2}{W_0(\mathbf{k})} \right) \left| \theta(\mathbf{k}) \right|^2. \tag{B.1}$$

Perturbations to this action can be analyzed using a renormalization group analysis. For example, the interaction that leads to superconductivity is

$$\mathcal{S}_{int}\left(\theta\right) = \int_\tau \int_x g_{sc} \sum_a \cos\left[\sqrt{4\pi}\left(\theta_a(\tau,x) - \theta_{a+1}(\tau,x) \right) \right]. \tag{B.2}$$

Renormalization involves decomposing the original fields into short wavelength and long wavelength components and then integrating out the long wavelength components from the action. In this process, one obtains an effective action that has the same structure as the original one, but with a new set of coupling constants. This helps ascertain the relative importance of various coupling constants. See, for example [1]. We split the momentum space $\left| \overrightarrow{k} \right| < \Lambda$ into a large region $\left| \overrightarrow{k} \right| < \Lambda'$ and a tiny sliver $\Lambda' < \left| \overrightarrow{k} \right| < \Lambda$ where $\Lambda' = \Lambda\left(1 - dt\right)$ and $\overrightarrow{k} = (\omega, k)$. We can then rewrite the original field θ as a sum over slow and fast modes $\theta_a(\tau,x) = \theta_a(\tau,x)_f + \theta_a(\tau,x)_s$,

$$\begin{aligned} \theta_a(\tau,x) &= \int_{\left|\overrightarrow{k}\right|<\Lambda'} e^{i\overrightarrow{k}.\overrightarrow{x}} \theta_a(\overrightarrow{k}) + \int_{\Lambda'<\left|\overrightarrow{k}\right|<\Lambda} e^{i\overrightarrow{k}.\overrightarrow{x}} \theta_a(\overrightarrow{k}) \\ &\equiv \theta_a(\tau,x)_f + \theta_a(\tau,x)_s \end{aligned}$$

Under this decomposition, the Gaussian part of the action (B.1) splits into two copies, one for slow modes and one for fast modes. The partition function may be written as

$$
\begin{aligned}
Z &= \int D\theta_f D\theta_s e^{-\mathcal{S}(\theta_f) - \mathcal{S}(\theta_s) - \mathcal{S}_{int}\left(\theta_a(\tau,x)_f + \theta_a(\tau,x)_s\right)} \\
&= Z_f \int D\theta_s e^{-\mathcal{S}(\theta_s)} \left\langle e^{-\mathcal{S}_{int}(\theta_a(\tau,x))} \right\rangle_f
\end{aligned}
\tag{B.3}
$$

where $Z_f = \int D\theta_f e^{-\mathcal{S}(\theta_f)}$ and

$$
\left\langle e^{-\mathcal{S}_{int}(\theta_a(\tau,x))} \right\rangle_f = \int D\theta_f e^{-\mathcal{S}(\theta_f) - \mathcal{S}_{int}\left(\theta_a(\tau,x)_f + \theta_a(\tau,x)_s\right)}.
\tag{B.4}
$$

Reexponentiating (B.4), we can obtain an effective action $\mathcal{S}_{eff}(\theta_s)$ that depends only on the slow modes,

$$
\mathcal{S}_{eff}(\theta_s) = \mathcal{S}(\theta_s) - \ln \left\langle e^{-\mathcal{S}_{int}(\theta_a(\tau,x))} \right\rangle_f.
\tag{B.5}
$$

To compute the above correction, we can expand the above expression in powers of g_{sc} when the perturbation is weak. To the lowest order in perturbative RG, the action gets renormalized as $\mathcal{S}_{eff}(\theta_s) = \mathcal{S}(\theta_s) + \langle \mathcal{S}_{int} \rangle_f$. Therefore we need to compute $\langle \mathcal{S}_{int} \rangle_f$,

$$
\begin{aligned}
\left\langle g_{sc} \cos\left[\sqrt{4\pi}\left(\theta_a(\tau,x) - \theta_{a+1}(\tau,x)\right)\right] \right\rangle_f &= g_{sc} \left\langle \frac{1}{2} \sum_{\sigma=\pm} e^{i\sigma\left[\sqrt{4\pi}(\theta_a(\tau,x) - \theta_{a+1}(\tau,x))\right]} \right\rangle_f \\
&= g_{sc} \sum_{\sigma=\pm} \frac{1}{2} e^{i\sigma\left[\sqrt{4\pi}(\theta_a(\tau,x)_s - \theta_{a+1}(\tau,x)_s)\right]} \\
&\quad \times \left\langle e^{i\sigma\left[\sqrt{4\pi}\left(\theta_a(\tau,x)_f - \theta_{a+1}(\tau,x)_f\right)\right]} \right\rangle_f.
\end{aligned}
$$

Using

$$
\left\langle e^{i\sigma\left[\sqrt{4\pi}\left(\theta_a(\tau,x)_f - \theta_{a+1}(\tau,x)_f\right)\right]} \right\rangle_f = e^{-2\pi\left\langle\left(\theta_a(\tau,x)_f - \theta_{a+1}(\tau,x)_f\right)^2\right\rangle},
$$

we see that

$$
\begin{aligned}
\left\langle g_{sc} \cos\left[\sqrt{4\pi}\left(\theta_a(\tau,x) - \theta_{a+1}(\tau,x)\right)\right] \right\rangle_f &= \left[\cos\sqrt{4\pi}\left(\theta_a(\tau,x)_s - \theta_{a+1}(\tau,x))_s\right)\right] \\
&\quad \times e^{-2\pi\left\langle\left(\theta_a(\tau,x)_f - \theta_{a+1}(\tau,x)_f\right)^2\right\rangle}
\end{aligned}
$$

where

$$\left\langle (\theta_a(\tau,x)_f - \theta_{a+1}(\tau,x)_f)^2 \right\rangle \;\; = \;\; 2 \int_{-\pi/L}^{\pi/L} \frac{dk_\perp}{(2\pi/L)} \left[\int' \frac{dk d\omega}{(2\pi)^2} \left\langle |\theta(k)|^2 \right\rangle \right] (1 - \cos k_\perp L).$$

The momentum integral gives

$$\int' \frac{dk d\omega}{(2\pi)^2} \left\langle |\theta(k)|^2 \right\rangle = \int' \frac{dk d\omega}{(2\pi)^2} \frac{1}{\left(\frac{\omega_n^2}{W_1(k_\perp)} + \frac{k^2}{W_0(k_\perp)} \right)} = \sqrt{W_0(k_\perp) W_1(k_\perp)} \frac{dt}{2\pi} = \kappa(k_\perp) \frac{dt}{2\pi}, \quad \text{(B.6)}$$

where prime indicates mode elimination. Hence,

$$\exp \left[-2\pi \left\langle (\theta_a(\tau,x)_f - \theta_{a+1}(\tau,x)_f)^2 \right\rangle \right] = \exp \left[-2\pi \times 2 \int_{-\pi/L}^{\pi/L} \frac{dk_\perp}{(2\pi/L)} \kappa(k_\perp L) \frac{dt}{2\pi} (1 - \cos k_\perp L) \right]$$

$$= s^{-\triangle_{sc}} \quad \text{(B.7)}$$

where I used $s = e^{dt}$ and $\triangle_{sc} = 2 \int_{-\pi}^{\pi} \frac{dk_\perp}{2\pi} \left[\kappa(k_\perp) \right] (1 - \cos k_\perp)$. Also on renormalization, $\int_\tau \int_x \rightarrow s^2 \int_{\tau'} \int_{x'}$. Therefore the flow equation for g_{sc} is $g_{sc} \rightarrow g_{sc} s^{2-\triangle_{sc}}$. This means that when the scaling dimension of this operator $\triangle_{sc} < 2$, we superconductivity becomes relevant.

Similarly for the CDW instability, we have

$$\mathcal{S}_{int} = \int_\tau \int_x g_{cdw} \sum_a \cos \left[\sqrt{4\pi} \left(\phi_a(\tau,x) - \phi_{a+1}(\tau,x) \right) \right]. \quad \text{(B.8)}$$

In this case we need to compute $\left\langle \cos \left[\sqrt{4\pi} \left(\phi_a(\tau,x)_f - \phi_{a+1}(\tau,x)_f \right) \right] \right\rangle$. To this end, we use the action (2.43). Following the same steps as above we get,

$$\triangle_{sc} = 2 \int_{-\pi}^{\pi} \frac{dk_\perp}{2\pi} \left[\kappa(k_\perp)^{-1} \right] (1 - \cos k_\perp).$$

Finally, for the case of single particle hopping, the bosonized interaction term is

$$\mathcal{H}_{sp} = g_{sp} \sum_a \cos \left[\sqrt{\pi} \left(\theta_a - \theta_{a+1} \right) \right] \cos \left[\sqrt{\pi} \left(\phi_a - \phi_{a+1} \right) \right]. \quad \text{(B.9)}$$

Now we can average the θ and ϕ terms separately,

$$
\left\langle \cos\left[\sqrt{\pi}\left(\theta_a - \theta_{a+1}\right)\right]\right\rangle \left\langle \cos\left[\sqrt{\pi}\left(\phi_a - \phi_{a+1}\right)\right]\right\rangle = \exp\left[-\frac{\pi}{2}\left\langle\left(\theta_a(\tau,x)_f - \theta_{a+1}(\tau,x)_f\right)^2\right\rangle\right] \times
$$

$$
\exp\left[-\frac{\pi}{2}\left\langle\left(\phi_a(\tau,x)_f - \phi_{a+1}(\tau,x)_f\right)^2\right\rangle\right]. \quad \text{(B.10)}
$$

The average of the first term on the RHS is the same as for the case of sc obtained previously and the second term corresponds to the cdw case respectively, except for a factor of $\frac{1}{4}$. Therefore the scaling dimension of the single particle hopping operator, $\triangle_{sp}$ is

$$
\triangle_{sp} = \frac{\triangle_{sc}}{4} + \frac{\triangle_{cdw}}{4}. \quad \text{(B.11)}
$$

The calculations for the spinful case is similar. For example, the sc perturbation after Bosonization is,

$$
\mathcal{H}_{sc} = \sum_j g_{sc}^{spin} \int dx \cos\left[\sqrt{2\pi}\left(\Theta_{\rho,j} - \Theta_{\rho,j+1}\right)\right] \cos\left[\sqrt{2\pi}\left(\Phi_{\sigma,j}\right)\right] \cos\left[\sqrt{2\pi}\left(\Phi_{\sigma,j+1}\right)\right]. \quad \text{(B.12)}
$$

The Φ_σ variables now contribute to the dimensions of these terms. Because the analogue of $\kappa\left(k_\perp\right)$ in Eq. (14) is 1, in the main text, the contribution of these variables is trivial, and the dimensions of $\triangle_{sc}^{spin}$ is given by, $\triangle_{sc}^{spin} = 1 + \int_{-\pi}^{\pi}\frac{dk_\perp}{2\pi}\left[\kappa\left(k_\perp\right)\right]\left(1 - \cos k_\perp\right).$

Appendix C

Disorder averaging

The action for the problem defined in Chapter 4, Eq. (3.1) is

$$
\mathcal{S} = \int \mathrm{d}\tau \left(\sum_i \Psi_i^\dagger (\tau) (\partial_\tau - \mu) \Psi_i (\tau) \right) + \int \mathrm{d}\tau \frac{1}{(2N)^{\frac{3}{2}}} \sum_{ijkl} J_{ijkl} \Psi_i^\dagger (\tau) \Psi_j^\dagger (\tau) \Psi_k (\tau) \Psi_l (\tau), \quad \text{(C.1)}
$$

where $\overline{|J_{ijkl}|^2} = J^2$. To deal with the random interaction, we need to average over their distribution. For that, first we need to introduce M replicas of the fields. This can be achieved by just endowing the fields with an extra index α which runs from 1 to M.

$$
\mathcal{S}_M = \sum_{\alpha=1}^{M} \int \mathrm{d}\tau \left(\sum_i \Psi_i^{\alpha\dagger} (\tau) (\partial_\tau - \mu) \Psi_i^\alpha (\tau) \right)
$$
$$
+ \sum_{\alpha=1}^{M} \int \mathrm{d}\tau \frac{1}{(2N)^{\frac{3}{2}}} \sum_{ijkl} J_{ijkl} \Psi_i^{\alpha\dagger} (\tau) \Psi_j^{\alpha\dagger} (\tau) \Psi_k^\alpha (\tau) \Psi_l^\alpha (\tau). \quad \text{(C.2)}
$$

The partition function is $Z_M = \int D\Psi D\Psi^\dagger e^{-\mathcal{S}_M}$. Eventually, we will be interested in the disorder averaged Free energy defined as $-\beta \overline{F} = \overline{\ln Z} = \lim_{M \to 0} \frac{\ln \overline{Z_M}}{M}$.

On disorder averaging using $\langle\langle e^{-\sum_{ijk\ell} J_{ijk\ell} A_{ijk\ell}} \rangle\rangle = e^{2J^2 \sum_{ijk\ell} \bar{A}_{ijk\ell} A_{ijk\ell}}$, we get,

$$
\begin{aligned}
\overline{Z_M} = \int D\Psi D\Psi^\dagger \exp\{ &-\sum_{\alpha=1}^{M} \int d\tau \left(\sum_i \Psi_i^{\alpha\dagger}(\tau)(\partial_\tau - \mu)\Psi_i^\alpha(\tau) \right) \\
&+ \sum_{ijkl} \frac{J^2}{4N^3} \sum_{\alpha=1}^{M}\sum_{\beta=1}^{M} \int d\tau \int d\tau' \, \Psi_i^{\alpha\dagger}(\tau)\Psi_j^{\alpha\dagger}(\tau)\Psi_k^\alpha(\tau)\Psi_l^\alpha(\tau)\Psi_l^{\beta\dagger}(\tau')\Psi_k^{\beta\dagger}(\tau')\Psi_i^\beta(\tau')\Psi_j^\beta(\tau') \}.
\end{aligned}
$$

$$(C.3)$$

We define the 'Green's function' as $NG^{\alpha\beta}(\tau - \tau') = \sum_i \Psi_i^{\dagger\alpha}(\tau')\Psi_i^\beta(\tau)$. Using Lagrange multipliers expressed as an integral over Ξ, G we get,

$$
I = \int \mathcal{D}\Xi \mathcal{D}G \exp \left[\sum_{\alpha=1}^{M}\sum_{\beta=1}^{M} \int_0^\beta d\tau \int_0^\beta d\tau' \Xi^{\alpha\beta}(\tau' - \tau) \left(NG^{\alpha\beta}(\tau - \tau') - \sum_i \Psi_i^{\dagger\alpha}(\tau')\Psi_i^\beta(\tau) \right) \right].
$$

$$(C.4)$$

Then,

$$
\begin{aligned}
\overline{Z_M} = \int \mathcal{D}\Xi \mathcal{D}G D\Psi D\Psi^\dagger \exp\{ &-\sum_{\alpha=1}^{M} \int d\tau \left(\sum_i \Psi_i^{\alpha\dagger}(\tau)(\partial_\tau - \mu)\Psi_i^\alpha(\tau) \right) \\
&+ \sum_{\sigma\sigma'} \frac{J^2 N}{4} \sum_{\alpha=1}^{M}\sum_{\beta=1}^{M} \int d\tau \int d\tau' G^{\alpha\beta}(\tau - \tau')^2 G^{\alpha\beta}(\tau' - \tau)^2 \\
&- \sum_{\alpha=1}^{M}\sum_{\beta=1}^{M}\sum_i \int_0^\beta d\tau \int_0^\beta d\tau' \Xi^{\alpha\beta}(\tau - \tau')\Psi_i^{\dagger\alpha}(\tau)\Psi_i^\beta(\tau') \\
&+ N \sum_{\alpha=1}^{M}\sum_{\beta=1}^{M} \int_0^\beta d\tau \int_0^\beta d\tau' \Xi^{\alpha\beta}(\tau' - \tau) G^{\alpha\beta}(\tau - \tau') \}.
\end{aligned}
$$

$$(C.5)$$

Assuming replica diagonal solutions, we may symbolically write,

$$
\overline{Z_M} = \left(\int \mathcal{D}\Xi \mathcal{D}G D\Psi D\Psi^\dagger e^{-S'} \right)^M
$$

and

$$\mathcal{S}' = N \int d\tau \left(\sum_{\sigma} \Psi^{\dagger} (\tau) (\partial_{\tau} - \mu) \Psi (\tau) \right) - \frac{J^2 N}{4} \int d\tau \int d\tau' G (\tau - \tau')^2 G (\tau' - \tau)^2$$

$$+ N \int_0^{\beta} d\tau \int_0^{\beta} d\tau' \Xi (\tau' - \tau) \Psi^{\dagger} (\tau') \Psi (\tau)$$

$$- N \int_0^{\beta} d\tau \int_0^{\beta} d\tau' \Xi (\tau' - \tau) G (\tau - \tau') , \tag{C.6}$$

where $-\beta \overline{F} = \overline{\ln Z} = \lim_{M \to 0} \frac{\log \overline{Z_M}}{M}$. The limit then becomes trivial leading to

$$-\beta \overline{F} = \log \left(\int \mathcal{D}\Xi \mathcal{D}G D\Psi D\Psi^{\dagger} e^{-\mathcal{S}'} \right) .$$

Defining $e^{-\beta \overline{F}} \equiv Z'_{\text{eff}} \equiv \int \mathcal{D}\Xi \mathcal{D}G D\Psi D\Psi^{\dagger} e^{-N\mathcal{S}'_{\text{eff}}}$,

$$\mathcal{S}'_{\text{eff}} = \int d\tau \int d\tau' \left(\Psi^{\dagger} (\tau) (\delta_{\tau\tau'} (\partial_{\tau} - \mu) + \Xi (\tau - \tau')) \Psi (\tau') \right)$$

$$- \int dx \frac{J^2}{4} \int d\tau \int d\tau' G (\tau - \tau')^2 G (\tau' - \tau)^2$$

$$- \int_0^{\beta} d\tau \int_0^{\beta} d\tau' \Xi (\tau' - \tau) G (\tau - \tau') . \tag{C.7}$$

After performing the Gaussian integral over Ψ, variation with respect to $G (\tau' - \tau)$ gives

$$\Xi (\tau - \tau') = -J^2 G^2 (\tau - \tau') G (\tau' - \tau) . \tag{C.8}$$

Variation with respect to $\Xi (i\omega_n)$ yields

$$G (i\omega_n) = \frac{1}{i\omega_n + \mu - \Xi (i\omega_n)} . \tag{C.9}$$

Eqs. (C.8),(C.9) are Eqs. (3.3),(3.4) in the main text.

Bibliography

[1] R. Shankar, Quantum Field Theory and Condensed Matter: An Introduction (Cambridge University Press, Cambridge, 2017).

[2] Mahan, G. D.. Many Particle Physics, Third Edition. New York: Plenum, 2000.

[3] Altland A and Simons B, 2010 Condensed Matter Field Theory (Cambridge: Cambridge University Press).

[4] J. W. Negele and J. Orland, Quantum Many Particle Systems (Addison-Wesley, New York, 1981).

[5] Fetter, A. L., and J. D. Walecka, Quantum Theory of Many-Particle Systems (McGraw-Hill, San Francisco), 1971.

[6] Tarucha, S., Honda, T. & Saku, T., Reduction of quantized conductance at low temperatures observed in 2 to 10mm-long quantum wires, Solid State Commun. **94**, 413-418 (1995).

[7] Auslaender, O. M., A. Yacoby, R. de Picciotto, K. W. Baldwin, L. N. Pfeiffer, and K. W. West, Tunneling Spectroscopy of the Elementary Excitations in a One-Dimensional Wire, Science **295**, 825 (2002).

[8] Tserkovnyak, Y., B. I. Halperin, O. M. Auslaender, and A. Yacoby, Finite-Size Effects in Tunneling between Parallel Quantum Wires, Phys. Rev. Lett. **89**, 136805 (2002).

[9] Dresselhaus, Mildred S., Gene Dresselhaus, and Peter C. Eklund, Science of fullerenes and carbon nanotubes: their properties and applications. Elsevier, (1996).

[10] Bockrath, M., Cobden, D. H., Lu, J., Rinzler, A. G., Smalley, R. E., Balents, L., & McEuen, P. L., Luttinger-liquid behaviour in carbon nanotubes, Nature, **397**, 6720 (1999).

[11] Yao, Zhen, Henk W. Ch Postma, Leon Balents, and Cees Dekker, Carbon nanotube intramolecular junctions, Nature **402**, 6759 (1999)

[12] M.P.A. Fisher and L.I. Glazman, in Mesoscopic Electron Transport, eds. L.L. Sohn, L.P. Kouwenhoven, and G. Schön (Kluwer, Netherlands, 1997), p. 331.

[13] Glattli, C. In High Magnetic Fields: Applications in Condensed Matter Physics and Spectroscopy; Berthier, C., et al., Ed.; Springer-Verlag: Berlin (2002).

[14] Milliken, F. P., C. P. Umbach, and R. A. Webb, Indications of a Luttinger liquid in the fractional quantum Hall regime, Solid State Communications **97**, no. 4 (1996).

[15] T. Giamarchi, Quantum Physics in One Dimension (Oxford University Press, 2003).

[16] E. Fradkin, Field Theories of Condensed Matter Physics, 2nd ed. (Cambridge University Press, 2013).

[17] P. Chaikin and T. Lubensky, Principles of Condensed Matter Physics (Cambridge University Press, Cambridge, 1995).

[18] F. D. M. Haldane, "Luttinger Liquid Theory" of OneDimensional Quantum Fluids. I. Properties of the Luttinger Model and Their Extension to the General 1D Interacting Spinless Fermi Gas, J. Phys. C **14**, 2585 (1981).

[19] F. D. M. Haldane, Effective Harmonic-Fluid Approach to Low-Energy Properties of One-Dimensional Quantum Fluids, Phys. Rev. Lett. **47**, 1840 (1981)

[20] J. C. Y. Teo and C. L. Kane, From Luttinger Liquid to Non-Abelian Quantum Hall States, Phys. Rev. B **89**, 085101 (2014).

[21] J. Klinovaja and Y. Tserkovnyak, Quantum Spin Hall Effect in Strip of Stripes Model, Phys. Rev. B **90**, 115426 (2014).

[22] E. Sagi and Y. Oreg, Non-Abelian Topological Insulators from an Array of Quantum Wires, Phys. Rev. B **90**, 201102 (2014).

[23] E. Sagi and Y. Oreg, From an Array of Quantum Wires to Three-Dimensional Fractional Topological Insulators, Phys. Rev. B **92**, 195137 (2015).

[24] J. Klinovaja, P. Stano, and D. Loss, Topological Floquet Phases in Driven Coupled Rashba Nanowires, Phys. Rev. Lett. **116**, 176401 (2016).

[25] S. Strong, D. G. Clarke, and P. W. Anderson, Magnetic Field Induced Confinement in Strongly Correlated Anisotropic Materials, Phys. Rev. Lett. **73**, 1007 (1994).

[26] V.M. Yakovenko, Once again about interchain hopping, JETP Lett. **56**, 510 (1992).

[27] S. A. Kivelson et al, Electronic liquid-crystal phases of a doped Mott insulator, Nature **393**, 550 (1998).

[28] E. Fradkin and S. Kivelson, Liquid-crystal phases of quantum Hall systems, Phys. Rev. B **59**, 8065 (1999).

[29] P. W. Anderson, "Confinement" in the one-dimensional Hubbard model: Irrelevance of single-particle hopping, Phys. Rev. Lett. **67**, 3844 (1991).

[30] J. M. Tranquada, D. J. Buttrey, V. Sachan, and J. E. Lorenzo, Simultaneous Ordering of Holes and Spins in $La_2NiO_{4.125}$, Phys. Rev. Lett. **73**, 1003 (1994).

[31] J. Zaanen and O. Gunnarsson, Charged magnetic domain lines and the magnetism of high- T_c oxides, Phys. Rev. B **40**, 7391 (1989).

[32] K. Machida, Magnetism in La_2CuO_4 based compounds, Phys. C Supercond. **158**, 192 (1989).

[33] M. Kato, K. Machida, H. Nakanishi, and M. Fujita, Soliton Lattice Modulation of Incommensurate Spin Density Wave in Two Dimensional Hubbard Model -A Mean Field Study- , J. Phys. Soc. Japan **59**, 1047 (1990).

[34] V. J. Emery, S. A. Kivelson, and J. M. Tranquada, Stripe phases in high-temperature superconductors, Proc. Natl. Acad. Sci. USA **96**, 8814 (1999).

[35] R. Mukhopadhyay, C. L. Kane, and T. C. Lubensky, Crossed sliding Luttinger liquid phase, Phys. Rev. B **63**, 081103(R) (2001).

[36] See V. Emery, in Highly Conducting One-Dimensional Solids, edited by J. Devreese et al. (Plenum, New York, 1979).

[37] C. Bourbonnais and L. G. Caron, Renormalization Group Approach To Quasi-One-Dimensional Conductors, Int. J. Mod. Phys. B **5**, 1033 (1991).

[38] V. J. Emery, E. Fradkin, S. A. Kivelson, and T. C. Lubensky, Quantum Theory of the Smectic Metal State in Stripe Phases, Phys. Rev. Lett. **85**, 2160 (2000).

[39] A. Vishwanath and D. Carpentier, Two-Dimensional Anisotropic Non-Fermi-Liquid Phase of Coupled Luttinger Liquids, Phys. Rev. Lett. **86**, 676 (2001).

[40] R. Mukhopadhyay, C. L. Kane, and T. C. Lubensky, Sliding Luttinger liquid phases, Phys. Rev. B **64**, 045120 (2001).

[41] Wang, P., Yu, G., Kwan, Y.H. et al. One-dimensional Luttinger liquids in a two-dimensional moiré lattice. Nature **605**, 57–62 (2022).

[42] Georges, A., Giamarchi, T. & Sandler, N. Interchain conductivity of coupled Luttinger liquids and organic conductors. Phys. Rev. B **61**, 16393–16396 (2000).

[43] Ning Lu, Chenxi Zhang, Chia-Hui Lee, Juan Pablo Oviedo, Minh An T. Nguyen, Xin Peng, Robert M. Wallace, Thomas E. Mallouk, Joshua A. Robinson, Jinguo Wang, Kyeongjae Cho, and Moon J. Kim, Atomic and Electronic Structures of WTe2 Probed by High Resolution Electron Microscopy and ab Initio Calculations, The Journal of Physical Chemistry C **120** (15), 8364-8369 (2016).

[44] Suárez Morell, E., Correa, J. D., Vargas, P., Pacheco, M. & Barticevic, Z. Flat bands in slightly twisted bilayer graphene: Tight-binding calculations. Phys. Rev. B **82**, 121407(R) (2010).

[45] Bistritzer, R. & MacDonald, A. H. Moiré bands in twisted double-layer graphene. Proc. Natl Acad. Sci. **108**, 12233–12237 (2011).

[46] Physics Today **73**, 1, 18 (2020).

[47] Cao, Y. et al. Correlated insulator behavior at half-filling in magic-angle graphene superlattices. Nature **556**, 80–84 (2018).

[48] Cao, Y. et al., Unconventional superconductivity in magic-angle graphene superlattices, Nature **556**, 43–50 (2018).

[49] Yankowitz, M. et al., Tuning superconductivity in twisted bilayer graphene, Science **363**, 1059–1064 (2019).

[50] Huang, S. et al., Topologically protected helical states in minimally twisted bilayer graphene, Phys. Rev. Lett. **121**, 037702 (2018).

[51] Yoo, H. et al., Atomic and electronic reconstruction at the van der Waals interface in twisted bilayer graphene, Nat. Mater. **18**, 448–453 (2019).

[52] Sunku, S. S. et al. Photonic crystals for nano-light in moiré graphene superlattices. Science **362**, 1153–1156 (2018).

[53] Oostinga, J. B., Heersche, H. B., Liu, X., Morpurgo, A. F. & Vandersypen, L. M. K. Gate-induced insulating state in bilayer graphene devices. Nat. Mater. **7**, 151–157 (2008).

[54] Zhang, Y. et al., Direct observation of a widely tunable bandgap in bilayer graphene, Nature **459**, 820–823 (2009).

[55] S. G. Xu *et al.,* Giant oscillations in a triangular network of one-dimensional states in marginally twisted graphene, Nat. Comm. **10**, 4008 (2019).

[56] C. Chen, A. H. Castro Neto, and V. M. Pereira, Correlated states of a triangular net of coupled quantum wires: Implications for the phase diagram of marginally twisted bilayer graphene, Phys. Rev. B **101**, 165431 (2020).

[57] G Jose and B Uchoa, Stability of the smectic phase in arrays of parallel quantum wires, arXiv:2202.11744 (2022).

[58] M. Killi, Tzu-Chieh Wei, I. Affleck, and A. Paramekanti, Tunable Luttinger Liquid Physics in Biased Bilayer Graphene, Phys. Rev. Lett. **104**, 216406 (2010).

[59] I. Martin, Y. M. Blanter, and A. F. Morpurgo, Topological Confinement in Bilayer Graphene, Phys. Rev. Lett. **100**, 036804 (2008).

[60] S. Biswas, T. Mishra, S. Rao, and A. Kundu, Chiral Luttinger liquids in graphene tuned by irradiation, Phys. Rev. B **102**, 155428 (2020).

[61] A. J. Heeger *et al.*, Solitons in conducting polymers, Rev. Mod. Phys. **60**, 781 (1988).

[62] G. W. Semenoff, V. Semenoff, and F. Zhou, Domain Walls in Gapped Graphene, Phys. Rev. Lett. **101**, 087204 (2008).

[63] M. Kindermann, B. Uchoa, and D. L. Miller, Zero-energy modes and gate-tunable gap in graphene on hexagonal boron nitride, Phys. Rev. B **86**, 115415 (2012).

[64] M. Kindermann and P. N. First, Local sublattice-symmetry breaking in rotationally faulted multilayer graphene, Phys. Rev. B **83**, 045425 (2011).

[65] E. J. Mele, Commensuration and interlayer coherence in twisted bilayer graphene, Phys. Rev. B **81**, 161405(R) (2010).

[66] E. J. Mele Phys. Rev. B **84**, Band symmetries and singularities in twisted multilayer graphene, 235439 (2011).

[67] R. Jackiw and C. Rebbi, Solitons with fermion number $1/2$, Phys. Rev. D **13**, 3398 (1976).

[68] S. Tchoumakov, V. Jouffrey, A. Inhofer, E. Bocquillon, B. Plaçais, D. Carpentier, M. O. Goerbig, Volkov-Pankratov states in topological heterojunctions, Phys. Rev. B **96**, 201302 (2017).

[69] X. Qian, J. Liu, L. Fu, J. Li, Quantum spin Hall effect in two-dimensional transition metal dichalcogenides. Science **346**, 1344–1347 (2014).

[70] Z. Fei, T. Palomaki, S. Wu, W. Zhao, X. Cai, B. Sun, P. Nguyen, J. Finney, X. Xu, D. H. Cobden, Edge conduction in monolayer WTe_2, Nat. Phys. **13**, 677–682 (2017).

[71] S. Tang, C. Zhang, D. Wong, Z. Pedramrazi, H.-Z. Tsai, C. Jia, B. Moritz, M. Claassen, H. Ryu, S. Kahn, J. Jiang, H. Yan, M. Hashimoto, D. Lu, R. G. Moore, C.-C. Hwang, C. Hwang, Z. Hussain, Y. Chen, M. M. Ugeda, Z. Liu, X. Xie, T. P. Devereaux, M. F. Crommie, S.-K. Mo, Z.-X. Shen, Quantum spin Hall state in monolayer 1T´-WTe_2, Nat. Phys. **13**, 683–687 (2017).

[72] L. Peng, Y. Yuan, G. Li, X. Yang, J.-J. Xian, C.-J. Yi, Y.-G. Shi, Y.-S. Fu, Observation of topological states residing at step edges of WTe_2, Nat. Commun. **8**, 659 (2017).

[73] Z.-Y. Jia, Y.-H. Song, X.-B. Li, K. Ran, P. Lu, H.-J. Zheng, X.-Y. Zhu, Z.-Q. Shi, J. Sun, J. Wen, D. Xing, S.-C. Li, Direct visualization of a two-dimensional topological insulator in the single-layer 1T WTe$_2$, Phys. Rev. B **96**, 041108 (2017).

[74] S. Wu, V. Fatemi, Q. D. Gibson, K. Watanabe, T. Taniguchi, R. J. Cava, P. Jarillo-Herrero, Observation of the quantum spin Hall effect up to 100 kelvin in a monolayer crystal, Science **359**, 76–79 (2018).

[75] A. H. Castro Neto, F. Guinea, N. M. R. Peres, K. S. Novoselov, and A. K. Geim, The electronic properties of graphene, Rev. Mod. Phys. **81**, 109 (2009).

[76] V. J. Emery, S. A. Kivelson, and O. Zachar, Spin-gap proximity effect mechanism of high-temperature superconductivity, Phys. Rev. B **56**, 6120 (1997).

[77] T. Y. Yang, *et. al.,* Directional massless Dirac fermions in a layered van der Waals material with one-dimensional long-range order, Nat. Materials **19**, 27 (2020).

[78] A. Luther and I. Peschel, Fluctuation Conductivity and Lattice Stability in One Dimension, Phys. Rev. Lett. **32**, 922 (1974).

[79] B. Uchoa, V. N. Kotov, and M. Kindermann, Valley order and loop currents in graphene on hexagonal boron nitride, Phys. Rev. B **91**, 121412(R) (2015).

[80] M. S. Nevius, M. Conrad, F. Wang, A. Celis, M. N. Nair, A. Taleb-Ibrahimi, A. Tejeda, and E. H. Conrad, Semiconducting Graphene from Highly Ordered Substrate Interactions. Phys. Rev. Lett. **115**, 136802 (2015).

[81] M. Yankowitz, J. Xue, D. Cormode, J. D. Sanchez-Yamagishi, K. Watanabe, T. Taniguchi, P. Jarillo-Herrero, P. Jacquod, and B. J. LeRoy, Emergence of superlattice Dirac points in graphene on hexagonal boron nitride, Nat. Phys. **8**, 382 (2012).

[82] W. Yang, G. Chen, Z. Shi, C.-C. Liu, L. Zhang, G. Xie, M. Cheng, D. Wang, R. Yang, D. Shi, K. Watanabe, T. Taniguchi, Y. Yao, Y. Zhang, and G. Zhang, Epitaxial growth of single-domain graphene on hexagonal boron nitride, Nat. Mater. **12**, 792 (2013).

[83] B. Sachs, T. O. Wehling, M. I. Katsnelson, and A. I. Lichtenstein, Adhesion and electronic structure of graphene on hexagonal boron nitride substrates, Phys. Rev. B **84**, 195414 (2011).

[84] V. M. Pereira, A. H. Castro Neto, and N. M. R. Peres, Tight-binding approach to uniaxial strain in graphene, Phys. Rev. B. **80**, 045401 (2009).

[85] S. Sachdev, Bekenstein-Hawking Entropy and Strange Metals, Phys. Rev. X **5**, 041025 (2015).

[86] S. Sachdev and J. Ye, Gapless Spin-fluid ground state in a random quantum Heisenberg magnet, Phys. Rev. Lett. **70**, 3339 (1993).

[87] S. H. Shenker and D. Stanford, Black holes and the butterfly effect, JHEP **03** (2014).

[88] S. H. Shenker and D. Stanford, Stringy effects in scrambling, JHEP **05** 132 (2015).

[89] J. Maldacena, S. H. Shenker, and D. Stanford, A bound on chaos, JHEP **08** 106 (2016).

[90] J. Maldacena, D. Stanford, and Z. Yang, Diving into Traversable Wormholes, Fortschr. Phys. **65**, 1700034 (2017).

[91] S. Sachdev, The SYK model: a window into non-Fermi liquids, Distinguished Lectures on Topological Materials, Institute for Materials Science, Los Alamos National Laboratory, May 28, 2021 (http://qpt.physics.harvard.edu/talks/talks.html).

[92] A. Larkin and Y.N. Ovchinnikov, Quasiclassical method in the theory of superconductivity, Sov. Phys. JETP **28** (1969) 120.

[93] A. Kitaev, Hidden correlations in the Hawking radiation and thermal noise, talk given at Fundamental Physics Prize Symposium, November 10, 2014.

[94] Zhou, X., Lee, WS., Imada, M. et al. High-temperature superconductivity. Nat Rev Phys **3**, 462–465 (2021).

[95] Proust, C. & Taillefer, L. The remarkable underlying ground states of cuprate superconductors. Annu. Rev. Condens. Matter Phys. 10, 409–429 (2019).

[96] C. L. Kane, Ranjan Mukhopadhyay, and T. C. Lubensky, Fractional Quantum Hall Effect in an Array of Quantum Wires, Phys. Rev. Lett. **88**, 036401(2002).

[97] Charles L. Kane, Ady Stern, and Bertrand I. Halperin, Pairing in Luttinger Liquids and Quantum Hall States, Phys. Rev. X **7**, 031009 (2017)

[98] M. Mitrano, A. A. Husain, S. Viga, A. Kogar, M. S. Rak, S. I. Rubeck, J. Schmalian, B. Uchoa, J. Schneeloche, R. Zhonge, G. D. Gue, and P. Abbamonte, Anomalous density fluctuations in a strange metal, Proc. Nat. Acad. Sci. **115**, 5392 (2018).

[99] A. A. Husain, M. Mitrano, M. S. Rak, S. Rubeck, B. Uchoa, K. March, C. Dwyer, J. Schneeloch, R. Zhong, G. D. Gu, and P. Abbamonte, *Crossover of Charge Fluctuations across the Strange Metal Phase Diagram*, Phys. Rev X **9**, 041062 (2019).

[100] J. Zaanen, Planckian dissipation, Minimal viscosity and the transport in cuprate strange metals, SciPost Phys. **6**, 061 (2019).

[101] A. A. Patel and S. Sachdev, Critical strange metal from fluctuating gauge fields in a solvable random model, Phys. Rev. B **98**, 125134 (2018).

[102] P. Cha, N. Wentzell, O. Parcollet, A. Georges, and E.-A. Kim, Linear resistivity and Sachdev-Ye-Kitaev (SYK) spin liquid behavior in a quantum critical metal with spin-1/2 fermions, Proc. Natl. Acad. Sci. USA **117**, 18341 (2020).

[103] G.E. Volovik, Flat band and Planckian metal, JETP Lett. **110**, 352-353 (2019).

[104] A. A. Patel, J. McGreevy, D. P. Arovas, and S. Sachdev, Magnetotransport in a model of a disordered strange metal, Phys. Rev. X **8**, 021049 (2018).

[105] P. Zhang, Dispersive Sachdev-Ye-Kitaev model: band structure and quantum chaos, Phys. Rev. B **96**, 205138 (2017).

[106] X.-Y. Song, C.-M. Jian, and L. Balents, Strongly Correlated Metal Built from Sachdev-Ye-Kitaev Models, Phys. Rev. Lett. **119**, 216601 (2017).

[107] Rosenhaus, Vladimir, An introduction to the SYK model, Journal of Physics A: Mathematical and Theoretical 52, no. 32 (2019): 323001.

[108] H. Takagi, B. Batlogg, H. L. Kao, J. Kwo, R. J. Cava, J. J. Krajewski, and W. F. Peck, Systematic Evolution of Temperature-Dependent Resistivity in La2−xSrxCuO4, Phys. Rev. Lett. **69**, 2975 (1992).

[109] B. Keimer, S. A. Kivelson, M. R. Norman, S. Uchida, and J. Zaanen, From Quantum Matter to High-Temperature Superconductivity in Copper Oxides, Nature (London) **518**, 179 (2015).

[110] G. R. Stewart, Non-Fermi-Liquid Behavior in d- and f-Electron Metals, Rev. Mod. Phys. **73**, 797 (2001).

[111] D. Chowdhury, Y. Werman, E. Berg, and T. Senthil, Translationally Invariant Non-Fermi Liquid Metals with Critical Fermi-Surfaces: Solvable Models, Phys. Rev. X **8**, 031024 (2018).

[112] A. Haldar, S. Banerjee, V. B. Shenoy, Higher-dimensional Sachdev-Ye-Kitaev non-Fermi liquids at Lifshitz transitions, Phys. Rev. B **97**, 241106 (2018).

[113] D. Ben-Zion and J. McGreevy, Strange metal from local quantum chaos, Phys. Rev. B **97**, 155117 (2018).

[114] A.A. Patel and S. Sachdev, Theory of a Planckian metal, Phys. Rev. Lett. **123**, 066601 (2019).

[115] P. T. Dumitrescu, N. Wentzell, A. Georges, and O. Parcollet, Planckian metal at a doping-induced quantum critical point, Physical Review B, **105** (18), L180404 (2021).

[116] A. Georges, G. Kotliar, W. Krauth, and M. J. Rozenberg, Dynamical mean-field theory of strongly correlated fermion systems and the limit of infinite dimensions, Rev. Mod. Phys. **68**, 13 (1996).

[117] H. J. Vidberg, J. W. Serene, Solving the Eliashberg equations by means of N-point Pade approximants, J. Low Temp. Phys. **29**, 179–192 (1977).

[118] O. Parcollet, M. Ferrero, T. Ayral, H. Hafermann, I. Krivenko, L. Messio, and P. Seth, TRIQS: A Toolbox for Research on Interacting Quantum Systems, Comp. Phys. Comm. **196**, 398-415 (2015).

[119] G. Jose, K. Seo, and B. Uchoa, Non-Fermi liquid behavior in the Sachdev-Ye-Kitaev model for a one-dimensional incoherent semimetal, Phys. Rev. Research **4**, 013145(2022).

[120] Gu, Y., Kitaev, A., Sachdev, S. et al. Notes on the complex Sachdev-Ye-Kitaev model. J. High Energ. Phys. **2020**, 157 (2020).

[121] Juan Maldacena and Douglas Stanford, Remarks on the Sachdev-Ye-Kitaev model, Phys. Rev. D **94**, 106002 (2016).

[122] Anffany Chen, R. Ilan, F. de Juan, D. I. Pikulin, and M. Franz, Quantum Holography in a Graphene Flake with an Irregular Boundary, Phys. Rev. Lett. **121**, 036403 (2018).

[123] Y. Aharonov and A. Casher, Ground state of a spin-$\frac{1}{2}$ charged particle in a two-dimensional magnetic field, Phys. Rev. A **19**, 2461 (1979).